



저작자표시-비영리-변경금지 2.0 대한민국

이용자는 아래의 조건을 따르는 경우에 한하여 자유롭게

- 이 저작물을 복제, 배포, 전송, 전시, 공연 및 방송할 수 있습니다.

다음과 같은 조건을 따라야 합니다:



저작자표시. 귀하는 원저작자를 표시하여야 합니다.



비영리. 귀하는 이 저작물을 영리 목적으로 이용할 수 없습니다.



변경금지. 귀하는 이 저작물을 개작, 변형 또는 가공할 수 없습니다.

- 귀하는, 이 저작물의 재이용이나 배포의 경우, 이 저작물에 적용된 이용허락조건을 명확하게 나타내어야 합니다.
- 저작권자로부터 별도의 허가를 받으면 이러한 조건들은 적용되지 않습니다.

저작권법에 따른 이용자의 권리는 위의 내용에 의하여 영향을 받지 않습니다.

이것은 [이용허락규약\(Legal Code\)](#)을 이해하기 쉽게 요약한 것입니다.

[Disclaimer](#)

공학박사 학위논문

Top-down metamaterial design
for enhancing extraordinary field
focusing of electromagnetic and
acoustic waves

전자기파와 음파의 특이 집속 현상과 이의
극대화를 위한 하향식 메타 물질 설계 및 응용

2015 년 8 월

서울대학교 대학원

공과대학 전기 컴퓨터 공학부

구 석 모

Top-down metamaterial design for enhancing extraordinary field focusing of electromagnetic and acoustic waves

지도 교수 박 남 규

이 논문을 공학박사 학위논문으로 제출함
2015 년 8 월

서울대학교 대학원
공과대학 전기컴퓨터공학부
구 석 모

구석모의 공학박사 학위논문을 인준함
2015 년 8 월

위 원 장 _____ 이병호 (인)

부위원장 _____ 박남규 (인)

위 원 _____ 이창희 (인)

위 원 _____ 민범기 (인)

위 원 _____ 신중화 (인)

Abstract

Top-down metamaterial design for enhancing extraordinary field focusing of electromagnetic and acoustic waves

Sukmo Koo

School of electric engineering, Nano photonics

The Graduate School

Seoul National University

Since their discovery by Ebbesen in 1998, extraordinary transmission and field enhancement of photonic waves have comprised a popular and important area of photonics research, including studies of light from a wide range of spectra (visible, infrared, THz, microwave) transmitted through various aperture geometries (Bow-tie, slit, hole antenna, NSOM, metamaterials). Extraordinary transmission of electromagnetic waves has been assumed to be impossible in the case of a focusing area size smaller than the metallic skin-depth, as the waves interact with metallic electrons only within the skin-depth of the surface.

The first part of this thesis addresses the extremely challenging problem of 3 mm wavelength light impinging on a 70 nm ($\lambda/40,000$) wide nanogap or nanowire, smaller than the skin-depth of 250 nm. Comparing effects of the complementary nanogap and nanowire structures, which should be identical by Babinet's principle, the

saturation point of the electric field enhancement in the nanogap was at the Thomas–Fermi length (<1 nm), much smaller than the skin–depth. The magnetic field enhancement in the nanowire was 100,000, which, while large, is much less than the electric field enhancement in the nanogap of 1,000,000; thus, Babinet’s principle does not hold in the extreme skin–depth domain. The extreme focusing in the nanogap could be utilized in nonlinear optical devices or nanosensor systems.

In the second part of this thesis, I designed metamaterials to enhance the focusing efficiency. For example, matched zero–index metamaterials could erase the effective space to increase collection of the light beyond the λ –zone limit. To design such metamaterials, I propose an entirely new top–down design strategy of the meta–atom, where the target ϵ_{eff} and μ_{eff} are first specified, and then, the design parameters are determined, inspired by fundamental oscillations of the elementary particle associated with the wave. To decouple the fundamental wave parameters ϵ_{eff} and μ_{eff} , envisaged by Pendry as an ideal platform for top–down and reconfigurable design of meta–atoms, I separated the anisotropic permittivity of the hypothetical meta–atom along radial (ϵ_r) and angular (ϵ_θ) directions. I analytically solved the inverse problem of the proposed structure design for the desired wave parameters; the design parameters ($\epsilon_r, \epsilon_\theta$) were determined to achieve matched zero–index properties ($\epsilon_{\text{eff}} = \mu_{\text{eff}} = 0$). I numerically demonstrated extraordinary transmission through a nanogap, 50 times greater than the previous λ –zone limit, utilizing the designed matched zero–index meta–atom.

Finally, I extended these concepts from electromagnetics to acoustics using the duality relation between the electromagnetic

(permittivity: ϵ , permeability: μ) and acoustic (density: ρ , compressibility: B^{-1}) wave parameters. As in the electromagnetic case, it is possible to decouple and independently control acoustic parameters ρ and B^{-1} by separating the membrane vibrations along the linear and radial directions. Parameter mapping of the analytical results shows the orthogonality between (ρ, B^{-1}) , and separated membrane parameters (m_0, m_1) , and visualizes the possibility of top-down design. Independent control of bianisotropy ξ , which arises from structural asymmetry, is realized theoretically and experimentally. Super-focusing and scattering through an asymmetric waveguide are demonstrated using bianisotropic pressure-velocity conversion.

Keywords : Nano photonics, Metamaterials, Photonic nano-focusing, Acoustics

Student Number : 2009-30177

Contents

Chapter 1. Introduction.....	1
1.1 Background.....	1
1.2 Motivation.....	5
1.3 The outline of thesis	8
Chapter 2. Background theory	10
2.1 FDTD (Finite difference time domain)	10
2.2 Super computer set-up	13
2.3 Rigorous Babinet's principle.....	14
2.4 Super-funneling through the bianisotropic matched zero index gap	14
2.5 Duality relation between electromagnetics and acoustics	18
2.6 Retrieving effective acoustic wave parameters from impedance tube	20
Chapter 3. Extraordinary electric and magnetic field enhancement in the nanogap and nanowire: Role of Surface Impedance in Babinet's Principle for Sub-Skin-Depth Regime	22
3.1 Introduction	22
3.2 Numerical analysis of the electric field enhancement in the nanogap	25
3.3 Analytical investigation of the perfect electric conductor nanogap and nanowire by solving rigorous scattering problem	30
3.4 Analytical and numerical investigation of the real metallic nanogap and nanowire	36
3.5 Effect of substrate	39
3.6 Discussion of role of surface impedance in the Babinet's principle for sub-skin-depth regime	43
3.7 Summary	47
3.8 Application to the switch.....	48
3.9 Application to the magnetic polarizer	50
Chapter 4. Decoupling of ϵ and μ with an anisotropic photonic meta-atom toward top-down design of metamaterials: Application to zero index super-λ funneling through a sub-λ nanoslit	58
4.1 Introduction	58
4.2 Analytical investigation of the hypothetical anisotropic meta-	

	atom	61
4.3	Dielectric implementation of the designed hypothetic anisotropic meta-atom	65
4.4	Metallic implementation of the designed hypothetic anisotropic meta-atom	68
4.5	Application to the super funneling through the nanoslit utilizing designed matched zero index meta-atom.....	70
4.6	Summary	74
Chapter 5. Inverse design of an acoustic omni meta-atom for the reconfigurable, full access to wave parameter space.....		75
5.1	Introduction	75
5.2	Derivation of acoustic macroscopic wave parameters from the electromagnetic first-principle homogenization theory	79
5.3	Ideal meta-atom platform of decoupling acoustic parameters	82
5.4	Application to the meta-surface example utilizing designed meta-atom	92
5.5	Concept extension to the bianisotropy and energy conversion	94
5.6	Summary	102
Chapter 6. Conclusion.....		103
References		106
한글초록.....		111

List of Figures

Fig. 1.1	Wave parameters of the previously reported electromagnetic and acoustic metamaterials.....	2
Fig. 1.2	Microwave cloaking using the cylindrical metamaterials [30]	3
Fig. 1.3	Visible light perfect absorber using metamaterials	3
Fig. 1.4	Super lens using hyperbolic metamaterials [26]	4
Fig. 1.5	Metamaterial bottom-up design using composite magnetic	

and electric meta-atom [23]	5
Fig. 1.6 Schematics of the λ -zone of (a) at the tip and (b) nano capacitor [34]. (c) Total scattering cross section of a plasmonic nano-rod with multi-degenerate resonance channels [35]	6
Fig. 1.7 Microwave cloaking based on the matched zero index metamaterials [4]	7
Fig. 2.1 Schematics of FDTD Algorithm	11
Fig. 2.2 Yee lattice for FDTD element	11
Fig. 2.3 Nonuniform orthogonal grid example	12
Fig. 2.4 The pictures of home-made CPU and GPU clusters.....	13
Fig. 2.5 The perfectly conducting screen (problem 1), and its complementary diffraction screen (2).	14
Fig. 2.6 The schematic of the problem where the Hz polarized light transmit through the slit. The dotted region is filled with homogenous matched zero index materials.....	15
Fig. 2.7 The schematic of the acoustic impedance tube set-up...	21
Fig. 3.1 The FDTD analysis of fields around nanogaps.....	27
Fig. 3.2 Diagram of the (a) nanogap and (b) nanowire structure having width w and infinitesimal thickness.....	30
Fig. 3.3 Field enhancement obtained through FDTD analysis for $\lambda = 3\text{mm}$. To bring out similar field pattern, we used PEC and thin ($t = 40\text{nm}$) metal structure. Width (w) for both structures is $1\mu\text{m}$. (a) E_x field enhancement at gap. (b) H_x field enhancement at wire.. ..	34
Fig. 3.4 (a) Magnetic field (H) enhancement for the nanowire plotted as a function of width: both analytical (lines) and FDTD analysis (+). (b) Field enhancement plotted as a function of t for nanowire (H) and nanogap (E , $\delta = 248\text{ nm}$, $w = 1\mu\text{m}$).....	37
Fig. 3.5 The schematics of nanogap and nanowire on the dielectric substrate.	39
Fig. 3.6 Field pattern for the nanogap and nanowire when the substrate exists. Profile of (a) Electric field (nanogap) and (b) Magnetic field (nanowire) ($w = 1\mu\text{m}$, $t_1 = 40\text{nm}$, $t_2 = 1\mu\text{m}$).....	40
Fig. 3.7 Electric and magnetic field enhancement for different substrate thickness. (dashed line: field enhancement when $t_2 = 0$, red circle: nanowire, blue circle: nanogap).	41
Fig. 3.8 Zoomed-in image of field enhancement obtained through FDTD analysis (Gold, $t = 100\text{nm}$, $w = 100\text{nm}$). The arrows represent the current flow (J) in the metal for (a) nanogap and (b) nanowire.	44
Fig. 3.9 Spatial distribution of the field enhancements at the exit side ($y = 100\text{ nm}$) obtained from FDTD for the same structures and	

material parameters as in Fig. 4. (a) nanogap and (b) nanowire..	45
Fig. 3.10 (a,b) Electric field and (c,d) current pattern of the nano-antennas for on and off state..	49
Fig. 3.11 Calculated field and current distributions around a subwavelength hole....	53
Fig. 3.12 (a) Scattering field polarizations for various hole diameters ($\theta = 70^\circ$, $\lambda = 780$ nm). (b) $\psi_{sc, E}$ vs. wavelength for a 100 nm hole punctured on 80 nm-thick gold on a sapphire substrate ($\theta = 70^\circ$, $\phi=45^\circ$; $\psi = 142^\circ$). (c) FDTD calculation (blue rectangle) of $\psi_{sc, E}$ when ψ is fixed at 135° using realistic gold and sapphire dielectric constants.....	55
Fig. 4.1 Physical origin of the electron induced electric (left) and magnetic (right) dipole moments of a classical atom	60
Fig. 4.2 (a) Schematic of the anisotropic meta-atom illuminated by TE plane wave. (b) Charge and (c) current distribution at the electric and magnetic resonance frequencies, respectively (arrows denote current flow). (d) Calculated ϵ_r and ϵ_θ values that give matched zero index property (solid: $R = 0.4a$, dashed: $R = 0.45a$). (e) ϵ_{eff} and μ_{eff} tunability including demonstration of matched index property ($n_{eff} = \pm 0.1$).....	61
Fig. 4.3 Anisotropic meta-atoms ($\epsilon_r \neq \epsilon_\theta$) of nano-pizza geometry with (a) 40 slices and (b) 8 slices. (inset in (a) shows an example of nano-donut). Calculated ϵ_{eff} and μ_{eff} for nano-pizzas of radius (c) $R = 0.4a$ ($a = 1.5$ cm), and (d) $R = 0.45a$ ($a = 600$ nm).....	66
Fig. 4.4 (a) Unit cell structure of the proposed metallic meta-molecule. (b, c) Hz field pattern (color) with Electric field (E) distribution (arrows) corresponding to (b) electric and (c) magnetic modes of the meta-molecule.....	68
Fig. 4.5 Demonstration of the decoupling μ from n_1 and also matched zero index response for the proposed meta-molecule. The plots show the spectra of (ϵ, μ) with changing (a) n_2 and (b) n_1 .	69
Fig. 4.6 (a) Schematic of the meta-atom coated slit structure (left) as an assembly of three parts (right). Deviation of effective permittivity $\Delta\epsilon$ before (dash-dot) and after (solid) tuning of (b) particle B in part III and (c) particle A in part II. Meta-atom of 8 slice nano-pizza (ϵ_1, ϵ_2) = (14.53, 179.2) were used. Green dash line denotes $f = 0.212$ c/a.....	70
Fig. 4.7 (a) Transmission spectra of the slit; without (green) and with zero-index meta-atom array of (blue) high index (ϵ_1, ϵ_2) = (14.53, 179.2) and (red) low index (2.22, 12.96) nano-pizza. f_0 is the frequency of matched zero index. (b, c) E_x field pattern near the nanoslit at f_0 , (b) with and (c) without the meta-atom array. (d-f)	

H_z field pattern of the slit at f_0 (d) without, (e) with high-index, and (f) with low-index nano-pizza meta-atom array. Slit width; 0.21λ (d, e) and 0.55λ (f).	72
Fig. 5.1 The schematics of meta-atom. p and q denote for average pressure and displacement for each cells and membranes. Arrows in q denote the positive directions	83
Fig. 5.2 Cylindrical bending of the membrane (gray) with fixed edge at the metallic boundary.....	85
Fig. 5.3 The portion of air (gray) area moving with membranes. (a) Outer ($m_{\text{air}} = 0.6\rho_0 s_0$), (b) inner membranes ($m_{\text{air}} = 0.5\rho_0 s_I + 0.25\rho_0 s_I$) in the meta-atom array, and (c) membranes at the interfaces ($m_{\text{air}} = 0.9\rho_0 s_0$) between meta-atoms and air.....	87
Fig. 5.4 Schematics and extracted parameters for proposed meta-atom. Demonstration of the complete quadrants of the effective parameters sets ($\rho = \pm 0.4$, $B^{-1} = \pm 0.1$) for the proposed meta-atom (inside dashed line).....	88
Fig. 5.5 Numerically extracted effective parameters of the meta-atom (designed to give matched zero index at 1500 Hz). (a) ρ and (b) B^{-1} spectra.....	90
Fig. 5.6 The outer membrane at the (a) internal unit cells and (b) interfaces.....	91
Fig. 5.7 Experimental results for reconfigurable meta-surface ..	93
Fig. 5.8 Schematics for nonzero bianisotropy of the proposed meta-atom when $\Delta b \neq 0$	96
Fig. 5.9 a) Schematic of the acoustic meta-atom. $\Delta b/2$ b) Wave parameter mapping of meta-atom reconfiguration. c) Wave impedance manipulation of bianisotropic medium. (d: thickness, $Z \rightarrow Z_1$ $Z \rightarrow Z_2$)	97
Fig. 5.10 Numerical demonstration of wave controlling by meta-surface..	98
Fig. 5.11 Design and the pressure field pattern of the bianisotropic meta-atom..	100
Fig. 5.12 The structure of in analysis of asymmetric tunneling with six bianisotropic meta-atoms ($\Delta b = 0.48$ mm) in the gap, and with matched zero index meta-atom array at the output side ($\Delta b = 0$). The analytically (blue and red line) and numerically calculated pressure field profile displayed (some data suppressed).....	101

Chapter 1.

Introduction

1.1 Background

1.1.1. Designing metamaterials

Metamaterials exhibiting naturally non-occurring refractive indices [1–29] and their applications to exotic forms of wave manipulation [30–33] are among the hottest research topics in nano-photonics today. The wave parameters of negative- [19–23], zero- [4,24], ultra-high- [12,25] index, hyperbolic [26], anisotropic [27], bianisotropic [28], and chiral [29] metamaterials have been explored and demonstrated.

The key parameters of metamaterials in nano-photonics and acoustics are sets of wave parameters, such as permittivity ϵ ,

permeability μ , density ρ , and compressibility β . All reported electromagnetic and acoustic metamaterials can be plotted in parameter space, as in Fig. 1.1. Materials in nature are usually distributed in quadrant I or II; artificially designed metamaterials with, for instance, negative refractive indices and magnetic permeabilities populate quadrants III and IV, completing the wave parameter space.

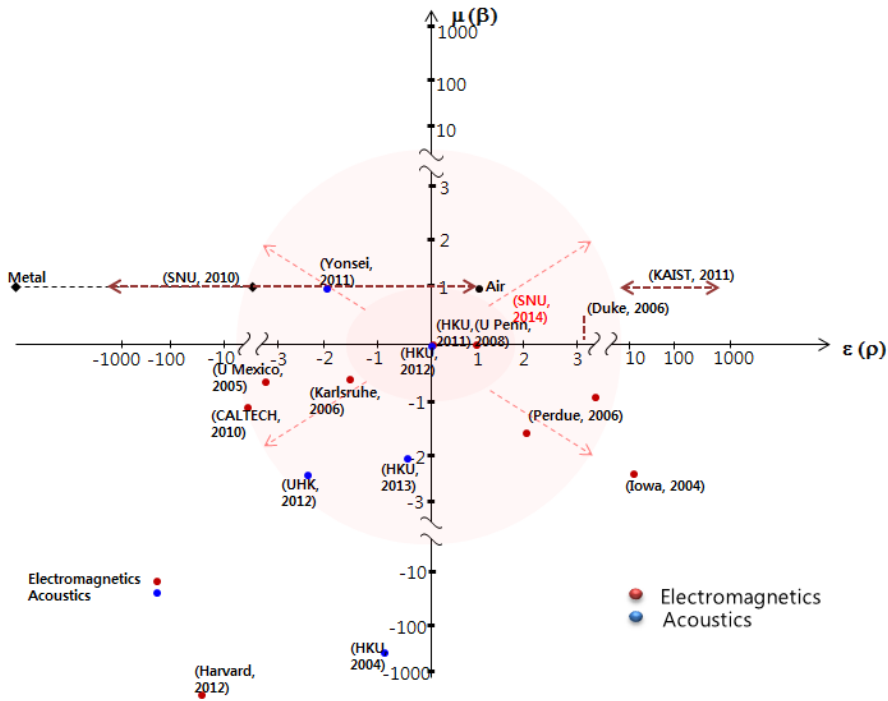


Fig.1.1 Wave parameters of previously reported electromagnetic and acoustic metamaterials [1–29]

1.1.2. Applications of metamaterials

As metamaterials realize otherwise non-existing material parameters, broad, distinct, and previously unrealized

applications have been reported, such as cloaking technologies, seismic wave blocking earthquake prevention methods, ultra-high resolution bio-sensors, sound insulators, ultra-thin optical super-lenses, and broad bandwidth solar cells. (Fig. 1.2–1.4)

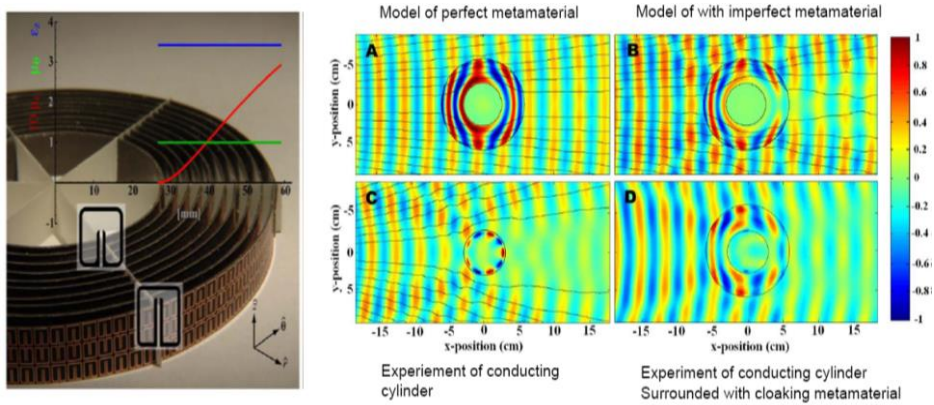


Fig. 1.2 Microwave cloaking using cylindrical metamaterials

[30]

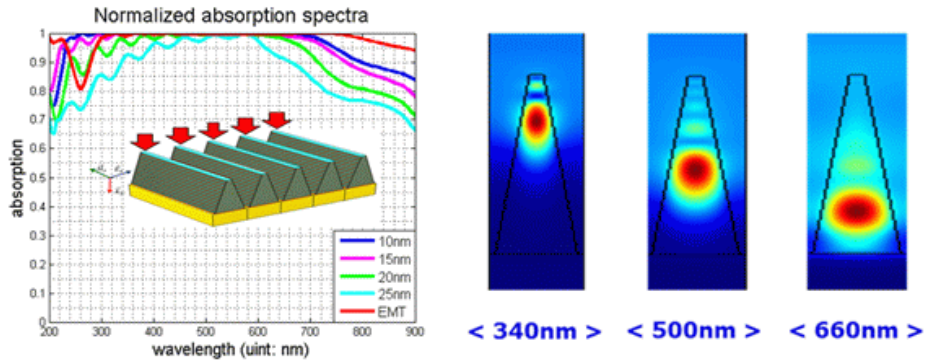


Fig. 1.3 Visible light perfect absorber made of metamaterials

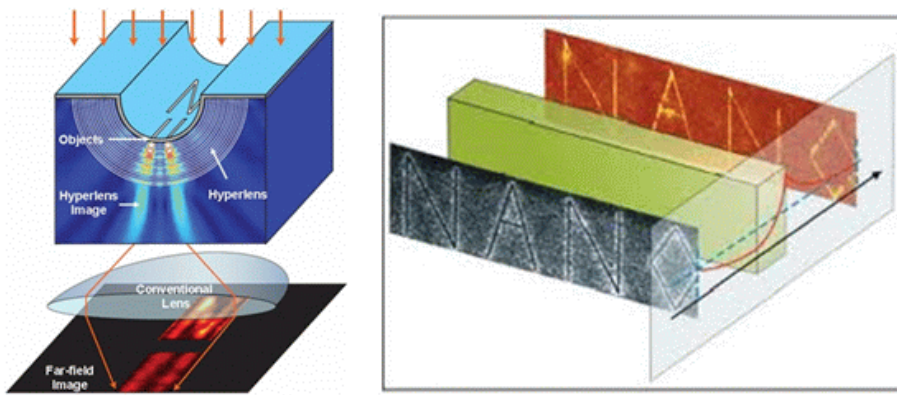


Fig. 1.4 Super-lens based on hyperbolic metamaterials [26]

1.2 Motivation

1.2.1. Metamaterial design methods

Early approaches to metamaterial design are based on retro-fit, bottom-up approaches, where the building blocks are initially proposed and the subsequent design is carried out through a series of iterative fabrications and guesswork, with the hope that the exotic properties will be realized. Moreover, as no existing physical mechanism can finely control the movement of bound charges in dielectrics, metamaterials have been intuitively designed largely with metallic inclusions that provide well-defined current paths for free charges (e.g., Fig. 1.5).

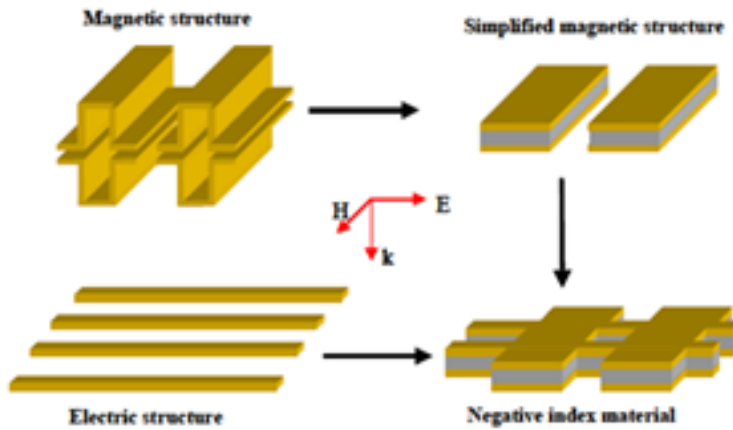


Fig. 1.5. Metamaterial bottom-up design using composite magnetic and electric meta-atoms [23]

However, the full accessibility of the entire wave parameter

space by existing meta-materials is still is an open question, and the existence of an omni-potent meta-atom for the reconfigurable, seamless access of wave parameter space is yet to be discovered. Motivated by the fundamental oscillations of the elementary particle associated with the wave, we propose a new paradigm in metamaterial design: a top-down approach, where the target ϵ and μ (ρ and β) are first specified, and the design parameters are subsequently determined.

1.2.2. Fundamental limit of focusing light

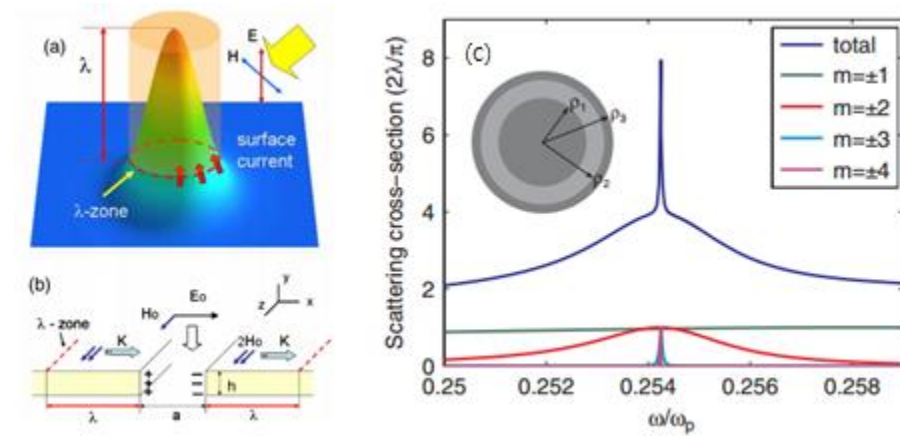


Fig. 1.6. Schematics of the λ -zone (a) illustrated for light E incident on a conducting surface and (b) in a nano capacitor [34]. (c) Total scattering cross section of a plasmonic nano-rod with multi-degenerate resonance channels [35].

The fundamental limit of confinement of light into a single nanostructure is determined by the maximum cross-section of the structure in terms of wavelength λ (3D: $3\lambda^2/2\pi$, 2D: $2\lambda/\pi$).

This limit is the λ -zone for a nano-capacitor, where the charging area is determined by the spatial regions indicated in Fig. 1.6(a, b) [34]. One method to exceed this limit is to increase the scattering channels with multiple resonances using plasmonic waves, as shown in the structure in Fig. 1.6(c) [35].

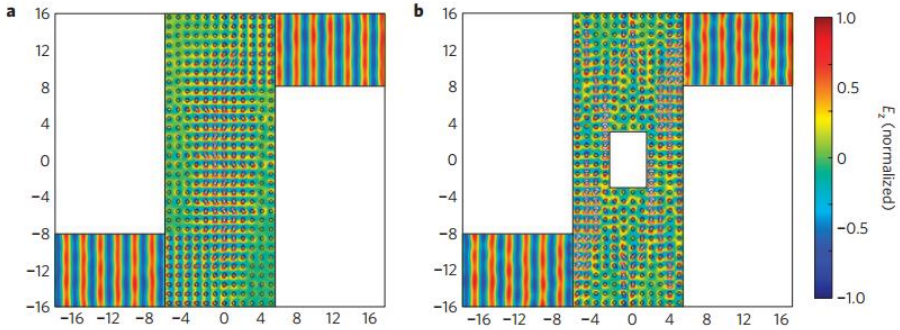


Fig. 1.7. Microwave cloaking based on matched zero-index metamaterials [4]

Another method uses matched zero-index metamaterial to overcome the λ -zone limit, and has been used mainly to cloak structures like those shown in Fig. 1.7 [4]. This metamaterial allows for 100% transmission through the nanogap by effectively removing the space to zero, even though the light collection width is far beyond the λ -zone.

1.3 Outline of the thesis

This thesis describes intense analyses and applications of extraordinary field enhancement on nano-structures. In addition, matched zero-index and bianisotropic metamaterials are utilized to focus the field beyond the λ -zone limit.

In chapter 2, background theories and experimental set-ups are introduced to understand the research methods. Numerical cluster and finite-difference time-domain (FDTD) calculations, impedance tube acoustic experimental set-up, and background theory, such as Babinet's principle, are described.

In chapter 3, analytical and numerical investigations of the extraordinary electric and magnetic field enhancement at a nanogap and nanowire is performed based on Babinet's principle. The effects of skin-depth and surface impedance on Babinet's principle are discussed. Example applications of a Bethe's hole magnetic polarizer and octave bandwidth THz antenna are introduced and numerically analyzed.

In chapter 4, super- λ funneling of the nanogap beyond the λ -zone limit is demonstrated using matched zero-index metamaterials. A novel strategy for top-down metamaterial design is proposed based on dielectric and metallic platforms; the target ϵ_{eff} and μ_{eff} are first specified, and then, the design

parameters are determined, inspired by fundamental oscillations of the elementary particle associated with the wave.

In chapter 5, the top-down metamaterial design strategy is applied to acoustic waves. The concept is extended beyond the decoupling of parameters ρ and B^{-1} to controlling ξ for the proposed platform. Example applications to a meta-surface and bianisotropic energy conversions are numerically and experimentally demonstrated.

Chapter 2.

Background theory

2.1 FDTD (Finite difference time domain)

FDTD [36] is the computational numerical algorithm for solving the fundamental physical equations (e.g. Maxwell's equation in electromagnetic domain) in the time domain. For this, the algorithm uses discrete space which has been divided sufficiently to reflect continuous real space. The schematics and Yee lattice for the FDTD element is described in Fig. 2.1 and Fig. 2.2.

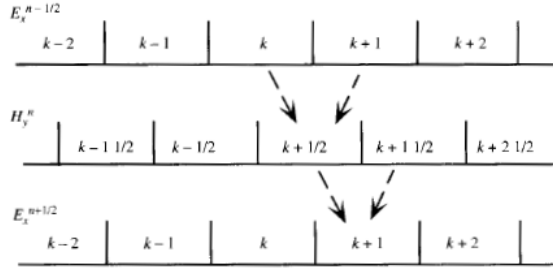


Fig. 2.1. Schematics of FDTD Algorithm

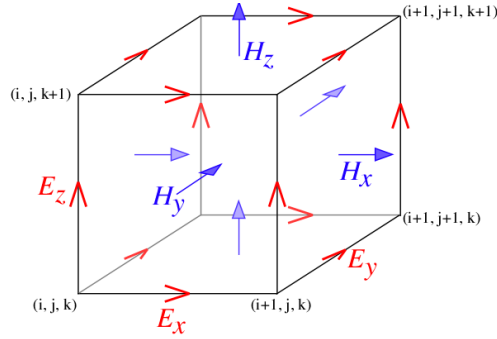


Fig. 2.2. Yee lattice for FDTD element

The size of the cell is usually determined by the wavelength ($\Delta x < \lambda/20$). The time step size is determined by the Δx , the convergence condition could be expressed by $\Delta t \leq \frac{\Delta x}{2\sqrt{n}c}$, for n dimensional space, where c is the speed of light. Also, non-uniform grids are used to treat extreme problem by reducing the memory space and computational time described in Fig. 2.3. The recommendation to reduce the error is maintaining the ratio of the cell size less than 2 between the adjacent cells.

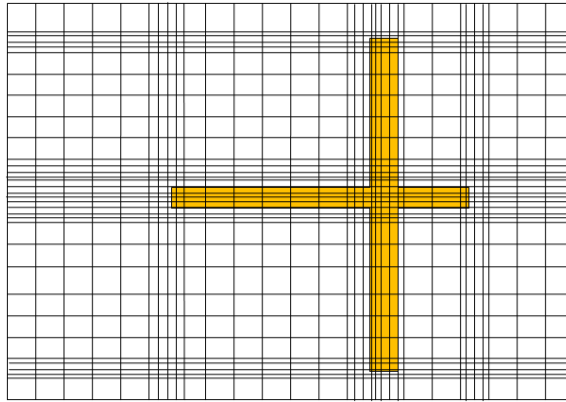


Fig. 2.3. Nonuniform orthogonal grid example

2.2. Super computer set-up

For the numerical analysis of the extensive physical problem in nanophotonics and acoustics, I have set-up the 256-core CPU cluster and 32-GPU clusters as shown in Fig. 2.4. The programming has been performed based on the MPI, C++ and CUDA. The CPU cluster with total memory 512GB can handle maximum 2×10^9 ($= 2000 \times 1000 \times 1000$) problem spaces. The GPU is specialized to the computational speed, 10 times faster than CPU was achieved for our FDTD algorithm.



Fig. 2.4. The pictures of home-made CPU and GPU clusters

2.3. Rigorous Babinet's principle

The useful relation called Babinet's principle [37] is a theorem concerning diffraction pattern from a certain shaped perfectly conducting plane screen is identical to that from a complementary screen as shown in Fig. 2.5.

The rigorous expression of Babinet's principle could be easily derived from the well-known boundary conditions in M (Perfect conductor, $E_x = E_z = 0$) and A (Continuity, $H_x^{(s)} = H_z^{(s)} = 0$) as below,

$$\left(\begin{array}{l} (E_{1x}^{(s)}, E_{1z}^{(s)}) = -(E_{1x}^{(i)}, E_{1z}^{(i)}) \text{ on } M \\ H_{1x}^{(s)} = H_{1z}^{(s)} = 0 \text{ on } A \end{array} \right) \quad \text{problem (1)} \quad (2.1)$$

$$\left(\begin{array}{l} (H_{2x}, H_{2z}) = (H_{2x}^{(i)}, H_{2z}^{(i)}) \text{ on } A \\ E_{2x} = E_{2z} = 0 \text{ on } M \end{array} \right) \quad \text{problem (2)}$$

where (s), (i) denotes scattering and incident field. From equation (2.1), it is clear to produce required form of Babinet's principle between complementary screen: $\mathbf{H}_2 = -\mathbf{E}_1^{(s)}$.

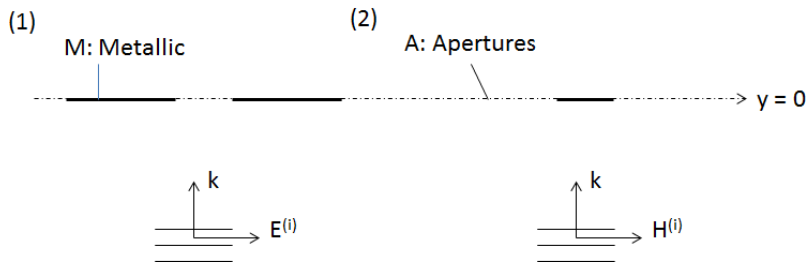


Fig. 2.5. The perfectly conducting screen (problem 1), and its complementary diffraction screen (2).

2.4. Super-funneling through the bianisotropic matched zero index gap

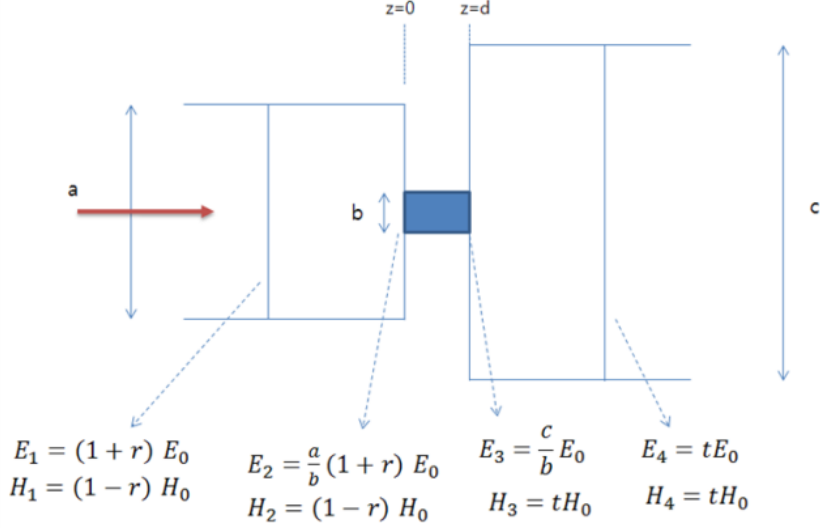


Fig. 2.6. The schematic of the problem where the H_z polarized light transmit through the slit. The dotted region is filled with homogenous matched zero index materials.

In this section, we analytically solve the tunneling problem that the impedance of input and output waveguide is different. We found that 100% transmission is possible utilizing the new kind of pseudo-chiral zero-index metamaterial, where the real part of ϵ and μ is zero, with non-zero ξ . This metamaterial is usually designed using Ω -shaped structure, where the locations of the electric and magnetic responses are split, to give non-zero pseudo chirality. Combining Ω -shaped unit cell and the nano-pizza, the non-zero pseudo chirality with matched zero index is designed and demonstrated. Our new investigation of pseudo-

chiral ZIM (zero index metamaterials) generalizes the concept of ZIM, with bridging different light impedance mode, between far-field and nano-structured waveguide.

Fig. 2.6 shows the problem of our consideration. With the H_z polarized light comes from left side, the dotted region is filled with matched ZIM ($\varepsilon = \mu = 0$). When we denote reflection and transmittance of this structure as r and t , we can calculate the field on the boundary from the definition of the ZIM, which is

$$\begin{aligned} E_1 &= (1+r)E_0, H_1 = (1-r)H_0 \\ E_2 &= \frac{a}{b}(1+r)E_0, H_2 = (1-r)H_0 \\ E_3 &= \frac{c}{b}tE_0, H_3 = tH_0 \\ E_4 &= tE_0, H_4 = tH_0 \end{aligned} \quad (2.2)$$

Now we establish the wave equation inside the blue area, with unknown properties of index n and impedances (z_+ and z_-), for bianisotropic media [28], which is

$$\begin{aligned} E &= E_{2+}e^{-jk_0nx} + E_{2-}e^{jk_0nx} \\ H &= \left(\frac{1}{z_+}E_{2+}e^{-jk_0nx} - \frac{1}{z_-}E_{2-}e^{jk_0nx}\right) \end{aligned} \quad (2.3)$$

Our final aim is to achieve 100% transmittance through the slit, which $r=0$ and $t=\sqrt{c/a}$. From (2.2) and (2.3), it is possible to achieve the solution for n , z_+ , z_- (or ε , μ , ξ) in the slit, applying continuous boundary condition for electric and magnetic field. Expressing as $\varepsilon [= 2n/(z_++z_-)]$, $\mu [= 2z_+z_-n/(z_++z_-)]$ and $\xi [= \ln(z_+-z_-)/(z_++z_-)]$,

$$\varepsilon = \mu = 0 \quad \text{and} \quad \xi = -\frac{1}{2kd} \ln\left(\frac{c}{a}\right). \quad (2.4)$$

When the impedances of the input and output waveguides are identical ($a = c$), the solutions of ε , μ and ξ are zero at the same time to achieve 100% transmittance, which agrees with the previous results for matched ZIM. In contrast, for the case of $a \neq c$, the required ξ is nonzero. The metamaterial of such property can be achieved using pseudo-chiral metamaterial. In addition, the ε and μ of the metamaterial has to be controlled, to remain zero.

2.5. Duality relation between electromagnetics and acoustics

In this section, we express the duality relation of electromagnetic and acoustic waves, which the exact equivalence has long been known that for 2D cases [38]. Starting from the fundamental acoustic equation for the inviscid fluid with zero shear modulus,

$$\rho \frac{\partial \mathbf{v}}{\partial t} = -\nabla p, \quad \frac{\partial p}{\partial t} = -B \nabla \bullet \mathbf{v} \quad (2.5)$$

where p is pressure, \mathbf{v} is the fluid velocity, ρ is the fluid density, B is the bulk modulus. We know then express (1) into the Cartesian coordinates (x, y, z) with using $\exp(j\omega t)$ convention as below.

$$\begin{aligned} -j\omega\rho_y v_y &= \frac{\partial(-p)}{\partial y}, \quad -j\omega\rho_x (-v_x) = -\frac{\partial(-p)}{\partial x}, \\ j\omega B^{-1}(-p) &= \frac{\partial(-v_x)}{\partial x} - \frac{\partial v_y}{\partial y} \end{aligned} \quad (2.6)$$

It is also possible to express 2D Maxwell equation in the same form assuming transverse magnetic polarization in cylindrical coordinates.

$$\begin{aligned} -j\omega\varepsilon_x E_x &= \frac{\partial H_z}{\partial y}, \quad -j\omega\varepsilon_y E_y = -\frac{\partial H_z}{\partial x}, \\ j\omega\mu_z H_z &= \frac{\partial E_y}{\partial x} - \frac{\partial E_x}{\partial y} \end{aligned} \quad (2.7)$$

The equations (2.6) and (2.7) could be arranged to highlight exact duality between two waves under the variable exchange.

$$[\varepsilon_x, \varepsilon_y, \mu_z, E_x, E_y, H_z] \leftrightarrow [\rho_y, \rho_x, B^{-1}, v_y, -v_x, -p] \quad (2.8)$$

2.6. Retrieving effective acoustic wave parameters from impedance tube

To extract effective parameters (ρ , B^{-1} , ξ) of the meta-atom experimentally, we measure S-parameters with using impedance tube set-up. As shown in Fig. 2.7 of the schematic view of this set-up, the microphones are used to measure the pressure values for each location. The relation between p_1 , p_2 , p_3 , p_4 and S_{11} , S_{21} is easily derived as below assuming symmetric case ($S_{11} = S_{22}$, $S_{12} = S_{21}$).

$$S_{11} = -\frac{p_{1-}p_{1+} - p_{2-}p_{2+}}{p_{1+}^2 - p_{2-}^2}, S_{21} = -\frac{p_{1-}p_{2-} - p_{2+}p_{1+}}{p_{1+}^2 - p_{2-}^2} \quad (2.9)$$

where

$$p_{1+} = \frac{2(p_1 e^{ikx_2} - p_2 e^{ikx_1})}{j \sin[k(x_1 - x_2)]}, p_{1-} = \frac{2j(p_1 e^{-ikx_2} - p_2 e^{-ikx_1})}{\sin[k(x_1 - x_2)]}, p_{2+} = \frac{2(p_3 e^{ikx_2} - p_4 e^{ikx_1})}{j \sin[k(x_1 - x_2)]},$$

$$p_{2-} = \frac{2j(p_3 e^{-ikx_2} - p_4 e^{-ikx_1})}{\sin[k(x_1 - x_2)]} \text{ and } k \text{ is the wavevector in the pipe } (\sim 2\pi f/343 \text{ (m}^{-1}\text{)}).$$

Moreover, the (2.9) could be generalized to treat the asymmetric case ($S_{11} \neq S_{22}$, $S_{12} \neq S_{21}$), by assuming no incident wave from port 2 ($p_{2-} = 0$). For this, the porous material has been used at the right-end of the pipe to absorb the sound without reflection. For our case, less than 5% reflection rate of the sound achieved using cone-shaped poly-urethane.

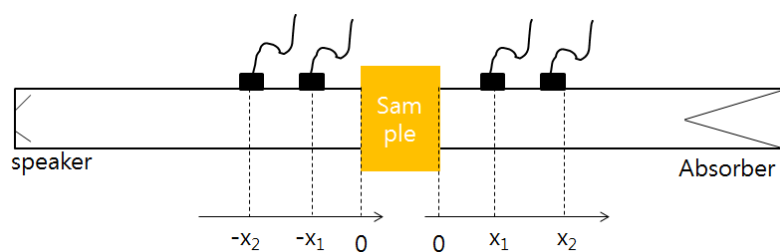


Fig. 2.7. The schematic of the acoustic impedance tube set-up.

Chapter 3.

Extraordinary electric and magnetic field enhancement in the nanogap and nanowire: Role of Surface Impedance in Babinet' s Principle for Sub-Skin-Depth Regime

3.1. Introduction

We propose and analyze the ‘complementary’ structure of a metallic nanogap, namely the metallic nanowire for magnetic field enhancement. Huge enhancement of the field up to factor of 300 was achieved. Introducing surface impedance concept, we also develop and numerically confirm a new analytic theory which successfully predict the field enhancement factors for

metal nanostructures. Compared to the predictions of the classical Babinet's principle applied to nanogap, orders of magnitude difference in the field enhancement factor was observed for the sub skin-depth regime nanowire.

It is well known that nano-sized metallic structures such as nanogaps can achieve huge electric field enhancement through the phenomena of Extraordinary Transmission (EOT) [39–49]. Recent development on EOT includes demonstration of non-resonant, factor of 1,000 enhancements in the electric field, through a $\lambda/40,000$ slit on metal films and thereby extending the concept of extraordinary transmission deep into the sub-skin-depth regime [49]. Considering the increasing attention towards magnetic field enhancement with its potential application – such as in magnetic nonlinearity and devices based thereon [50,1], – achieving magnetic field enhancement is as important an issue in nanophotonics as achieving electric field enhancement. Though a simple approach to achieve this goal can be found in the well-known Babinet's principle [37], considering the non-ideal nature of real metal, an in-depth investigation of Babinet's principle is warranted. As an example, the partial disagreement of experimental results with the predictions of Babinet's principle in [52] has been attributed to the non-ideal nature of real metals and possibly fabrication error in the sample.

In this chapter, motivated by Babinet's principle, we propose the metallic nanowire (complementary of nanogap in [49], which could be fabricated for example, by using the method in [53]) to achieve extraordinary magnetic field enhancement by a

factor of 300. Further, for the first time to the best of our knowledge, we also develop a comprehensive theory to explain the difference in field enhancement between the electric and magnetic fields in complementary metallic nanostructures, and to correctly predict the enhancement of magnetic field in the sub skin-depth regime. In sharp contrast to the predictions of the classical Babinet's principle applied to the result of [49] – where the enhancement factor of electric field scaled only with the inverse of gap-width, our analysis shows that the magnetic field enhancement of nanowire has strong dependence on the fundamental scaling length - metal skin depth. Orders of difference in the field enhancement were observed between nanogap and nanowire. Results show excellent agreement of the developed theory with the FDTD analysis.

3.2. Numerical analysis of the electric field enhancement in the nanogap

For a better understanding and optimization of our nanogap structure, two-dimensional finite-difference time-domain (FDTD) analysis was carried out. It is important to note that, regarding the problem of extending the size from the centimetre scale (sample dimension) down to nanometre (metal grid) ranges, asymptotically varying grid sizes were used. For the highly varying field inside the metal and at the nanogap, a 2.5-nm grid size was used, which gradually becomes larger as the process shifts away from the metal/nanogap region, up to 25 μm for fields in air. Convergence of this asymptotic grid size control was also confirmed by testing different grid densities (in a factor of 2 for each axis) in the two-dimensional FDTD, to verify field amplitudes converging to the solution with less than 2% of errors over the whole simulation space ($10 \times 2.5 \text{ mm}^2$). To implement the response of real metal in the FDTD analysis within the frequency range of interest, the Drude model was adopted for the calculation of the dielectric parameters of the metal (gold) [54]:

$$\varepsilon(\omega) = \varepsilon_{\infty} - \frac{\omega_p^2}{\omega(\omega + i\gamma)}$$

where $\varepsilon_{\infty} = 1$, plasma frequency $\omega_p = 1.37 \times 10^4 \text{ THz}$ and $\gamma = 40.7 \text{ THz}$ for gold. Notably, the skin depth at 0.1 THz is 250 nm, clearly larger than the 70-nm gap width or the 60-nm film thickness.

Fig. 3.1 shows the horizontal electric field pattern obtained from full-scale numerical analysis at 0.1 THz (wavelength 3 mm), zoomed-in on an area of $700 \times 700 \text{ nm}^2$ with a 500-nm gap sample ($h = 60 \text{ nm}$). The field enhancement at the gap is ~ 200 relative to the unperturbed incident field. We now narrow the gap to 70 nm, as shown in Fig. 3(b). The field enhancement is much stronger here than with a 500-nm gap; it is more than 1,000 at its maximum. This prediction of an increasing field enhancement with a decreasing gap beyond the skin depth regime is consistent with the simple concept here of charges concentrating towards the gap region as the gap closes. It is also in good agreement with the experimentally obtained field enhancement of 800. It is worth noting that the field is completely concentrated at the nanogap without penetrating into the metal, even with the nanogap size of 70 nm, which is much smaller than the skin depth of 250 nm. This is because the horizontal electric field at the gap is normal to the gap wall, at which point it is terminated by surface charges. The vertical electric field shown in Fig. 3.1(c) is also concentrated on the immediate vicinity of the gap and is terminated by surface charges on the metal plane. Note that the size of the surface charge spread is close to the gap width, consistent with our picture that charges move closer and closer to the edges as the gap narrows, most likely due to the attraction of opposite charges.

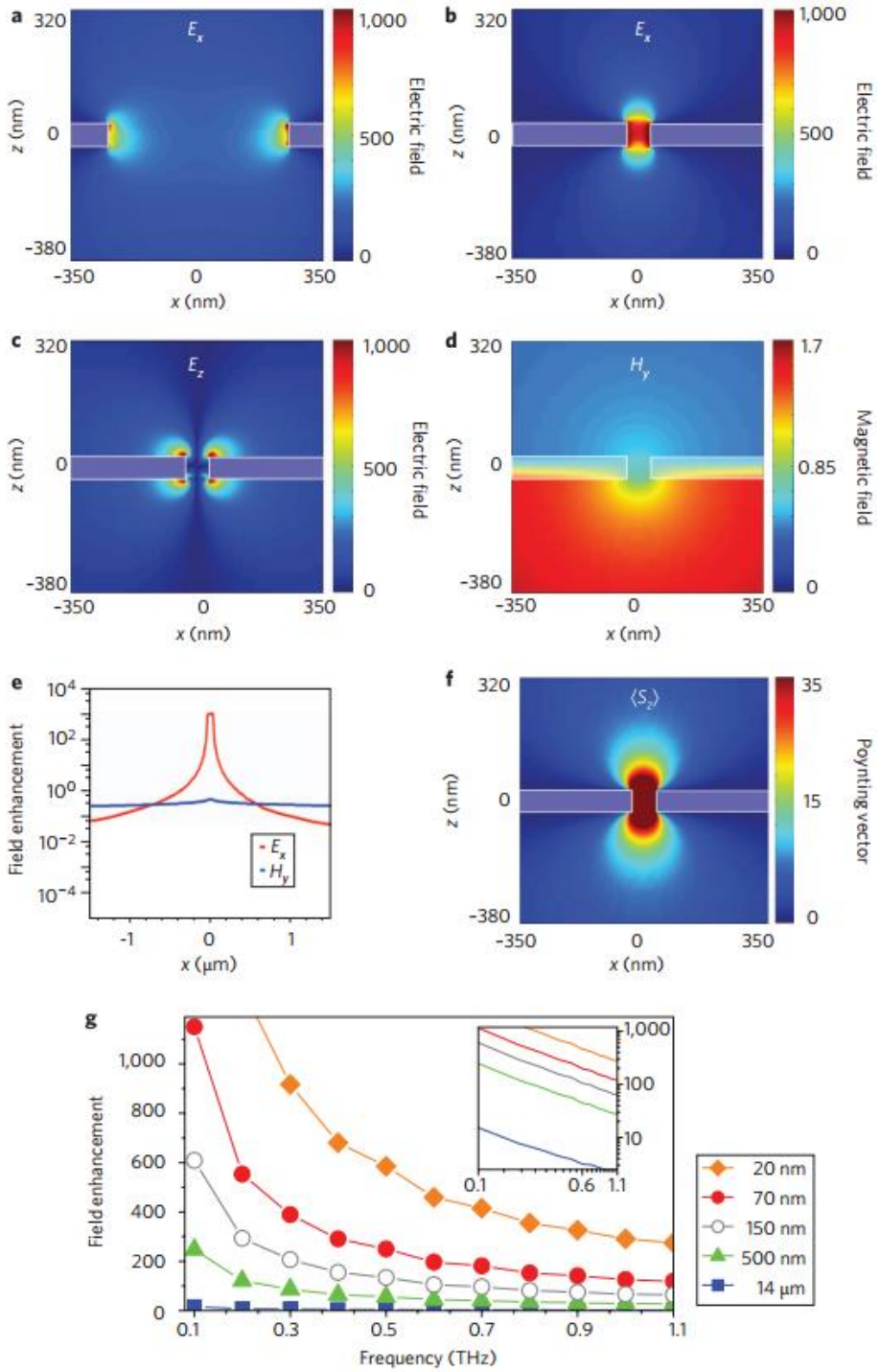


Fig. 3.1. The FDTD analysis of fields around nanogaps. (a) Simulated horizontal electric field around a 500-nm gap at 0.1 THz. (b) E_x , (c) E_z , and (d) H_y . (e) Cross-sectional plot of the

horizontal electric and magnetic fields at the exit side. (f) Time-averaged Poynting vector component $\langle S_z \rangle$. (g) Frequency dependent horizontal electric field at the exit plane measured mid-gap for gap widths

In stark contrast to the strong horizontal electric field that is focused on the gap region, the magnetic field H_y (Fig. 3.1d) is much more spread out, with essentially no enhancement. It also penetrates deeply into the metallic region, consistent with the skin depth. Fig. 3.1e shows the E_x and H_y fields calculated at an effective distance of 2.5 nm above the exit plane (in logarithmic scale). Although the magnetic field stays mostly constant in this length scale, of order 1, the horizontal electric field at the gap is orders of magnitudes stronger than the magnetic field. Once we move away from the centre of the nanogap into the top of the metallic surface, the electric field becomes weaker than the magnetic field. To demonstrate the energy flow through the nanogap, Fig. 3.1f shows a plot of the time-averaged Poynting vector $\langle S_z \rangle$, where concentration of light energy at the sub-skin-depth gap is apparent. What is striking is that the Poynting vector enhancement is much smaller than what simple multiplication of electric and magnetic fields suggests, indicating that the phase difference between the enhanced (charge-induced) electric field and impinging magnetic fields is close to 90° in this quasistatic regime.

Finally, the frequency and width dependence of the average electric field enhancement at the gap $\langle E_{\text{near}} \rangle / E_{\text{inc}}$, shown in Fig. 3g, reproduce the experimentally observed field enhancement

well, quantitatively as well as qualitatively, including the $1/f$ -type dependence and the increasing enhancement with decreasing a . The film thickness was 60 nm for $a = 70$ nm and $a = 500$ nm, 150 nm for $a = 150$ nm, and $17\text{ }\mu\text{m}$ for $a = 14\text{ }\mu\text{m}$. In simulation, a nanogap of size 20 nm was also considered to probe the possibility of enhancing the nanogap performance with smaller gap width. Indeed, larger enhancement is seen with the 20-nm gap ($h = 60$ nm), still maintaining the $1/f$ dependence, indicating that our scheme would work for even smaller gap sizes. Analysing the current distribution inside the conductor and the surface charge distribution near the nanogap shows that while the current distribution is nearly frequency-independent apart from the trivial $e^{-i\omega t}$ dependence, the surface charges at the nanogap contain the necessary $1/f$ term. This dependence, which is universal in any capacitor problem with an alternating current source, is therefore consistent with the terahertz light field-induced, harmonically oscillating currents charging the nanogap, with the charging time inversely proportional to the driving frequency.

3.3. Analytical investigation of the perfect electric conductor nanogap and nanowire by solving rigorous scattering problem

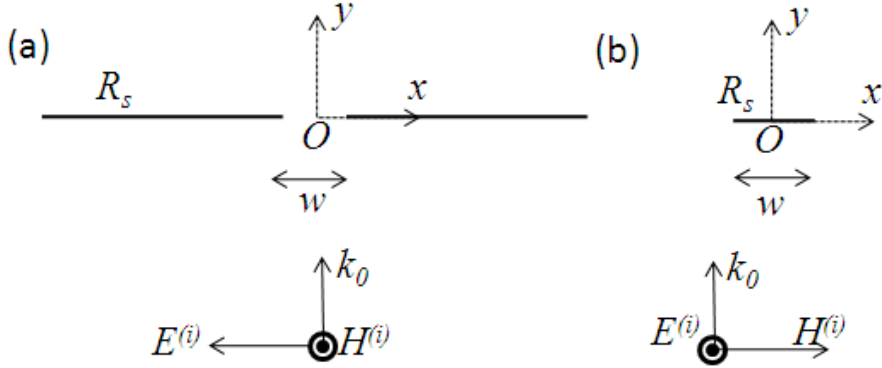


Fig. 3.2. Diagram of the (a) nanogap and (b) nanowire structure having width w and infinitesimal thickness. R_s is the surface resistivity of the metal in ohms per square, and Z is the free space impedance. The structure is illuminated by the TM (TE) wave for the nanogap (nanowire) having wavelength $\lambda_0 = 2\pi/k_0$. The superscript (i) denotes incident fields.

Fig. 3.2 shows the system under consideration. Fig. 3.2(a) is the nanogap and Fig 3.2(b) is the nanowire. A plane wave of wavelength λ_0 impinges normally on these structures. The polarization considered is transverse magnetic (TM) for the nanogap and transverse electric (TE) for the nanowire. For the present, the thickness of the structure is assumed to be infinitesimal so as to isolate the effect of non-zero impedance of the real metal on the complementary scattering behavior. The effects of finite thickness on the scattering are discussed

later. R_s stands for the surface resistivity in ohms per square. When $R_s = 0$, the metal becomes a perfect electric conductor (PEC).

The field H_z (E_z) for the TM (TE) wave in free space for 2D problems can be expressed as below.

$$\frac{\partial^2 H_z(E_z)}{\partial x^2} + \frac{\partial^2 H_z(E_z)}{\partial y^2} + k_0^2 H_z(E_z) = 0 \quad (3.1)$$

A general solution of (3.1) can be expressed as a linear combination of plane waves. With the scattering objects at $y = 0$, following the procedures in [37], the scattered field components can be shown to be as

$$\begin{aligned} H_z^{(s)} &= \pm \int_C P(\cos \alpha) \exp(ik_0 r \cos(\theta \mp \alpha)) d\alpha \\ E_x^{(s)} &= -Z \int_C \sin \alpha P(\cos \alpha) \exp(ik_0 r \cos(\theta \mp \alpha)) d\alpha \\ E_y^{(s)} &= \pm Z \int_C \cos \alpha P(\cos \alpha) \exp(ik_0 r \cos(\theta \mp \alpha)) d\alpha \\ E_z^{(s)} &= \int_C P(\cos \alpha) \exp(ik_0 r \cos(\theta \mp \alpha)) d\alpha \\ H_x^{(s)} &= \pm \frac{1}{Z} \int_C \sin \alpha P(\cos \alpha) \exp(ik_0 r \cos(\theta \mp \alpha)) d\alpha \\ H_y^{(s)} &= -\frac{1}{Z} \int_C \cos \alpha P(\cos \alpha) \exp(ik_0 r \cos(\theta \mp \alpha)) d\alpha \end{aligned} \quad (3.2)$$

$$\begin{aligned} H_x^{(s)} &= \pm \frac{1}{Z} \int_C \sin \alpha P(\cos \alpha) \exp(ik_0 r \cos(\theta \mp \alpha)) d\alpha \\ H_y^{(s)} &= -\frac{1}{Z} \int_C \cos \alpha P(\cos \alpha) \exp(ik_0 r \cos(\theta \mp \alpha)) d\alpha \end{aligned} \quad (3.3)$$

respectively for TM and TE incidence. Here k_0 and Z are the wavenumber and impedance respectively in free space. C is the path in the complex α plane along which $\cos \alpha$ ranges through real values from $-\infty$ to ∞ [37]. The superscript (s) denotes scattered components ($E = E^{(i)} + E^{(s)}$, $H = H^{(i)} + H^{(s)}$) and the upper sign is for $y > 0$ and the lower sign is for $y < 0$.

The boundary conditions for infinitesimally thin metals are well-known [53] and so are the symmetry conditions on the scattered fields [37], as given below.

$$\left(\begin{array}{l} \hat{\mathbf{n}} \times (\mathbf{E}(y=0+) - \mathbf{E}(y=0-)) = 0 \\ R_s \mathbf{J}_s = R_s [\hat{\mathbf{n}} \times (\mathbf{H}(y=0+) - \mathbf{H}(y=0-))] = -\hat{\mathbf{n}} \times \hat{\mathbf{n}} \times \mathbf{E}(y=0) \end{array} \right) \begin{array}{l} \text{on air} \\ \text{on metal} \end{array} \quad (3.4)$$

$$\left(\begin{array}{l} H_x^{(s)}(y=0+) = -H_x^{(s)}(y=0-) \\ H_y^{(s)}(y=0+) = H_y^{(s)}(y=0-) \\ H_z^{(s)}(y=0+) = -H_z^{(s)}(y=0-) \end{array} \right) \quad \left(\begin{array}{l} E_x^{(s)}(y=0+) = E_x^{(s)}(y=0-) \\ E_y^{(s)}(y=0+) = -E_y^{(s)}(y=0-) \\ E_z^{(s)}(y=0+) = E_z^{(s)}(y=0-) \end{array} \right) \quad (3.5)$$

Here \mathbf{n} is the outward unit vector parallel to the $+y$ direction and \mathbf{J}_s is the surface current density. Now putting (3.2), (3.3) into (3.4) and (3.5) we can arrive at the dual integral equations to be solved for $P(\cos \alpha)$. At $y = 0+$, with $\cos \alpha = \mu$, for nanogap (3.6) and nanowire (3.7) we get,

$$\left(\begin{array}{l} \int_{-\infty}^{\infty} \frac{P(\mu)}{\sqrt{1-\mu^2}} \exp(ik_0 x \mu) d\mu = 0, \\ \int_{-\infty}^{\infty} \left(\frac{2R_s}{\sqrt{1-\mu^2}} + Z \right) P(\mu) \exp(ik_0 x \mu) d\mu = E^{(i)}, \end{array} \right) \begin{array}{l} (|x| < \frac{w}{2}) \\ (|x| > \frac{w}{2}) \end{array} \quad (3.6)$$

$$\left(\begin{array}{l} \int_{-\infty}^{\infty} \left(\frac{1}{\sqrt{1-\mu^2}} + 2 \frac{R_s}{Z} \right) P(\mu) \exp(ik_0 x \mu) d\mu = -ZH^{(i)}, \\ \int_{-\infty}^{\infty} P(\mu) \exp(ik_0 x \mu) d\mu = 0, \end{array} \right) \begin{array}{l} (|x| < \frac{w}{2}) \\ (|x| > \frac{w}{2}) \end{array} \quad (3.7)$$

Using the convolution theorem [55] from spectral analysis, we can express (3.6) and (3.7) as, for nanogap (3.8) and nanowire (3.9)

$$\left(\begin{array}{l} \int_{-\infty}^{\infty} E_x^{(s)}(x') c(x-x') dx' = 0, \\ -\frac{k_0 R_s}{Z\pi} \int_{-\infty}^{\infty} E_x^{(s)}(x') c(x-x') dx' - E_x^{(s)}(x) = E^{(i)}, \end{array} \right) \begin{array}{l} (|x| < \frac{w}{2}) \\ (|x| > \frac{w}{2}) \end{array} \quad (3.8)$$

$$\begin{cases} \frac{k_0}{2\pi} \int_{-\infty}^{\infty} H_x^{(s)}(x') c(x-x') dx' + 2 \frac{R_s}{Z} H_x^{(s)}(x) = -H^{(i)}, (|x| < \frac{w}{2}) \\ H_x^{(s)}(x) = 0, (|x| > \frac{w}{2}) \end{cases} \quad (3.9)$$

where

$$c(x) = \int_{-\infty}^{\infty} \frac{1}{\sqrt{1-\mu^2}} \exp(ik_0 x \mu) d\mu = \pi(J_0(k_0 x) + iY_0(|k_0 x|))$$

and w is the width of the nanogap/nanowire (Fig.1). Here $J_0(x)$ and $Y_0(x)$ are Bessel functions of the first and second kinds of order zero respectively. Considering that $k_0 w$ will be very small, the Bessel functions can be approximated in terms of $k_0 w$ and $\ln(k_0 w)$. Further, using the average field values, $E_{x0}(R_s)$ (gap) and $H_{x0}(R_s)$ (wire) for the range $|x| < w/2$ in (3.8) and (3.9) respectively, we get expressions for Electric [Magnetic] field strengths for PEC ($R_s = 0$) as

$$E_{x0}(R_s = 0)[H_{x0}(R_s = 0)] \cong \frac{E^{(i)} [-H^{(i)}]}{k_0 w (0.5 + \frac{i}{\pi} (\ln(k_0 w/4) - \gamma - 1))} \quad (3.10)$$

For cases of real metal (non zero R_s), we also obtain,

$$\begin{cases} \frac{E_{x0}(R_s)}{E^{(i)}} \cong \frac{E_{x0}(0)/E^{(i)}}{1 + 2R_s/Z} \\ \frac{H_{x0}(R_s)}{H^{(i)}} \cong \frac{H_{x0}(0)/H^{(i)}}{1 - 2(R_s/Z)H_{x0}(0)/H^{(i)}} \end{cases} \quad (3.11)$$

where $\gamma \approx 0.577$ is the Euler constant. Equation (3.10) shows $\sim 1/f$ as well as $\sim 1/w$ dependence of the field enhancement in the nanogap which agrees perfectly with the earlier experimental and numerical results [49].

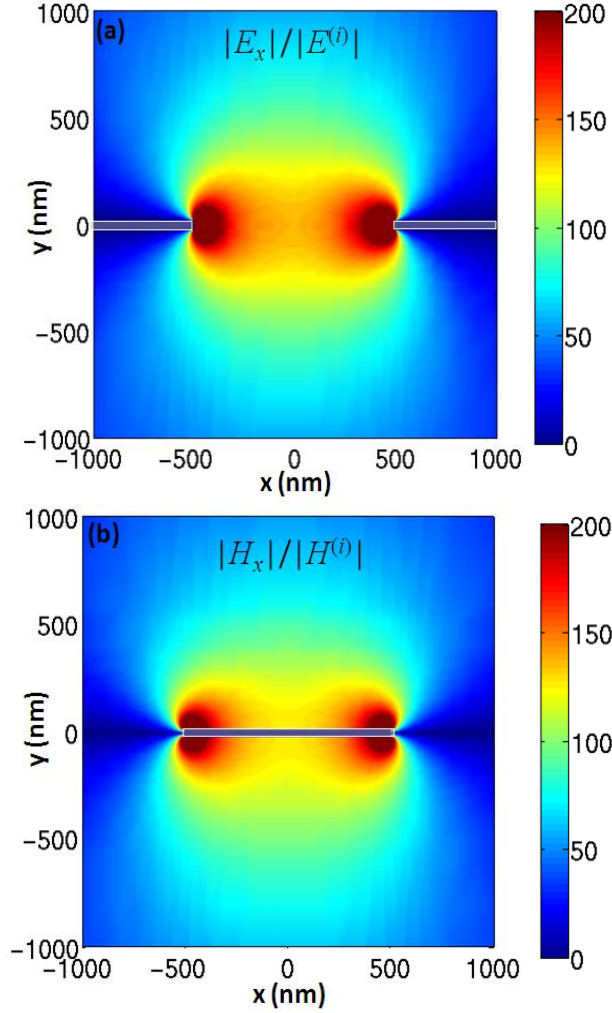


Fig. 3.3 Field enhancement obtained through FDTD analysis for $\lambda = 3\text{mm}$. To bring out similar field pattern, we used PEC and thin ($t = 40\text{nm}$) metal structure. Width (w) for both structures is $1\mu\text{m}$. (a) E_x field enhancement at gap. (b) H_x field enhancement at wire.

Equation (3.10) and (3.11) above shows that the field enhancement in the nanogap and nanowire remains the same for both the cases if the metals are PECs ($R_s = 0$). To verify this, we simulated the nanowire and nanogap structures using FDTD.

The simulation result assuming perfect conductor has been plotted in Fig. 3.3(a) and (b) for thickness that is small enough ($t = 40\text{nm}$, $w = 1\mu\text{m}$) so that the effect of finite thickness on field distribution is suppressed. To note, though the example considered here is from [49], our analysis applies equally well to other values of t and w as long as $w \ll \lambda_0$. Enhancement factor as high as $\sim 1,000$ could be achieved both for electric field ($E_{x0}(0)/E^{(i)}$) and magnetic field ($H_{x0}(0)/H^{(i)}$) with dimensions $t = 4\text{nm}$ and $w = 145\text{nm}$ (Fig.3.4(a)).

3.4. Analytical and numerical investigation of the real metallic nanogap and nanowire

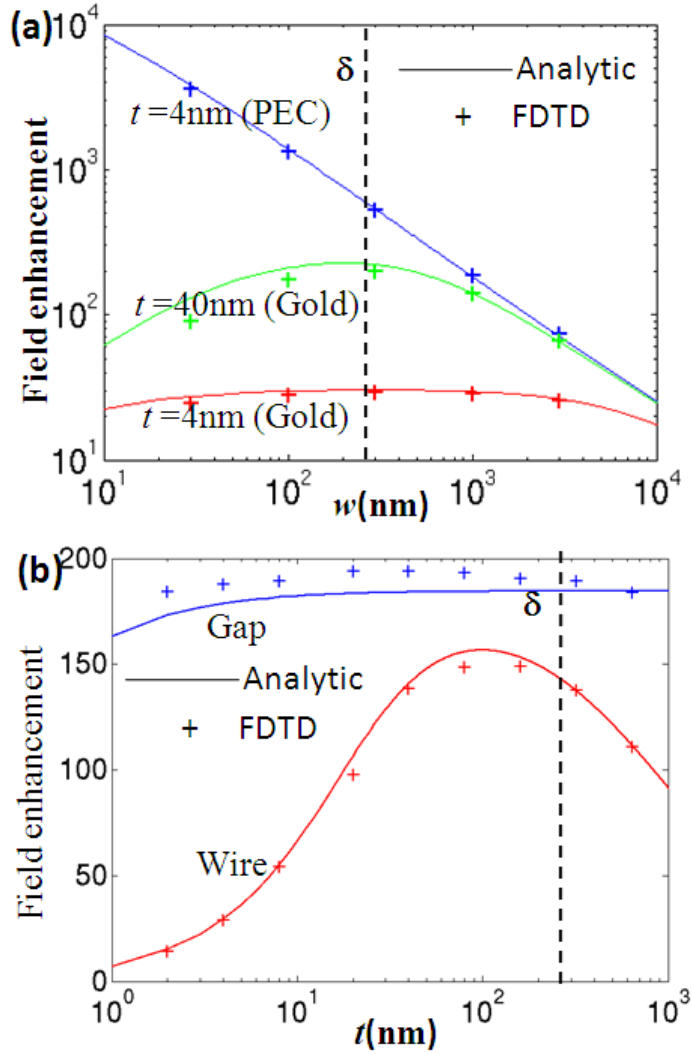


Fig. 3.4 (a) Magnetic field (H) enhancement for the nanowire plotted as a function of width: both analytical (lines) and FDTD analysis (+). (b) Field enhancement plotted as a function of t for nanowire (H) and nanogap (E, $\delta = 248\text{ nm}$, $w = 1\text{ }\mu\text{m}$)

Now for the real metal, from (3.11) the behavior of field enhancement is quite different for the nanowire from that of the nanogap. For the nanogap, the field enhancement does not reduce as R_s increases (real metal) because the resistivity of the metal R_s is much smaller compared to Z in general. However, for the nanowire, the product R_s/Z in the denominator gets multiplied by $H_{x0}(0)/H^{(i)}$ causing reduction in magnetic field enhancement as R_s increases.

Eq. (3.11) is not complete in the sense that the effects of finite thickness have been ignored. As the thickness increases, the conditions given in (3.4) and (3.5) are no longer valid. We name this as the geometric effect. This geometric effect can be accounted for in the analysis by assuming the current distribution to be essentially uniform within the wire, as long as t is smaller than the skin-depth δ .

This small t assumption also means that we are in the negligible retardation regime and the induced current in the nanowire only depends on R_s and not on t by itself. Under this condition, for the same amount of flux impinging on wires of identical widths w , the current I will be constant given by $I = H_{x0}(R_s, t) \times (2w + 2t) = H_{x0}(R_s, 0) \times (2w)$. Now the expression for nanowire that takes into account the effect of finite thickness can be arrived at by multiplying Eq.(3.11) with $w/(w + t)$.

$$\frac{H_{x0}(R_s, t)}{H^{(i)}} = \frac{[H_{x0}(0,0)/H^{(i)}]w}{[1 - 2(R_s/Z)H_{x0}(0,0)/H^{(i)}](w + t)} \quad (3.12)$$

Arriving at the final equation for field enhancement including

the geometric effect, we now study the field enhancement dependence on skin depth. Expressing field enhancement in terms of the skin depth (for the case of the nanowire) by writing $R_s = \rho/t$ [56] as $\delta^2 \omega \mu_0 / 2t$ (holds for low frequency, when $t < \delta$) in Eq. (3.12) where ρ is the resistivity, we get

$$\begin{aligned} \frac{H_{x0}(R_s, t)}{H^{(i)}} &= \frac{H_{x0}(0,0)/H^{(i)}}{1 + (\delta^2 / wt)} \frac{\pi}{(\pi/2 + i(\ln(k_0 w/4) - \gamma - 1))} \frac{w}{w+t} \\ &= \frac{H_{x0}(0,0)/H^{(i)}}{1 + (\delta^2 / wt)b} \frac{w}{w+t}, \quad b = \frac{\pi}{(\pi/2 + i(\ln(k_0 w/4) - \gamma - 1))} \end{aligned} \quad (3.13)$$

The term b above being of the order of 1, the magnetic field enhancement reduces when the product of (w/δ) and (t/δ) becomes smaller than 1. Fig. 3.4 shows the magnetic field enhancement for different wire width and thickness. Perfect agreement is observed between calculated and numerically obtained results. For the electric field of nanogap, dependence on slit thickness was found to be negligible (Eq. (3.11) and FDTD data in Fig. 3.4(b)).

While the electric field enhancement of nanogap scales linearly with the reduction of gap width (even in the sub skin depth regime [49]), Eq. (3.13) and FDTD result in Fig. 3 above shows that the case is different for nanowire if w/δ or t/δ (dotted black lines in Fig. 3.4) is smaller than 1. Thus, contrary to the case of nanogap, increase in the magnetic field enhancement of nanowire does not well correlate with the wire width but saturates in the sub skin depth regime; leading to a fundamental scaling length especially for magnetic field – the metal skin depth.

3.5. Effect of substrate

In a sense that it is impossible to experimentally realize the freestanding nanogap and nanowire, we consider the structure on the dielectric substrate which is possible for the current fabrication technologies. Since conventional substrate have larger permittivity (ϵ , order of 10) than the permeability (μ , order of 1) it is possible to expect the separate response on the electric and magnetic field. In this section, we simulate and study the effect of the dielectric substrate under the complementary metallic nanogap and nanowire structure.

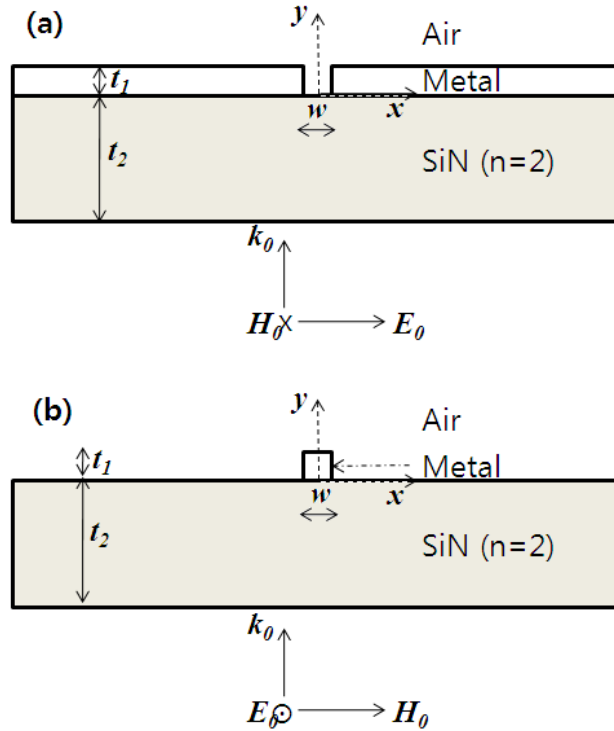


Fig. 3.5 The schematics of nanogap and nanowire on the dielectric substrate.

Using the FDTD numerical analysis, although the Babinet's principle predicts identical field pattern between complementary nanogap and nanowire, the magnetic field enhancement was larger than the electric field enhancement with the presence of the substrate as shown in Fig. 3.6.

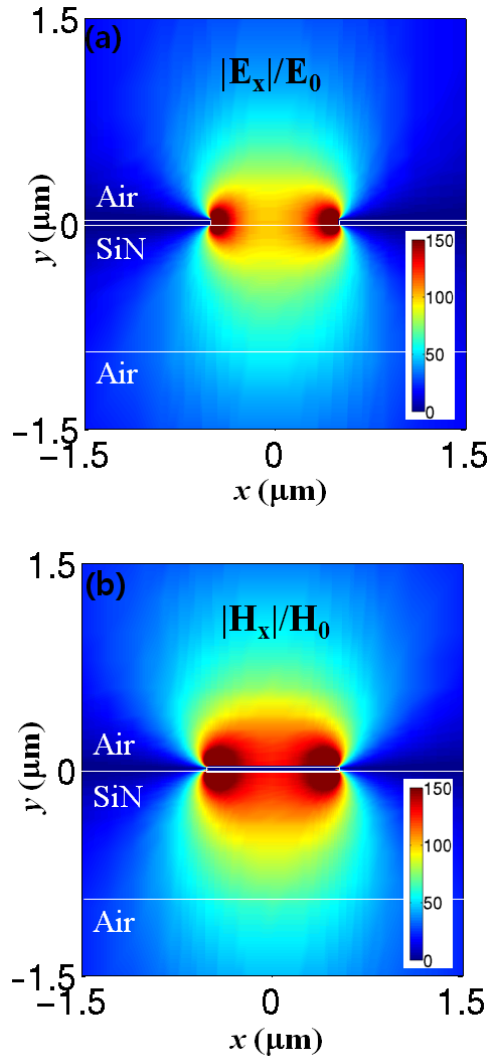


Fig. 3.6 Field pattern for the nanogap and nanowire when the substrate exists. Profile of (a) Electric field (nanogap) and (b) Magnetic field (nanowire) ($w = 1\mu\text{m}$, $t_1 = 40\text{nm}$, $t_2 = 1\mu\text{m}$).

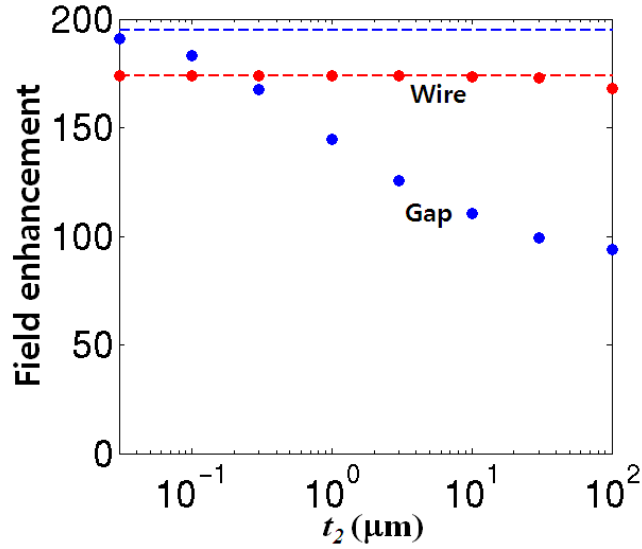


Fig. 3.7 Electric and magnetic field enhancement for different substrate thickness. (dashed line: field enhancement when $t_2 = 0$, red circle: nanowire, blue circle: nanogap)

Fig. 3.7 shows the change of the field enhancement at different substrate thickness. First of all, the magnetic field enhancement of the nanowire (red circle) does not change as the thickness increases. The negligible effect (except the slight reduction because of the Fabry–Perot resonance near $t_2 = 100\mu\text{m}$) on the nanowire means that the structure separately enhances only the magnetic field but not the electric field. Thus for the nanowire, the magnetic field enhancement will be affected by the permeability of the dielectric substrate, which is usually same value (μ_0) as air.

In contrast, the electric field in the nanogap (blue circle) decreases as the substrate gets thicker, because of the change of the effective capacitance in the nanogap. Assuming the quasi static approximation near the nanogap, as the capacitance of the

nanogap is proportional to the permittivity across the metallic surface, the existence dielectric substrate under the gap increases the capacitance of the overall structure; the voltage and the electric field enhancement across the nanogap decreases from inverse proportional relation, between voltage and capacitance ($Q = CV$).

We explain using the capacitance model for the case when the substrate thickness gets infinite (for this case, $t_2 = 100\mu\text{m}$), reducing the field enhancement value about by 45%. Neglecting the central gap region, as the thickness of the nanogap ($t_1 = 40\text{nm}$) much much smaller than the width ($w = 1\mu\text{m}$), the overall capacitance can be approximated by averaging the effect of the substrate ($\epsilon_{\text{sub}} = 4$, 50%) and air ($\epsilon_{\text{air}} = 1$, 50%) equally. For this case, the capacitance gets $C = 0.5(\epsilon_{\text{sub}}C_0 + C_0) = 2.5C_0$ where C_0 is the capacitance of the freestanding nanogap. As the capacitance increased by 2.5, the decreased electric field can be estimated by 40%, which is close value to the simulation case (45%).

3.6. Discussion of role of surface impedance in the Babinet's principle for sub-skin-depth regime

To put it intuitively, the outcome of the above analysis is that for the case of nanowire having finite conductivity, due to its boundary condition the magnetic field penetrates into the metallic region (Fig. 4(b)). This means that the current flow is distributed within the metallic nanowire and hence, the resistance of the sub skin-depth nanowire scales inversely with area [57] causing a saturation in the magnetic field enhancement. On the other hand for the case of nanogap, the field driven electric charges accumulate within the scale of the sub-nm Thomas-Fermi length at the gap surface (Fig. 3.8(a)), irrespective of the conductivity. Due to this charge accumulation on the 'surface', the effective width of the gap becomes independent of material conductivity as long as the gap-width is considerably larger than sub-nm Thomas-Fermi length scales. Hence, in contrast to the nanowire, there is no conductivity dependent variation in the achieved electric field enhancement.

To add, Fig. 3.8 shows the spatial distribution of the field enhancement at the exit ($y = 100\text{nm}$) obtained from FDTD analysis for the nanogap and nanowire with same dimensions and material parameters as in Fig. 3.4.

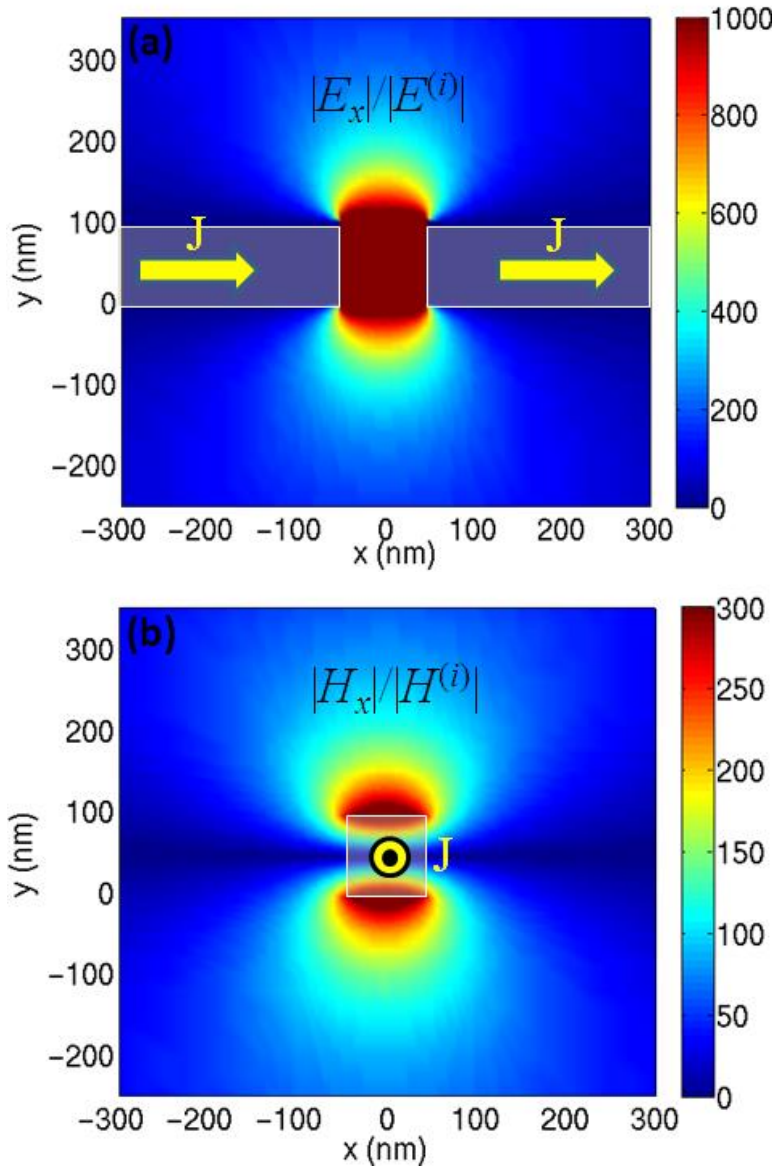


Fig. 3.8 Zoomed-in image of field enhancement obtained through FDTD analysis (Gold, $t = 100\text{nm}$, $w = 100\text{nm}$). The arrows represent the current flow (J) in the metal for (a) nanogap and (b) nanowire.

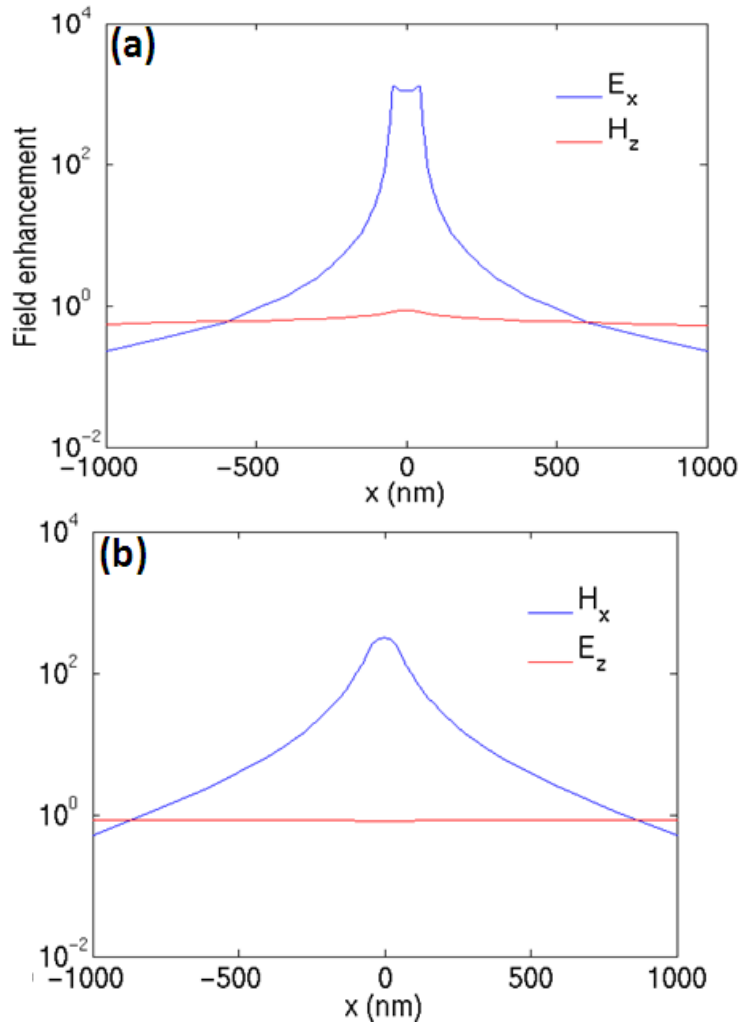


Fig. 3.9 Spatial distribution of the field enhancements at the exit side ($y = 100$ nm) obtained from FDTD for the same structures and material parameters as in Fig. 3.8. (a) nanogap and (b) nanowire.

The effect of the surface impedance has an opposite tendency to the substrate that the saturation effect occurs to the nanogap case. So about the same value of the field enhancement could be achieved when the effect of substrate is added. For example, meanwhile the free standing gold nanogap and nanowire for $w =$

$1\mu\text{m}$, $t_1 = 40\text{nm}$ gives field enhancement values of 190 and 140, the field enhancement of both structure gets 140 when the substrate thickness is $1\mu\text{m}$. When the structure size gets order of sub-skin-depth, the effect of the substrate is relatively smaller than the metallic loss. For the case of the nanogap and nanowire of $w = 100\text{nm}$, $t_1 = 100\text{nm}$, the field enhancement values are 1400, 300 for no substrate ($t_2 = 0$), and 900, 300 when $t_2 = 1\mu\text{m}$, respectively.

3.7. Summary

To summarize, metallic nanowire structures (Babinet complementary structures for nanogaps) have been proposed and analyzed to achieve extraordinary magnetic field enhancement. Enhancement of the THz magnetic field by a factor of 300 (in terms of intensity, corresponds to a factor of 90,000) is obtained from the proposed nanowire. Analytic formulas derived incorporating thickness-normalized surface impedance concept shows that the achievable magnetic field enhancement in sub skin-depth nanowires, though huge, cannot be as much as the electric field enhancement achieved in nanogaps. Orders of difference in the field enhancement were observed between nanogap and nanowire. More specifically, it was observed that when the cross sectional area of the nanowire becomes smaller than the square of skin depth of the material, there was a saturation in the achieved magnetic field enhancement. Our study provides detailed insights into the underlying physical phenomena that cause the deviations in classical Babinet's principle. We also believe that our rigorous theory will work as valuable guidelines for designing efficient sub skin-depth metallic components such as the nanowire and nanoresonator, suitable for future applications in magnetic sensors and magnetic nonlinearity based devices.

3.8. Application to the switch

Here, we present ultra-broad-band metamaterial thin film with colossal dynamic control range, based on the nanogap antenna structure. To better illustrate the active nano metamaterial performance with full extinction control, we qualitatively investigated transmissions around the single nano resonator-patterned thin film at insulating and conducting states of VO_2 , respectively. For these purposes, we calculated horizontal electric field intensity (Fig. 3.10, (a) and (b)) and conducting current distributions (Fig. 3.10, (c) and (d)) using a 3D finite-difference time-domain (FDTD) method with asymptotically varying grid sizes. The nano resonator used in this calculation has 100 nm width, 100 nm-thickness, and 10 μm -length. The refractive index of VO_2 is 3 for insulating state and $10.24+10.10i$ for conducting state, respectively. The electric field intensity is normalized to the calculated value for an equivalent structure without nano pattern, and the conducting current is normalized by maximum value of each figure. When the film is insulating, the narrow nano resonator in the middle has large antenna cross section, attracting surrounding electromagnetic waves and funneling them through itself (Fig. 3.10(a)). The enhanced transmission at the nano resonator is around 100 with comparable condition identified by a 100-nm-width and 10- μm -length of the nano resonator at the resonance wavelength 34.48 μm . However, when the underlying film becomes metallic, the enhanced conducting current flowing beneath the resonator effectively shuts off the

resonator, reflecting most of light back and achieving orders of magnitudes larger extinction (Fig. 3.10(b),(d)). The conducting current distributions in Fig 3.10(c) and (d) represent the on- and the off-state of the metamaterial, which agree well with the experimental results.

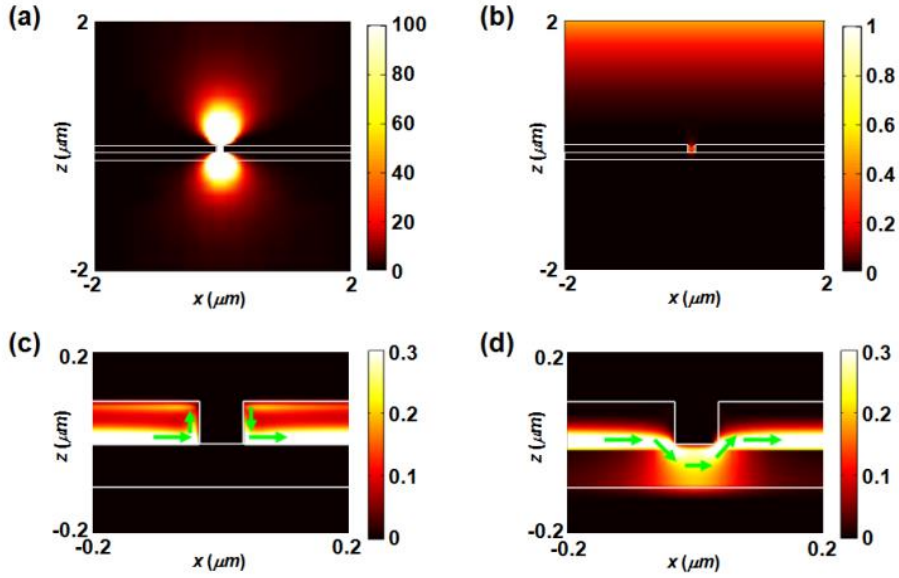


Fig. 3.10 (a,b) Electric field and (c,d) current pattern of the nano-antennas for on and off state.

3.9. Application to the magnetic polarizer

3.9.1. Bethe' s single hole determines magnetic field orientation

Here we show that a metallic circular nanoscale aperture is a magnetic scatterer in complete agreement with Bethe' s theoretical analysis on diffraction by a circular aperture, allowing the magnetic field direction to be determined, independent of the electric field direction. This structure is, therefore, a device that functions as a polarization analyser for the magnetic field component of light.

Time varying magnetic fields induce Eddy currents in metals, which is the principle behind induction heating and welding, as well as metal detection. When light is incident on a subwavelength aperture in a metallic film with a large dielectric constant, the small size of the aperture and the large dielectric constant of the metal result in strong evanescent fields in this quasistatic regime. The tangential magnetic field enters the subwavelength hole with a certain distortion (Fig. 3.11(a)), with its amplitude at the centre of the aperture equal to that of the incident field. In contrast, the tangential electric field is primarily reflected, its influence being much weaker on both sides of the plane and inside the hole (Fig. 3.11(b)). Therefore, the scattering properties of an aperture in a metal film are mainly determined by the incident magnetic field—inducing surface currents, which in turn function as a source for far-field radiation [58,59]. It should be noted that the magnetic field—dominated scattering process is generally possible with

non-circular apertures, but for the present study, a circular hole has been chosen for clarity [60].

The best way to separate the effects of electric and magnetic fields on this metallic aperture is to probe the structure with light at oblique incidence angles, having an asymmetric polarization that is neither purely transverse electric (TE, $\phi=0^\circ$) nor transverse magnetic (TM, $\phi=90^\circ$), where ϕ is the polarization angle (Fig. 3.11(c)). We consider a detector placed along the z axis and hence insensitive to the normal field components. In this case, the incident electric and magnetic fields projected onto the reflecting plane, $\mathbf{E}_t = \mathbf{E}_0 - (\mathbf{z} \cdot \mathbf{E}_0)\mathbf{z} = E_0(-\cos\theta\sin\phi, \cos\phi, 0)$ and $\mathbf{H}_t = H_0(-\cos\theta\cos\phi, -\sin\phi, 0)$ are, in general, not orthogonal, which creates an ideal situation to discriminate the electric and magnetic nature of the scattering.

In Fig. 3.11(d),(e), finite-difference-time-domain (FDTD) calculations of surface currents on the scattering side of the structure, for the case of an oblique incident angle ($\theta=80^\circ$) with $\phi=21^\circ$ and 159° , respectively, are shown, with \mathbf{E}_t and \mathbf{H}_t depicted by blue and red arrows, respectively. For both the cases, the surface current \mathbf{K} profile is aligned perpendicular to the tangential magnetic field, with the incident electric field direction seemingly irrelevant. Continuously changing the electric field direction while maintaining a constant magnetic field direction can be achieved by varying the wavevector of the incident light with almost no effect on the surface current distribution. These observations strongly suggest that the surface currents on the scattering side of the structure are of an induced nature, with its symmetric axis determined by the

incident magnetic field $\mathbf{n} \times \mathbf{H}_i$, where \mathbf{n} is the unit vector normal to the plane, in our case \mathbf{z} .

With the surface current profile on the scattering side determined primarily by the incident magnetic field, the far-field radiation polarization also reflects the magnetic field direction, at least for the above example of a nearly perfect conductor. As its far-field polarization is invariant with respect to changes in the incident electric field direction because of the negligible tangential electric field on the metal surface, the subwavelength aperture, when combined with far-field polarization analysis, senses the orientation of magnetic vector field. The incident magnetic field direction can be obtained simply by rotating the polarization of the scattered light by 90° . The critical question is whether the surface current profile and radiation polarization of the aperture would still be determined primarily by the incident optical frequency magnetic field in which the metal has less-than-ideal metal conductivities, and when the aperture is larger than the pure quasistatic regime analysed here.

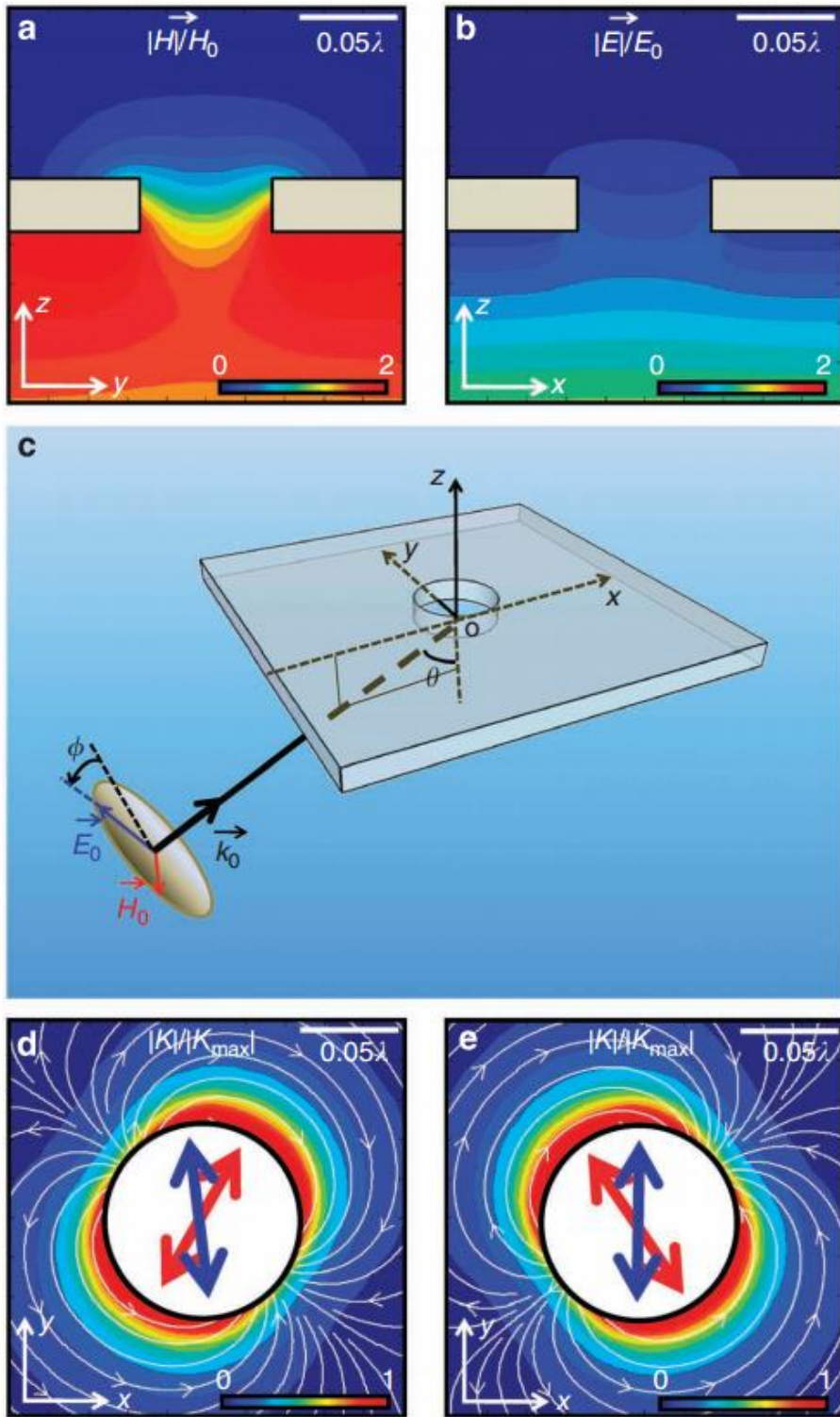


Fig. 3.11 Calculated field and current distributions around a

subwavelength hole. The metal film has been assumed to be a near perfect electric conductor with a hole diameter of 0.08λ and a thickness of 0.02λ . (a,b) Normalized electric and magnetic field strength distribution with the normal incidence ($\mathbf{E}_0 = E_0\mathbf{x}$, $\mathbf{H}_0 = H_0\mathbf{y}$). (c) Schematic of setup with an oblique incidence ($\theta \neq 0^\circ$) \mathbf{k}_0 in the xz plane, with the polarization angle ϕ . (d,e) Surface current distribution on the exit side of the hole for $\phi=21^\circ$ and 159° with fixed θ of 80° . \mathbf{H}_t and \mathbf{E}_t are depicted as red and blue arrows inside the hole, respectively. The white arrows represent the direction of the surface current.

3.9.2. Functionality of the polarization analyzer for magnetic field depending on hole diameters and excitation wavelengths

In this section, we investigate the effect of the hole diameters and the excitation wavelengths on the functionality of the hole as a nano magnetic polarizer. We expect that as the hole becomes larger, its scattering no longer reflects the orientation of the surface current in its absence, losing its functionality. Similarly, as the wavelength becomes smaller, the metal becomes poorer, again losing its functionality.

First, we plot the scattering polarization for various hole diameters for the 780 nm wavelength laser excitation. Apertures are made on a piece of 80 nm-thick gold film deposited onto a sapphire substrate and the incident polarization angle is fixed at $\phi=45^\circ$. As shown both

experimentally (red circle) and by FDTD calculation (blue rectangle) data in Fig. 3.12(a), for the small hole, the scattering polarization angle $\psi_{sc,E}$ (52 degrees) is the same as the angle of the perfect magnetic polarizer, oriented at 90 degrees from the tangential magnetic field. On the other hand, as the diameter of the hole gets larger, $\psi_{sc,E}$ deviates from the magnetic polarizer line.

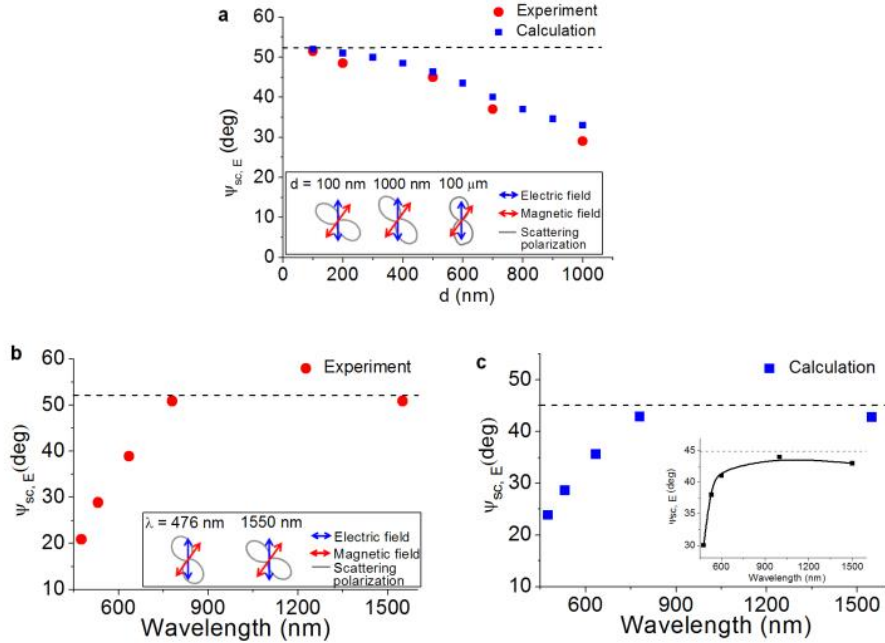


Fig. 3.12 (a) Scattering field polarizations for various hole diameters ($\theta = 70^\circ$, $\lambda = 780$ nm). FDTD calculation (blue rectangle) and experimental (red circle) $\psi_{sc,E}$ for various hole diameters when ψ is fixed at 142° . The black dotted line, $\psi_{sc,E} = 52^\circ$, denotes the perfect magnetic polarizer case. The Inset shows the polarization analyzed scattering intensities together with \mathbf{H}_t and \mathbf{E}_t for $d=100$ nm, 1000 nm, and 100 μm . (b) $\psi_{sc,E}$ vs. wavelength for a 100 nm hole punctured on 80 nm-thick gold on a sapphire substrate ($\theta = 70^\circ$, $\phi=45^\circ$; $\psi = 142^\circ$). The Inset

compares the scattering polarization polar plots for 476 nm and 1550 nm wavelengths. (c) FDTD calculation (blue rectangle) of $\psi_{sc, E}$ when ψ is fixed at 135° using realistic gold and sapphire dielectric constants. (Inset) FDTD calculation (black rectangle) of $\psi_{sc, E}$ when the size of hole is scaled with the wavelength keeping $d/\lambda = 0.1$.

The Inset shows the experimental scattering polarization for $d = 100$ nm, where the scattering polarization is perpendicular to the tangential magnetic field, and for $d = 1000$ nm, and finally for $d=100$ μm where the scattering polarization is along the tangential electric field. Experimental and theoretical data are in good agreements, especially considering that the simulation was for the free standing PEC case. These results show that while a smaller hole is always preferable, a diameter $d \sim \lambda/2$ can be used as an acceptable magnetic polarizer with errors smaller than five degrees.

Second, we plot the scattering polarization for various wavelengths to see the functionality for the pooler metal case. The hole diameter is 100 nm also made on a 80 nm–thick gold film deposited onto a sapphire substrate. Fig. 3.12(b) and (c) shows experimental and calculation data of scattering polarization angle $\psi_{sc, E}$ for various wavelengths, respectively. The substantial deviation at shorter wavelengths indicates that apertures on gold cannot be used as magnetic polarizers for visible wavelengths.

Fig. 3.12(c) shows FDTD simulation, in good agreement with experiments. It should be noted that in both Fig. 3.12(b) and

3.12(c), the diameter is fixed at 80 nm while the wavelength changes, making the relative hole size larger for shorter wavelengths. To determine whether the increasing error in the visible wavelengths is due to decreasing of ϵ or due to the increasing of relative hole size, in the inset of Supplementary Fig. 3.12(c) we show the result when both the hole size and the wavelength are scaled so that the ratio of the hole diameter to wavelength is constant: $d/\lambda=0.1$ (Inset of Fig. 3.12(c)). The similarity between the result for the fixed hole diameter and the scaled hole diameter suggests that the error originating from the decreasing of $|\epsilon|$ is chiefly responsible for the increasing error at visible wavelengths. It is expected that with decreasing of $|\epsilon|$, higher order terms contribute, making simple Leontovich boundary condition no longer valid.

Chapter 4.

Decoupling of ϵ and μ with an anisotropic photonic meta-atom toward top-down design of metamaterials: Application to zero index super- λ funneling through a sub- λ nanoslit

4.1. Introduction

We propose to introduce anisotropy ($\epsilon_r \neq \epsilon_\theta$) into a metamaterial building block as a means for decoupling of the effective permittivity ϵ_{eff} and permeability μ_{eff} . Inverse-solving the decoupled solution for a target set of ϵ_{eff} and μ_{eff} , an analytic, top-down determination for the internal structure of a photonic meta-atom is accomplished. To realize the anisotropy from

isotropic materials, a particle of internal permittivity modulation is proposed. Constructing a matched zero index dielectric meta-atom of nano-pizza geometry, super-funneling of a 50λ -wide wave through a sub- λ slit is demonstrated; far exceeding the flux collection limit dictated by the λ -zone.

Metamaterials exhibiting naturally non-occurring refractive indices [1–29] and their application to exotic forms of wave manipulation [30–33] is one of the hottest research topics in nano-photonics today. Since the properties of photonic metamaterials manifest themselves through electromagnetic coupling to the far-field, design strategies have been sought for the realization of designer electric (ϵ_{eff}) and magnetic (μ_{eff}) dipolar responses through the engineering and assembly of metallic or dielectric building blocks.

Yet, past approaches to metamaterial (MM) design are based on retro-fit, bottom-up approaches – where the building blocks are initially proposed and the subsequent design is carried out through a series of iterations and guesswork, with the hope that the exotic index is realized. Moreover, as there is no physical mechanism to attain fine-control over the movement of bound charges in dielectrics, the intuitive design of MM has been largely based on metallic inclusions providing well-defined current paths of free charges. Although realistically, the intrinsic loss problem of metals make dielectric MM [1–5] a favorable option, yet have gained insufficient attention due to the current proliferation of metallic MM.

In this chapter, we propose a new paradigm in MM design: a top-down approach – where the target ϵ_{eff} and μ_{eff} are first

specified, and the design parameters are subsequently determined, all the while using readily available lossless dielectrics. Our new approach is motivated by a direct analogy with the electric- and magnetic dipolar nature of a classical atom. It is well understood that the origins of the permittivity ϵ and permeability μ of an atom are directly linked to the mutually orthogonal movements of the electron and the related dipole moments p_r (χ_r) and m_z (χ_θ) (Fig. 4.1).

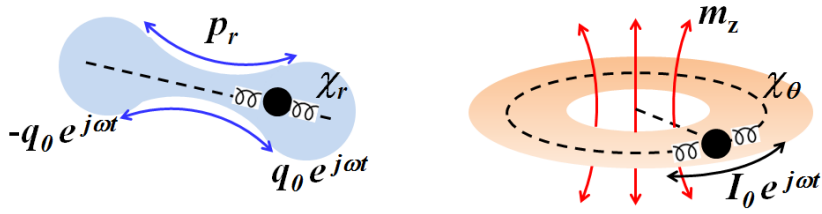


Fig. 4.1 Physical origin of the electron induced electric (left) and magnetic (right) dipole moments of a classical atom.

From this point of view, it is evident that we could decouple and independently control ϵ_{eff} and μ_{eff} of a photonic meta-atom (e.g., an elementary dielectric resonator) by introducing internal anisotropy $\epsilon_r \neq \epsilon_\theta$ conforming to current pathways of chosen electric / magnetic resonances. Further, by retaining a simple geometry of an elementary resonator we expect that the optical response can be predicted analytically. This would offer decoupled relations between those $(\epsilon_r, \epsilon_\theta)$ that realize the desired exotic index $(\epsilon_{\text{eff}}, \mu_{\text{eff}})$; a truly top-down approach to the MM design.

4.2. Analytical investigation of the hypothetical anisotropic meta-atom

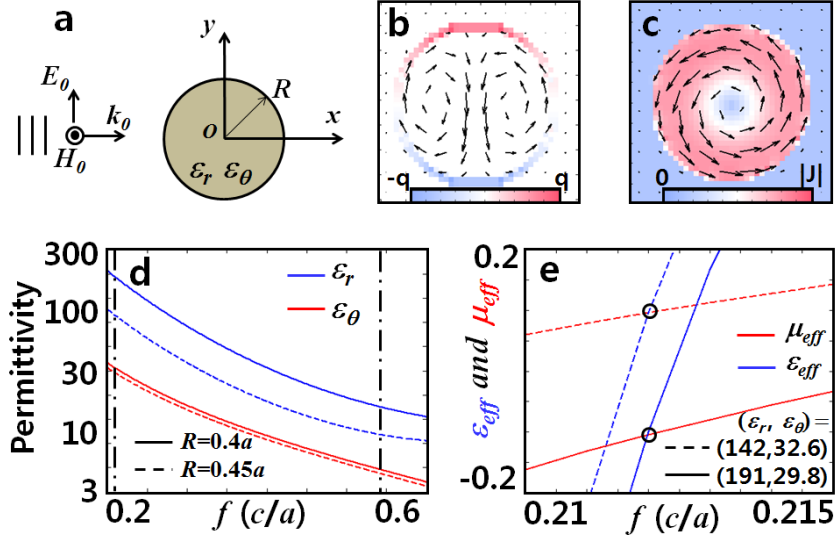


Fig. 4.2 (a) Schematic of the anisotropic meta-atom illuminated by TE plane wave. (b) Charge and (c) current distribution at the electric and magnetic resonance frequencies, respectively (arrows denote current flow). (d) Calculated ϵ_r and ϵ_θ values that give matched zero index property (solid: $R = 0.4a$, dashed: $R = 0.45a$). (e) ϵ_{eff} and μ_{eff} tunability including demonstration of matched index property ($n_{\text{eff}} = \pm 0.1$).

Without loss of generality, we consider the two dimensional case shown in Fig. 4.2(a); a transverse electric (TE) plane wave is incident onto a cylindrical particle of radius R with split ϵ_r , ϵ_θ anisotropy. To derive ϵ_{eff} and μ_{eff} of the meta-atom lattice, we start from the zeroth order expressions for the electric and

magnetic polarizabilities (α_e and α_m) [6] of the isolated particle,

$$\alpha_e = \frac{\int_C (\varepsilon_y - 1) E_y ds}{E_0}, \alpha_m = -\frac{j\omega}{2H_0} \int_C \varepsilon_0 (\varepsilon_\theta - 1) \mathbf{r} \times \mathbf{E} ds \quad (4.1)$$

where ε_i is the permittivity of the particle along the i direction, and the integration is over the particle cross section C . To treat the anisotropic case, we introduce the auxiliary vector potential F as $\mathbf{D} = -\nabla \times \mathbf{F}$ [61], where \mathbf{D} is the electric displacement vector. The TE mode scalar wave equation for F_z [61] can then be written as,

$$r \frac{\partial}{\partial r} \left(r \frac{\partial F_z}{\partial r} \right) + \frac{\varepsilon_r}{\varepsilon_\theta} \frac{\partial^2 F_z}{\partial \theta^2} + \omega^2 \mu_0 \varepsilon_0 \varepsilon_\theta r^2 F_z = 0. \quad (4.2)$$

Solving Eq. (4.2) by separation of variables, the solution for F_z can be expressed in terms of the Bessel–Fourier series expansions,

$$F_z = \begin{cases} H_0 \sum_{n=0}^{\infty} b_n J_{\sqrt{\frac{\varepsilon_\theta}{\varepsilon_r}} n} (\sqrt{\varepsilon_\theta} k_0 r) \cos(n\theta) & (r < R) \\ H_0 \sum_{n=0}^{\infty} a_n H_n^{(2)}(k_0 r) \cos(n\theta) + F_{z0} & (r > R) \end{cases}, \quad (4.3)$$

where δ_{ij} is Kronecker delta, H_0 is the incident magnetic field amplitude, $k_\theta = (\varepsilon_\theta)^{1/2} k_0$, J_n and $H_n^{(2)}$ are the Bessel and Hankel (second kind) functions. From $\mathbf{D} = -\nabla \times \mathbf{F}$, the polarizabilities in (4.1) can evidently be expressed in terms of a series expansion of b_n . Writing down only the lowest order terms (applicable within the assumption $\varepsilon_r, \varepsilon_\theta \gg 1$) and by setting $\phi_k = k_0 R$ we arrive at,

$$\alpha_e \sim \pi R c J_{\sqrt{\varepsilon_\theta}}(\sqrt{\varepsilon_\theta} \phi_k) b_1, \alpha_m \sim j \omega \pi R^2 J_2(\sqrt{\varepsilon_\theta} \phi_k) b_0. \quad (4.4)$$

The coefficients b_n are determined by applying the boundary conditions for tangential E and H at $r = R$:

$$b_n = \frac{2(2 - \delta_{n0})(-j)^n / \pi \omega \phi_k}{J_{\sqrt{\varepsilon_\theta}}(\sqrt{\varepsilon_\theta} \phi_k) H_n^{(2)}(\phi_k) - \frac{1}{\sqrt{\varepsilon_\theta}} J'_{\sqrt{\varepsilon_\theta}}(\sqrt{\varepsilon_\theta} \phi_k) H_n^{(2)}(\phi_k)}. \quad (4.5)$$

From α_e and α_m of the isolated particle (4.4) and (4.5), we now calculate ε_{eff} and μ_{eff} for a periodic square lattice of meta-atoms. Using the mixing formula [10],

$$\begin{aligned} \varepsilon_{\text{eff}} &= f(\alpha_e, C_{\parallel}), \mu_{\text{eff}} = f(\alpha_m, C_{zz}) \\ f(\alpha, C) &\approx 1 + \frac{1}{a^2} \frac{1}{\text{Re}[\alpha^{-1}] - \text{Re}[C]}, \end{aligned} \quad (4.6)$$

where $C_{\parallel} \approx \frac{k_0^2}{2} \sum_{\mathbf{r}_1 \neq 0} H_0^{(2)}(k_0 |\mathbf{r}_1|) + \frac{1}{a^2}$, $C_{zz} \approx 2C_{\parallel} - \frac{1}{a^2}$ are the

dynamic interaction constants, a is the periodicity, and \mathbf{r}_1 is a lattice point vector [10]. We note though, while Eq. (4.6) is valid only in the low index regime ($n_{\text{eff}} \ll \lambda/2a$ [10]), ε_{eff} and μ_{eff} can be determined from S-matrix parameters [62] for the high index case. Focusing on the low index case, we solve the problem inversely from (4.6) to determine $(\varepsilon_{\text{eff}}, \mu_{\text{eff}})$. Using the identity for changing order of Bessel functions, grouping all terms in ε_r and ε_θ on the left hand side of (4.6), and then setting $\varepsilon_{\text{eff}}(\mu_{\text{eff}}) = 0$ for the matched zero index case we get,

$$\begin{aligned} [J_{\sqrt{\varepsilon_\theta}}'(\sqrt{\varepsilon_\theta} \phi_k)] / [J_{\sqrt{\varepsilon_\theta}}(\sqrt{\varepsilon_\theta} \phi_k)] &= A(\phi_k)^{-1} \quad (\varepsilon_{\text{eff}} = 0), \\ [\sqrt{\varepsilon_\theta} J_1'(\sqrt{\varepsilon_\theta} \phi_k)] / [J_1(\sqrt{\varepsilon_\theta} \phi_k)] &= B(\phi_k)^{-1} \quad (\mu_{\text{eff}} = 0), \end{aligned} \quad (4.7)$$

where $A(\phi_k)$ and $B(\phi_k)$ are slowly varying functions of ϕ_k obtained from (4.6). Taking the solution for ϕ_k to first order near the first zeros of the Bessel functions [6], Eq. (4.7) can be put in the simpler form,

$$\begin{aligned}\phi_k &\sim \frac{\alpha_0 - A(\phi_k)}{\sqrt{\epsilon_\theta}} + \frac{\alpha_1 - \alpha_0}{\sqrt{\epsilon_r}} \quad (\epsilon_{\text{eff}} \sim 0), \\ \phi_k &\sim \frac{\alpha_1}{\sqrt{\epsilon_\theta}} - B(\phi_k) \quad (\mu_{\text{eff}} \sim 0),\end{aligned}\tag{4.8}$$

where α_0 (~ 2.405), α_1 (~ 3.831) are the first zeros of the zeroth and first order Bessel functions. Inspection of Eqs. (4.7) and (4.8) demonstrates the complete decoupling of μ_{eff} from ϵ_r , thus providing separate tunability of ϵ_{eff} and μ_{eff} by adjustment of ϵ_r and ϵ_θ ; confirming our expectations according to the respective current patterns exhibited by the electric and magnetic modes [Fig. 4.2(b), (c)]. Fig. 4.2(d) shows the solution of (4.7) for the particles of $R = 0.4a$ (solid lines) and $0.45a$ (dashed lines), giving the values of $(\epsilon_r, \epsilon_\theta)$ that provide a matched zero index at different target frequencies. The required $(\epsilon_r, \epsilon_\theta)$ varied between about 100 to 10, and become smaller as either f or R are increased. We also show in Fig. 4.2(e) the tunability of ϵ_{eff} and μ_{eff} including demonstration of exotic matched index properties ($n_{\text{eff}} = \pm 0.1$). In all cases, the required ϵ_r is greater than ϵ_θ , thus red-shifting the usually higher energy electric dipole resonance $(\epsilon_r, \epsilon_\theta)$ closer toward the lower energy magnetic dipole resonance (ϵ_θ) .

4.3. Dielectric implementation of the designed hypothetical anisotropic meta-atom

To realize the set of separate ϵ_r and ϵ_θ from isotropic materials, we modulate the internal permittivity in the particle along a given axis (r or θ). A proposed structure of nano-pizza geometry is shown in Fig. 3(a). Extending the concept of average permittivity [63] from Gauss' law in polar coordinates we obtain,

$$\epsilon_r \sim (1-p)\epsilon_1 + p\epsilon_2, \quad \epsilon_\theta \sim \left(\frac{1-p}{\epsilon_1} + \frac{p}{\epsilon_2}\right)^{-1}, \quad (4.9)$$

where ϵ_1, ϵ_2 ($\epsilon_1 < \epsilon_2$) are the permittivities of nano-pizza slices shown in Fig. 4.3(a) and p is the proportion of the area of slices containing ϵ_2 . While it is possible to design the meta-atom for fixed ϵ_1 ($= 1$, for example) by changing p and ϵ_2 , we now focus on the uniformly sliced nano-pizza ($p = 0.5$). For $p = 0.5$, as the arithmetic mean is larger than the harmonic mean, the condition of $\epsilon_r \geq \epsilon_\theta$ [Fig. 4.2(d)] is met in this geometry [we note, $\epsilon_\theta \geq \epsilon_r$ for nano-donut - inset of Fig. 4.3(a)]. Using (9) for the pair $(\epsilon_r, \epsilon_\theta) = (166, 31.1)$ [giving zero index at $f = 0.212$ c/a (2.12 GHz for $a = 1.5$ cm) and $R = 0.4a$ from Eq. (4.7)], we obtain $(\epsilon_1, \epsilon_2) = (16.32, 315.8)$. In Fig. 4.3(c) we compare plots of ϵ_{eff} (α_e) and μ_{eff} (α_m) analytically obtained from Eq. (4.6), with FDTD simulations of a 40-slice nano-pizza. Near the zero-index, an almost perfect fit with less than 1% frequency error was obtained from that predicted by Eq. (4.9). Additionally, in consideration of fabrication complexity, a nano-

pizza with reduced number of slices has also been tested [Fig. 3(b)].

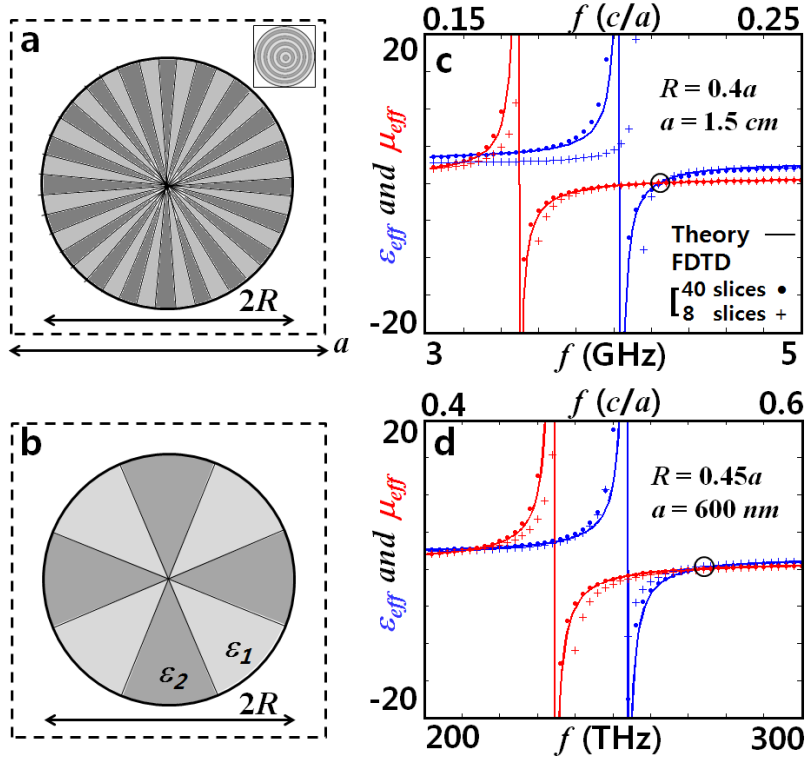


Fig. 4.3 Anisotropic meta-atoms ($\epsilon_r \neq \epsilon_0$) of nano-pizza geometry with (a) 40 slices and (b) 8 slices. (inset in (a) shows an example of nano-donut). Calculated ϵ_{eff} and μ_{eff} for nano-pizzas of radius (c) $R = 0.4a$ ($a = 1.5 \text{ cm}$), and (d) $R = 0.45a$ ($a = 600 \text{ nm}$). By appropriate choice of a , the operating frequency is determined. Circles indicate the frequencies of operation at matched zero index. Excellent agreement between the theory and FDTD (for both 40 slice and 8 slice nano-pizza), especially near the matched zero index, is observed.

We find that, even though the average (ϵ_r, ϵ_0) of (4.9) starts to deviate as the size of slices is increased, by using several Newton iterations for the zero-index frequency deviation, it was possible to determine $(\epsilon_1, \epsilon_2) = (15.12, 171.9)$ providing a matched zero index for the 8-slice nano-pizza at $f = 0.212 c/a$ [marked with ‘+’ symbol in Fig. 4.3(c)]. This value determined from the mixing formula (4.6) is in excellent agreement with exact values of $(\epsilon_1, \epsilon_2) = (14.53, 179.2)$ extracted from S-matrix parameters [62]. Smaller permittivity values [40 slices: $(\epsilon_1, \epsilon_2) = (2.43, 15.13)$, 8 slices: $(2.22, 12.96)$] using Si and SiO₂ for example, can be accessed by using a larger radius $R = 0.45a$, giving matched zero index at $f = 0.546 c/a$ ($\lambda = 1100$ nm for $a = 600$ nm) [Fig. 4.3(d)]. It should be noted, our implementation of split-symmetry susceptibility significantly widens the scope of metamaterial design; offering a top-down approach to designer optical response (including both matched zero and negative index) from lossless dielectrics, and also lifting the stringent restrictions of accidental degeneracy [4] which itself was limited to matched zero index at fixed frequency.

4.4. Metallic implementation of the designed hypothetical anisotropic meta-atom

Fig. 4.4(a) shows the square lattice unit cell structure of the proposed 2-D meta-molecule. The unit cell consists of a 3×3 array of (perfectly conducting) metallic meta-atoms [12,64]. The properties of the meta-molecule have been determined using the finite difference time domain method, with the impinging plane wave (H_z polarized) propagating in the negative y direction. As can be seen from the electric field distribution (Fig. 4.4(b), (c)), the electric and magnetic response of the meta-molecule is mainly determined by the linear (x) / angular (θ) components of displacement current in the dielectric.

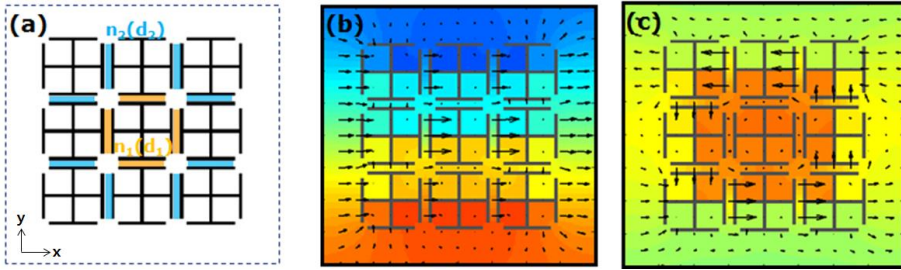


Fig. 4.4 (a) Unit cell structure of the proposed metallic meta-molecule. (b, c) H_z field pattern (color) with Electric field (E) distribution (arrows) corresponding to (b) electric and (c) magnetic modes of the meta-molecule.

From Fig. 4.4(b), (c) it is apparent that independent control of (ϵ , μ) could be achieved by separate control of n_1 and n_2 (Fig.

4.4 (a)). Fig. 4.5 shows the change of (ϵ, μ) spectra for different values of n_1 and n_2 . Even if the change of n_2 affects the response of both ϵ and μ (Fig. 4.5(a)), the change of n_1 only affects the response of ϵ , not μ (Fig. 4.5(b)); clearly demonstrating the decoupling of μ from n_1 , sufficient for the independent control of ϵ and μ (e.g. adjust n_2 for desired μ , and then adjust n_1 for desired ϵ).

For the given problem, the matched zero index response was achieved by adjusting n_1 and n_2 values to 2.9 and 1.5 respectively (Fig. 4.5(a), solid). To note, the proposed concept is not limited only for matched zero index, but to completely flexible design of (ϵ, μ) including also negative index and ultra-high index metamaterials.

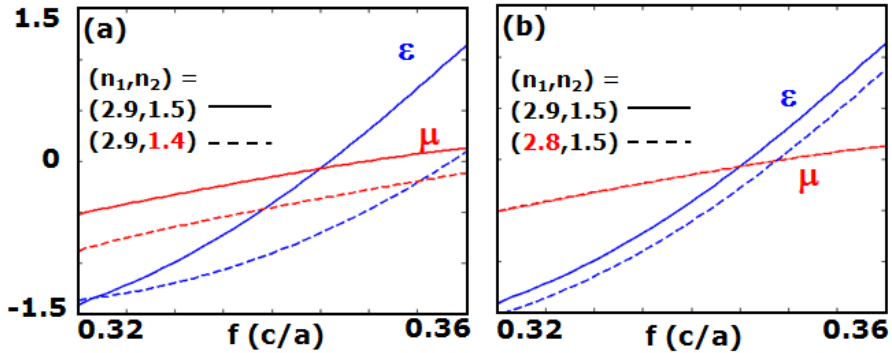


Fig. 4.5 Demonstration of the decoupling μ from n_1 and also matched zero index response for the proposed meta-molecule. The plots show the spectra of (ϵ, μ) with changing (a) n_2 and (b) n_1 .

4.5. Application to the super funneling through the nanoslit utilizing designed matched zero index meta-atom

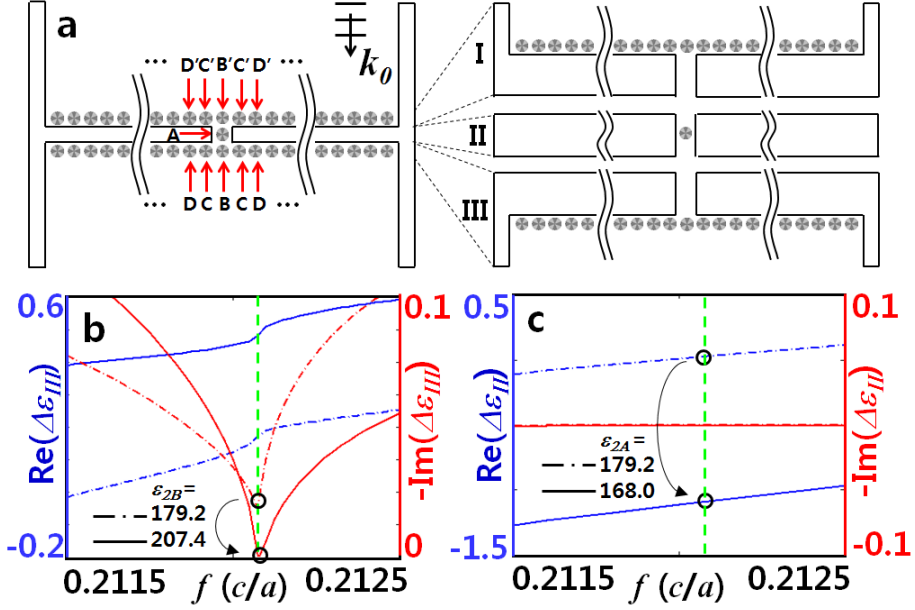


Fig. 4.6 (a) Schematic of the meta-atom coated slit structure (left) as an assembly of three parts (right). Deviation of effective permittivity $\Delta\epsilon$ before (dash-dot) and after (solid) tuning of (b) particle B in part III and (c) particle A in part II. Meta-atom of 8 slice nano-pizza (ϵ_1, ϵ_2) = (14.53, 179.2) were used. Green dash line denotes $f = 0.212$ c/a.

Using the nano-pizza of matched zero index, we now investigate the problem of extraordinary optical transmission (EOT) [34,45,49,65,66], for which the maximum field enhancement is limited by the λ -zone [34]. Applications of

zero index in EOT have been demonstrated in the past [6–9], yet the possibility of flux funneling beyond the λ -zone has not been investigated. A perfect electric conductor (PEC) sub-wavelength slit of flux reception width far larger than the λ -zone, atop and below which is placed a single layer of meta-atoms of $\epsilon_{\text{eff}} = \mu_{\text{eff}} = 0$ (at $f = 0.212$ c/a) is shown in Fig. 4.6(a).

Obviously, introducing the metal slit to the originally matched zero-index meta-atom periodic array results in a deviation $\Delta\epsilon$ and $\Delta\mu$ from zero, preventing the unity transmission through the structure. To recover the matched zero index, the independent fine control of ϵ_{eff} and μ_{eff} as provided by our meta-atom is critical. For this, we focus on particles A and B (B') located at positions of abrupt change in the lateral PEC confinement. Fig. 4.6(b) shows $\Delta\epsilon_{\text{III}}$ extracted from the S-matrix parameters for the particle array at the output face [part III of the slit, Fig. 4.6(a)], before (dash-dot) and after (solid) the ϵ -tuning (ϵ_2 from 179.2 to 207.4) of the particle B; the nonzero $\text{Im}(\Delta\epsilon_{\text{III}})$ at $f = 0.212$ c/a has been successfully brought back to zero. Subsequently, the remaining nonzero $\text{Re}(\Delta\epsilon_{\text{III}})$ [Fig. 4.6(b)] for particle arrays I and III are compensated with the detuned ($\epsilon_2 = 168.0$) particle A to give $\text{Re}(\Delta\epsilon_{\text{II}}) + 2\text{Re}(\Delta\epsilon_{\text{III}}) = 0$ [Fig. 4.6(c)]. It is worth noting that the deviation $\Delta\mu$ was negligible, with the absence of magnetic charge for PEC ($\mu = 1$, $\epsilon = \infty$) leading to reduced distortion of the magnetic field [27,28].

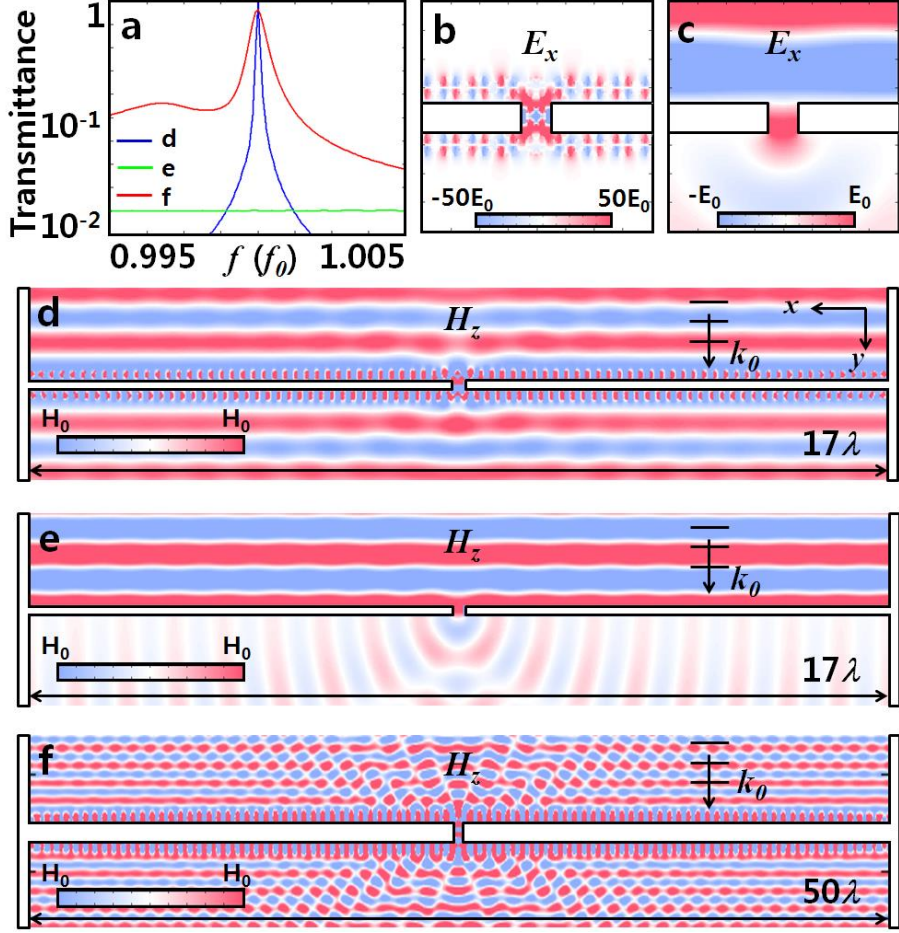


Fig. 4.7 (a) Transmission spectra of the slit; without (green) and with zero-index meta-atom array of (blue) high index (ϵ_1 , ϵ_2) = (14.53, 179.2) and (red) low index (2.22, 12.96) nano-pizza. f_0 is the frequency of matched zero index. (b, c) E_x field pattern near the nanoslit at f_0 , (b) with and (c) without the meta-atom array. (d-f) H_z field pattern of the slit at f_0 (d) without, (e) with high-index, and (f) with low-index nano-pizza meta-atom array. Slit width; 0.21λ (d, e) and 0.55λ (f).

The transmittance of the meta-atom coated nanoslit structure

with tuned particles A and B (B') shows almost perfect transmittance of 0.97 [Fig. 4.7(a), (d)], a ~ 50 times increase compared to the slit with no meta-atom coating [Fig. 4.7(a), (e)]. This clearly demonstrates super-funneling of flux 17 times greater than the λ -zone. Further, the near field pattern in Fig. 4.7(b), (c) shows the associated dramatic enhancement of the electric field with the presence of the single layer of matched zero index meta-atoms. We have further considered a low-index 8-slice nano-pizza [$(\epsilon_1, \epsilon_2) = (2.22, 12.96)$ at $R = 0.45a$ providing matched zero index at $f = 0.546 c/a$, see Fig. 4.3(d)] over much larger flux reception area (50λ). To compensate for a factor of ~ 90 channel width variation (50λ to 0.55λ), an increased number of tuning particles [A to G – see Fig. 4.6(a)] were used to suppress higher order modal components of nonzero k_x . A transmittance of 0.85 was achieved, showing the super-funneling of 42λ -flux ($50\lambda \cdot 0.85$) through the meta-atom coated slit [Fig. 4.7(a), (f)].

4.6. Summary

To summarize, a hypothetical meta-atom of internal anisotropy has been proposed. Introducing the split-symmetry of susceptibility $\chi_r \neq \chi_\theta$ conforming to the orthogonal axes of current pathways of the respective electric- and magnetic-dipoles, we show analytically the decoupling and separate tunability of ϵ_{eff} and μ_{eff} ; the desired optical response is then provided by proper choice of ϵ_r and ϵ_θ readily obtained from our top-down approach. Nano-pizzas and nano-donut structures have been proposed as a means to attain the split radial-angular anisotropy. A nano-pizza assembled from all-lossless dielectric materials has been demonstrated to exhibit the matched zero index property; thus overcoming the significant loss problem intrinsic to metamaterials based on metallic inclusions and lifting the restrictions of accidental degeneracy. In an application to EOT, utilizing a single layer of matched zero index meta-atoms, we demonstrated for the first time a super-funneling of flux two orders of magnitude beyond the usual λ -zone limit.

Our proposal to introduce coordinate-conforming anisotropy for decoupling the electric and magnetic responses and thus allowing the separate control over ϵ_{eff} and μ_{eff} is applicable to elementary resonators in other exotic coordinate systems compliant to current pathways of chosen electric / magnetic resonances. We expect future development of other anisotropic meta-atom families based on our approach.

Chapter 5.

Inverse design of an acoustic omni meta-atom for the reconfigurable, full access to wave parameter space

5.1. Introduction

The common behavior of a wave is completely determined by the wave parameters of its medium, which are in general associated with the fundamental oscillations of its elementary particle. In the context of metamaterials, the decoupled excitation of these fundamental oscillations in a meta-atom would provide an ideal platform for the top-down and reconfigurable access to the entire space of wave parameters, but this has been remained as a conceivable and complicated problem that has to be fulfilled, as pointed out by Pendry [30,67]. Here focusing on the case of an acoustic meta-atom, we achieve the decoupling of density ρ , modulus B^{-1} and

bianisotropy [28] ξ , by separating paths of particle momentum to conform to the basis vectors of each macroscopic wave parameters. Independent access to all octants of parameter space $(\rho, B^{-1}, \xi) = (+/-, +/-, +/-)$ is thus realized under the single platform of an omni meta-atom, as a building block which empowers a reconfigurable [66,68,69], in addition top-down and deterministic access to all the target properties of meta-materials. Reconfigurable acoustic wave front shaping, and bianisotropic pressure-velocity conversion are experimentally demonstrated under the meta-surface and meta-waveguide context, in excellent agreement with theoretical analysis.

The general outcome of the wave propagation is ultimately determined by the properties of its medium, where the wave travels through. In order to achieve an extreme manipulation of the wave propagation, thus an accessibility to the unusual space of wave parameters are obligatory, including regimes not offered by the natural materials. Wide variety of artificial, extreme wave parameters and their application have been witnessed for different types of waves and material systems in the name of metamaterials; to cover; acoustics [19–21,24,25,38,70–73], photonics [4,12,28,29,62,74–76], thermodynamics [77], elastodynamics [78], seismics, and etc. Negative [19–23], zero [4,24], ultra-high [12,25] index, hyperbolic [26], anisotropic [27], bianisotropic [28] and chiral [29] metamaterials, along with their exotic applications towards cloaking [30,38,67,78], super-focusing [27], perfect absorption [72], and frequency-agile memory [79] also have been explored and demonstrated so far.

With the advent of metamaterials, with keen interest on their applications, the active and deterministic control of their wave parameters has become one of the main stream of wave physics [20,21,30,67,69]. Meanwhile the decoupling of the fundamental wave parameters has been envisaged as an ideal platform (Pendry et. al., [67]) toward top-down and reconfigurable design of the meta-atom, nonetheless, has yet remained as a plausible idea that yet has to be answered. At the present status in contrast, strategies for metamaterial design have been based on bottom-up, retro-fit approaches – where the building blocks are initially proposed and the subsequent design is carried out through a series of iterations and guesswork, with the hope that the specific index and impedance of target purpose is realized. The full accessibility to the entire space of wave parameters with the various designs of existing meta-materials still is an open question, and the existence of an omni-potent meta-atom for the reconfigurable, seamless access to the wave parameter space also has to be answered.

In this chapter, we propose an entirely new design strategy of the meta-atom inspired by fundamental oscillations of the elementary particle of a wave. Focusing on the acoustic platform, criteria for decoupling of ρ , B^{-1} and ξ are derived based on the first principles calculations, and an omni meta-atom design achieving full access to the entire wave parameter space is demonstrated. Deterministic, top-down control of the omni meta-atom for reconfigurable wave front manipulation, and bianisotropic acoustic field conversion are demonstrated under the meta-surface and meta-waveguide context.

As is well-known that the electromagnetic wave parameter ϵ and μ of a classical atom are directly related to the linear and angular oscillations of an elementary particle of an electron, our approach starts from the observation of characteristic oscillation of the underlying elementary particles (such as electrons, holes, ions, and particles with mass, etc.), in relation to the wave parameters of interest. In this respect, the analytical derivation of effective parameters of acoustic wave ($\rho_{\mathbf{n}}$: density for \mathbf{n} direction and B^{-1} : inverse modulus) from the motions of particles are straightforward.

5.2. Derivation of acoustic macroscopic wave parameters from the electromagnetic first-principle homogenization theory

To give motivations to design the structure, we started the effective acoustic parameters which calculated from the macroscopic acoustic wave equation, in the manuscript. In this section, we provide detailed derivation process from the first-principles a new homogenization theory, which has been suggested by Alù [74] used for determining electromagnetic parameters of metamaterials.

The starting equations of the microscopic acoustic wave for the time harmonics of $\exp(i\omega t)$, based on the Newton's second law and Hooke's law of motion is well-known as below [38],

$$\begin{aligned}\nabla p(\mathbf{r}) &= -i\omega\rho_0\mathbf{v}(\mathbf{r}) - i\omega\rho_0(\rho_u - 1)\mathbf{v}(\mathbf{r}) \\ \nabla \cdot \mathbf{v}(\mathbf{r}) &= -i\omega B_0^{-1}p(\mathbf{r}) - i\omega B_0^{-1}(B_u^{-1} - 1)p(\mathbf{r})\end{aligned}\tag{5.1}$$

where $p(\mathbf{r})$ and $\mathbf{v}(\mathbf{r})$ is pressure and velocity field at \mathbf{r} , ρ_0 (ρ_u) and B_0 (B_u) is the density and modulus of the background (materials), and ω is the angular frequency. From (5.1), we derive macroscopic acoustic equation by applying Floquet theory with $\exp(-i\boldsymbol{\beta} \cdot \mathbf{r})$ dependence. Applying average operation $\int a^{-2}\exp(i\boldsymbol{\beta} \cdot \mathbf{r})dS$ on (5.1) for the square lattice (lattice constant a , unit cell area S) for the two-dimensional case, we write,

$$\begin{aligned}
-i\boldsymbol{\beta}\bar{p} &= -i\omega\rho_0\bar{\mathbf{v}} - \frac{i\omega\rho_0}{a^2} \int_S (\rho_u - 1)\mathbf{v}(\mathbf{r})e^{i\boldsymbol{\beta}\cdot\mathbf{r}} dS \\
-i\boldsymbol{\beta} \cdot \bar{\mathbf{v}} &= -i\omega B_0^{-1}\bar{p} - \frac{i\omega B_0^{-1}}{a^2} \int_S (B_u^{-1} - 1)p(\mathbf{r})e^{i\boldsymbol{\beta}\cdot\mathbf{r}} dS \quad (5.2) \\
\text{where } \bar{\mathbf{v}} &= \frac{1}{a^2} \int_S \mathbf{v}(\mathbf{r})e^{i\boldsymbol{\beta}\cdot\mathbf{r}} dS \text{ and } \bar{p} = \frac{1}{a^2} \int_S p(\mathbf{r})e^{i\boldsymbol{\beta}\cdot\mathbf{r}} dS.
\end{aligned}$$

From the macroscopic relation of (5.2), we can now express constitutive effective parameters of ρ and B^{-1} . Taking similar approach of the electromagnetic case [74], we take Taylor's expansion of the $\int_S (\rho_m - 1)\mathbf{v}(\mathbf{r})e^{i\boldsymbol{\beta}\cdot\mathbf{r}} dS$ by assuming long wavelength limit ($a \ll 2\pi/|\boldsymbol{\beta}|$).

$$\begin{aligned}
\int_S \mathbf{W}(\mathbf{r})e^{i\boldsymbol{\beta}\cdot\mathbf{r}} dS &= \int_S \mathbf{W}(\mathbf{r})dS - i\boldsymbol{\beta} \times \int_S \frac{\mathbf{r} \times \mathbf{W}(\mathbf{r})}{2} dS + \dots, \quad \text{where } \mathbf{W}(\mathbf{r}) = (\rho_u - 1)\mathbf{v}(\mathbf{r}). \quad (5.3) \\
\int_S (B_u^{-1} - 1)p(\mathbf{r})e^{i\boldsymbol{\beta}\cdot\mathbf{r}} dS &= \int_S (B_u^{-1} - 1)p(\mathbf{r})dS - i\boldsymbol{\beta} \cdot \int_S \frac{\mathbf{r}(B_u^{-1} - 1)p(\mathbf{r})}{2} dS + \dots
\end{aligned}$$

Worth to note, we neglect $\int_S (B_u^{-1} - 1)p(\mathbf{r})e^{i\boldsymbol{\beta}\cdot\mathbf{r}} dS$ as its effect is small for the practical design ($B_u^{-1} \ll B_0^{-1}$, whereas $\rho_u \gg \rho_0$ for general solid). Now using (5.3), we may write (5.2) as

$$\begin{aligned}
-i\boldsymbol{\beta}[\bar{p} - \frac{i\omega}{2a^2} \int_S \mathbf{r} \cdot \mathbf{W}(\mathbf{r})dS] &= -i\omega\rho_0[\bar{\mathbf{v}} + \frac{1}{a^2} \int_S \mathbf{W}(\mathbf{r})dS] \\
-i\boldsymbol{\beta} \cdot [\bar{\mathbf{v}} - \frac{i\omega}{2a^2} \int_S \mathbf{r}(B_u^{-1} - 1)p(\mathbf{r})dS] &= -i\omega B_0^{-1}[\bar{p} + \frac{1}{a^2} \int_S (B_u^{-1} - 1)p(\mathbf{r})dS] \quad (5.4)
\end{aligned}$$

Following the procedures of [74], we now compare microscopic (5.1) and macroscopic (5.4) equations, to express effective acoustic parameters of ρ and B^{-1} .

$$\begin{aligned}
\boldsymbol{\rho}(\hat{\mathbf{n}}) &= \frac{\int_S \rho_n \mathbf{v} \cdot \hat{\mathbf{n}} dS}{a^2 \bar{\mathbf{v}} \cdot \hat{\mathbf{n}} - \frac{i\omega}{2} \int_S r B_u^{-1} p \hat{\mathbf{r}} \cdot \hat{\mathbf{n}} dS} = \frac{\int_S \boldsymbol{\pi} \cdot \hat{\mathbf{n}} dS}{a^2 \bar{\mathbf{v}} \cdot \hat{\mathbf{n}} - \frac{i\omega}{2} \int_S (\nabla \cdot \mathbf{q}) \mathbf{r} \cdot \hat{\mathbf{n}} dS}, \\
B^{-1} &= \frac{\int_S B_u^{-1} p dS}{a^2 \bar{p} + \frac{i\omega}{2} \int_S r \rho_r \mathbf{v} \cdot \hat{\mathbf{r}} dS} = \frac{\int_S \nabla \cdot \mathbf{q} dS}{a^2 \bar{p} + \frac{i\omega}{2} \int_S \boldsymbol{\pi} \cdot \mathbf{r} dS}
\end{aligned} \tag{5.5}$$

for a two dimensional square unit cell S of lattice constant a , having distributed particle density tensor $\boldsymbol{\rho}_m$ and modulus B_m of the constituting materials where \mathbf{r} the position vector measured from the cell center, p and \mathbf{v} the pressure and velocity fields at \mathbf{r} . Important to note from (5.5) is the presence of cross-coupling terms in the denominators of $\boldsymbol{\rho}_m$ (B^{-1}) and B_m ($\boldsymbol{\rho}_m$) related to the spatial dispersion effects [74], hindering the decoupling of $\boldsymbol{\rho}_m$ and B_m . Nonetheless, understanding the physical origin of the cross-coupling which becomes negligible in the limit of $r \sim 0$, it is also possible to interpret partially achieve the decoupling of effective parameters $\boldsymbol{\rho}_m$ and B^{-1} from $B_m^{-1}(\mathbf{0})$ and $\boldsymbol{\rho}_m \cdot \boldsymbol{\theta}$ respectively, from (5.5).

5.3. Ideal meta-atom platform of decoupling acoustic parameters

5.3.1. Schematics

To realize above basic assumption, we design the meta-atom structure by constructing anisotropic mass ρ_m and non-local modulus B_m . We consider two sets of properly chosen main design parameters to control; widths of membranes (b_o , b_l) and volumes of the sub-cells (V_o , V_l); where we divided the linear (b_o) and radial (b_l) momentum, and also outer (V_o) and inner (V_l) meta-atom modulus as conceptualized in Fig. 5.1.

Another important question is whether the wave parameters of proposed meta-atom are analytically solvable. Being ideal platform of splitting kinetic energy in the membranes ($\rho_{mem} \gg 0$), and strain energy in the air sub-cells ($B_0 \ll B_{mem}$), we can separately apply Newton's law into the membranes and Hooke's law into the sub-cell to give formula of ρ and B^{-1} . To verify our theory, we not only performed the numerical analysis using COMSOL based on FEM algorithm but also carried experiment; with constructing the 3D converted meta-atom sample using acrylic glass wall and LLDPE (Linear low density polyethylene) membrane. To assign reconfigurability to the meta-atom, the control of the individual sub-cell volumes (V_o , V_l) = ($s_o h_o$, $s_l h_l$) has been realized by changing the heights of the sub-cells (h_o , h_l) using vertically moving floor. The experimental determination of the wave parameters have been performed by measuring S parameters from the impedance tube.

5.3.2. Analytical derivation of the effective parameters

Here we derive effective acoustic parameters of the 2D meta-atoms. To explicitly express the equations, we show the structures and symbols in the manuscript as Fig. 5.1.

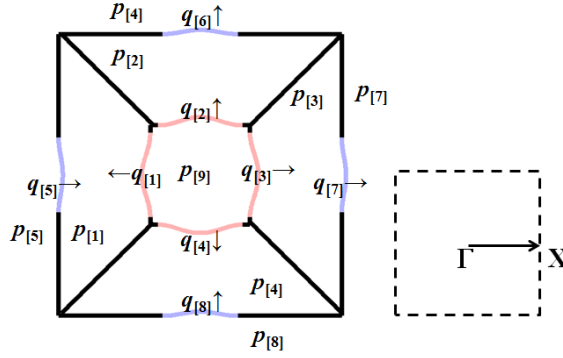


Fig. 5.1 The schematics of meta-atom. p and q denote for average pressure and displacement for each cells and membranes. Arrows in q denote the positive directions.

All unknown p and q 's to be solved are numbered in Fig. 5.1. Using the equations (5.1) in the manuscript, we can govern linear system problem ($\mathbf{A}\mathbf{x} = 0$) calculate eigenmode, where \mathbf{A} is the 17 by 17 matrix and \mathbf{x} is the vector consisting all of p 's and q 's. Focusing on the ΓX direction of the acoustic wave,

$$\begin{pmatrix}
1 & 0 & 0 & 0 & 0 & 0 & 0 & 0 & 0 & 0 & C_o & 0 & 0 & 0 & -C_o & 0 & 0 & 0 \\
0 & 1 & 0 & 0 & 0 & 0 & 0 & 0 & 0 & 0 & -C_o & 0 & 0 & 0 & 0 & C_o & 0 & 0 \\
0 & 0 & 1 & 0 & 0 & 0 & 0 & 0 & 0 & 0 & 0 & -C_o & 0 & 0 & 0 & 0 & C_o & 0 \\
0 & 0 & 0 & 1 & 0 & 0 & 0 & 0 & 0 & 0 & 0 & 0 & C_o & 0 & 0 & 0 & 0 & -C_o \\
0 & 0 & 0 & 0 & 0 & 0 & 0 & 0 & 0 & 1 & -C_I & C_I & C_I & -C_I & 0 & 0 & 0 & 0 \\
1 & 0 & 0 & 0 & -1 & 0 & 0 & 0 & 0 & 0 & 0 & 0 & 0 & 0 & 0 & M_o & 0 & 0 \\
0 & 1 & 0 & 0 & 0 & -1 & 0 & 0 & 0 & 0 & 0 & 0 & 0 & 0 & 0 & -M_o & 0 & 0 \\
0 & 0 & 1 & 0 & 0 & 0 & -1 & 0 & 0 & 0 & 0 & 0 & 0 & 0 & 0 & 0 & 0 & -M_o \\
0 & 0 & 0 & 1 & 0 & 0 & 0 & -1 & 0 & 0 & 0 & 0 & 0 & 0 & 0 & 0 & 0 & M_o \\
1 & 0 & 0 & 0 & 0 & 0 & 0 & 0 & -1 & -M_I & 0 & 0 & 0 & 0 & 0 & 0 & 0 & 0 \\
0 & 1 & 0 & 0 & 0 & 0 & 0 & 0 & -1 & 0 & M_I & 0 & 0 & 0 & 0 & 0 & 0 & 0 \\
0 & 0 & 1 & 0 & 0 & 0 & 0 & 0 & -1 & 0 & 0 & M_I & 0 & 0 & 0 & 0 & 0 & 0 \\
0 & 0 & 0 & 1 & 0 & 0 & 0 & 0 & -1 & 0 & 0 & 0 & -M_I & 0 & 0 & 0 & 0 & 0 \\
0 & 0 & 0 & 0 & 0 & 0 & 0 & 0 & 0 & 0 & 0 & 0 & 0 & e^{-i\beta_o na} & 0 & 0 & -1 & 0 \\
0 & 0 & 0 & 0 & 0 & 0 & 0 & 0 & 0 & 0 & 0 & 0 & 0 & 0 & 0 & 1 & 0 & -1 \\
e^{-i\beta_o na} & 0 & -1 & 0 & e^{-i\beta_o na} & 0 & -1 & 0 & 0 & 0 & 0 & 0 & 0 & 0 & 0 & 0 & 0 & 0 \\
0 & 1 & 0 & -1 & 0 & 1 & 0 & -1 & 0 & 0 & 0 & 0 & 0 & 0 & 0 & 0 & 0 & 0
\end{pmatrix}
\begin{pmatrix}
p_{[1]} \\
p_{[2]} \\
p_{[3]} \\
p_{[4]} \\
p_{[5]} \\
p_{[6]} \\
p_{[7]} \\
p_{[8]} \\
p_{[9]} \\
q'_{[1]} \\
q'_{[2]} \\
q'_{[3]} \\
q'_{[4]} \\
q'_{[5]} \\
q'_{[6]} \\
q'_{[7]} \\
q'_{[8]}
\end{pmatrix}
=
\begin{pmatrix}
0 \\
0 \\
0 \\
0 \\
0 \\
0 \\
0 \\
0 \\
0 \\
0 \\
0 \\
0 \\
0 \\
0 \\
0 \\
0 \\
0 \\
0
\end{pmatrix} \quad (5.6)$$

where $C_I = \frac{B_0 a}{s_I}$, $C_o = \frac{B_0 a}{s_o}$, $M_I = \frac{a(k_I - m_I \omega^2)}{b_I^2}$, $M_o = \frac{a(k_o - m_o \omega^2)}{b_o^2}$, and $q'_n = \frac{b_n}{a_n} q_n$.

The (5.6) consists of the equations from Hooke' s law (row 1 to 5), Newton' s second law (row 6 to 13), and Floquet' s boundary (row 14 to 17). From (5.6), n could be analytically determined by solving the equation $\text{Det}(\mathbf{A}) = 0$ as below, to give non-zero physical null space \mathbf{x} .

$$\begin{aligned}
\exp(i\beta_o na) &= \frac{1}{2C_o^2 C_I} \{M_o(M_I + C_o)(M_I + C_o + 4C_I) + 2C_o[M_I(M_I + C_o) + C_I(4M_I + C_o)] \pm \\
&\sqrt{[2M_I C_o + M_o(M_I + C_o)][M_I + C_o + 4C_I]} \times \\
&\sqrt{[2M_I C_o(M_I + C_o) + 4C_o C_I(2M_I + C_o) + M_o(M_I + C_o)(M_I + C_o + 4C_I)]}\}
\end{aligned} \quad (5.7)$$

Then, we express effective impedance Z from the null space x.

$$\begin{aligned}
ZZ_0 &= \frac{2i\omega q'_{[7]}}{p_{[7]} + p_{[3]}} = \\
&\pm \frac{2i\omega(M_I + C_o)\sqrt{M_I + C_o + 4C_I}}{\sqrt{[2M_I C_o + M_o(M_I + C_o)]}} \times \\
&\frac{1}{\sqrt{[2M_I C_o(M_I + C_o) + 4C_o C_I(2M_I + C_o) + M_o(M_I + C_o)(M_I + C_o + 4C_I)]}}
\end{aligned} \quad (5.8)$$

Solving the inverse problem of (5.7) and (5.8), the design parameters of membrane M_o , and M_I could be determined from the desired acoustic parameters (ρ, B^{-1}) expressed using the relations of $\rho = n/Z$ and $B^{-1} = nZ$.

5.3.3. Analytical derivation of the effective spring constant and effective mass of the membrane slab

Here we solve the effective spring constant k and effective mass of the membrane slab m in manuscript, based on the plate bending theory. The problem space is illustrated in Fig. 5.2.

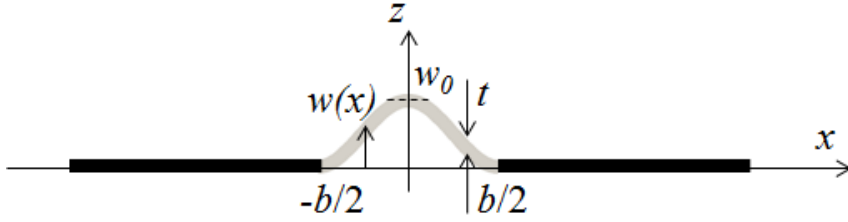


Fig. 5.2 Cylindrical bending of the membrane (gray) with fixed edge at the metallic boundary.

From the Kirchhoff–Love plate theory [80], we start from the governing equation to solve displacement profile $w(x)$ of the membrane. For one-dimensional we get,

$$\frac{\partial^4 w}{\partial x^4} = -\frac{Q}{D} \quad (5.9)$$

where $D = Et^3/[12(1 - \nu^2)]$ is the plate stiffness factor (E : Young's modulus, ν : Poisson's ratio) [81], and Q is an applied transverse load per unit area. Assuming uniform load distribution Q , we can express $w(x)$ by 4th polynomial function [80].

$$w(x) = \sum_{n=0}^4 a_n x^n \quad (5.10)$$

We then apply boundary condition to get a_n 's. For the fixed

edge at the boundary, w and dw/dx is zero ($x = \pm b/2$) [81].
Now $w(x)$ is,

$$w(x) = w_0 \left(1 - \frac{4x^2}{b^2}\right)^2 \quad (5.11)$$

where $w(0) = w_0$ (Fig. 5.2).

From w , we calculate total strain energy V and total kinetic energy T of the vibrating plate [81],

$$\begin{aligned} V &= \frac{D}{2} \int_{-b/2}^{b/2} \left(\frac{\partial^2 w}{\partial x^2}\right)^2 dx = \frac{512Dw_0^2}{5b^3} \\ T &= \frac{\rho_m \omega^2 t}{2} \int_{-b/2}^{b/2} w^2 dx = \frac{64\rho_m \omega^2 w_0^2 bt}{315} \end{aligned} \quad (5.12)$$

where ρ_m is the density of the membrane. Now we can finally derive analytical expression of k and m from (5.12), from the relation between average displacement $\langle w \rangle = b^{-1} \int w dx = (8/15) \cdot w_0$ and energies.

$$\begin{aligned} k &= \frac{2V}{\langle w \rangle^2} = \frac{2 \cdot 512Dw_0^2}{5l^3 \left[\int_{-l/2}^{l/2} w(x) dx / b \right]^2} = \frac{60Et^3}{(1-\nu^2)b^3} \\ m &= \frac{2T}{\omega^2 \langle w \rangle^2} + m_{air} = \frac{2 \cdot 64\rho_0 w_0^2 bt}{315 \left[\int_{-l/2}^{l/2} w(x) dx / b \right]^2} + m_{air} = \frac{10\rho_m bt}{7} + m_{air} \end{aligned} \quad (5.13)$$

m_{air} is the mass of the air near the vibrating membranes which depends on the geometry near the membranes. The numerical fitting values of m_{air} are listed in captions of Fig. 5.3 with all geometry cases in the meta-atom.

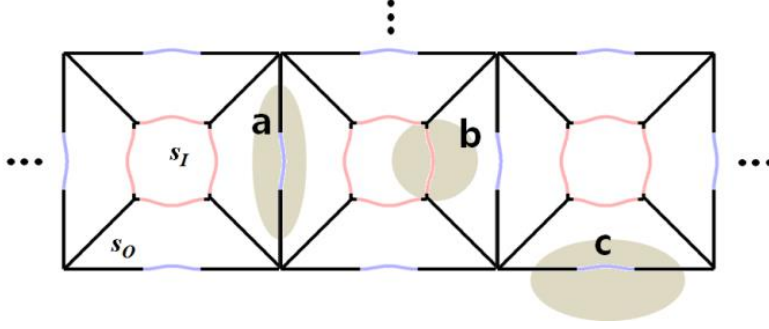


Fig. 5.3 The portion of air (gray) area moving with membranes. (a) Outer ($m_{\text{air}} = 0.6\rho_0 s_O$), (b) inner membranes ($m_{\text{air}} = 0.5\rho_0 s_I + 0.25\rho_0 s_I$) in the meta-atom array, and (c) membranes at the interfaces ($m_{\text{air}} = 0.9\rho_0 s_O$) between meta-atoms and air.

5.3.4. Numerical and experimental demonstration of top-down design for proposed meta-atom

Fig. 5.4(b) shows excellent agreement between the analytical solution and parameters from numerically calculated S-parameters (COMSOL) of 2D meta-atom. From the analytically solved formulas of (5.7) and (5.8), we plot the visualized mapping between parameters (ρ, B^{-1}) and (b_0, b_I) as shown in Fig. 5.4(c) (1,500 Hz). Near the Dirac point $[4, 24]$ of $(\rho, B^{-1}) = (0, 0)$ the long wavelength limit, perfect orthogonality between (b_0, b_I) as expected from first assumption. For the 3D case, we also plotted the mapping for the theoretical (Fig. 5.4(d)) and experimental (Fig. 5.4(e)) result for the target frequency 1,200 Hz; although not perfect agreement observed from the fabrication error, it is possible to find desired parameter with changing (h_0, h_I) . Overall, not only the determination of (b_0, b_I) and (h_0, h_I) is possible from simply

choosing desired parameters, but also the full accessibility to the quadrant parameters sets can be observed.

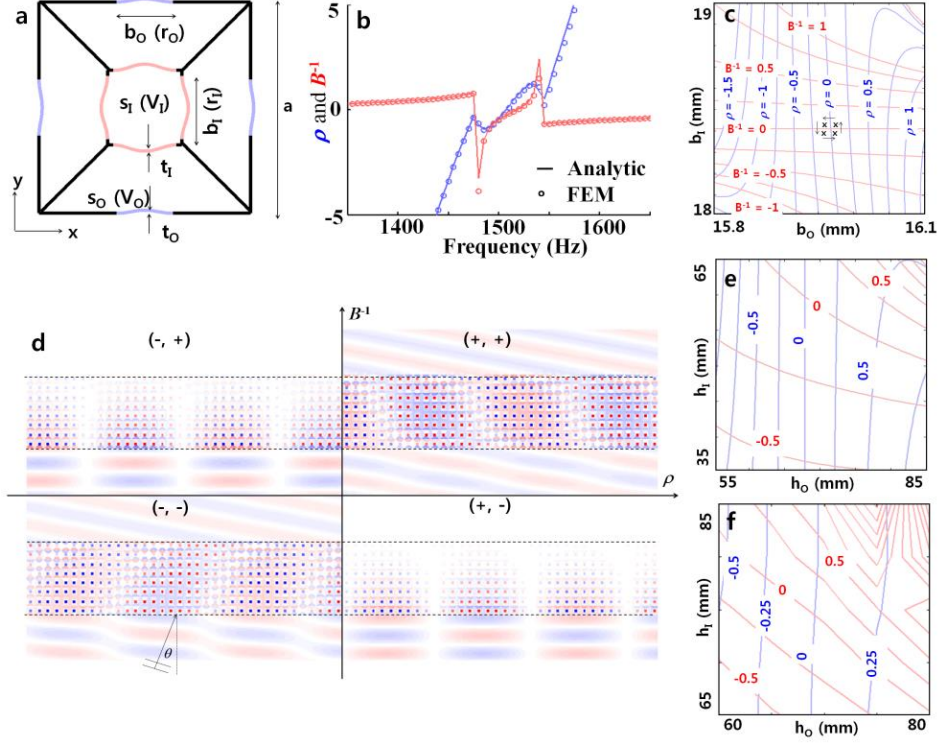


Fig. 5.4 Schematics and extracted parameters for proposed meta-atom. Demonstration of the complete quadrants of the effective parameters sets ($\rho = \pm 0.4$, $B^{-1} = \pm 0.1$) for the proposed meta-atom (inside dashed line). (a) Schematic of the proposed meta-atom (blue, red and black: outer, inner membranes, and solid wall, b , t and s : membrane length, thickness, and sub-cell area, subscript O and I: outer and inner membranes or cells), (b) Analytically (line) and numerically (circle) calculated effective parameters spectra of the proposed meta-atom. (c) Mapping of the ρ and B^{-1} to the outer and inner membranes at 1500Hz, (d) Numerically calculated pressure

field pattern (blue: low, red: high) for the case of oblique incidence ($\theta = 10^\circ$) at 1500 Hz.

To demonstrate the wave behavior of the meta-atom, we numerically plot the pressure field pattern for the oblique incident case at a plane metamaterial boundary. For the case of quadrant I and III, the target parameters have been determined to give zero reflection at a boundary according to the following impedance matching conditions [82].

$$\rho = \frac{n}{\sqrt{1+(1-n^{-2})\tan^2\theta}}, B^{-1} = n\sqrt{1+(1-n^{-2})\tan^2\theta} \quad (5.14)$$

For the case of $n = \pm 0.2$ and $\theta = 10^\circ$, the target parameters are $\rho = \pm 0.4$ and $B^{-1} = \pm 0.1$ from (5.14). For the remaining quadrants II and IV, we switch the sign of the parameters. From the targets, the design parameters are determined with only changing the width of the membranes. Fig. 1(d) shows the pressure field pattern and k vector of wave inside the meta-atom arrays. For the quadrants I and III ($\rho B^{-1} > 0$), the propagating wave inside meta-atom is observed with positive and negative refractions as expected. For the quadrants II and IV ($\rho B^{-1} < 0$) in contrast, the exponential decay is observed through the meta-atom.

5.3.5. Incident angle dependency

As the analytical effective parameters of the meta-atoms in the manuscripts are derived assuming ΓX directions, the results can be assured only for the normal incidence case. However, as

shown in the Fig. 5.4 (d) in the manuscript, excellent acoustic wave behaviors of the proposed meta-atom were observed even for the oblique case. To study for the case of oblique incidence, we show the numerical results of the effective parameters of the meta-atoms for different incident angles in Fig. 5.5. Except the case of B^{-1} splitting near 1500 Hz, the parameters show independency for incident angle; the analytical top-down design can be applied to oblique case.

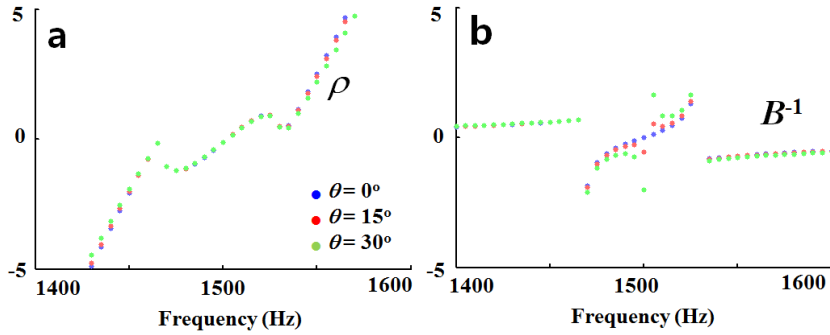


Fig. 5.5 Numerically extracted effective parameters of the meta-atom (designed to give matched zero index at 1500 Hz). (a) ρ and (b) B^{-1} spectra.

5.3.6. Membrane designs at interface between air and meta-atom layers

As there is abrupt change in pressure across the membranes, the membrane designs at the interface between air and meta-atom need to be modified. For this, we compare the cases for membrane in the meta-atoms and at the interfaces as shown in Fig. 5.6.

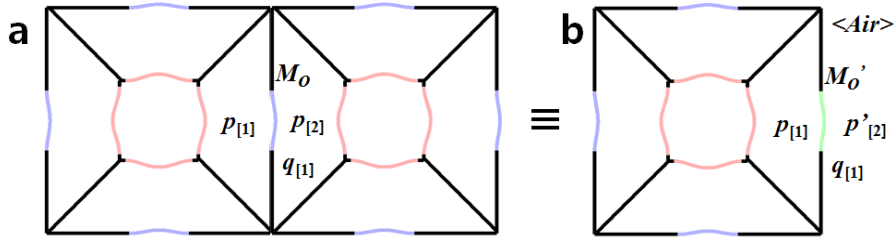


Fig. 5.6 The outer membrane at the (a) internal unit cells and (b) interfaces.

The relations between p and q' are $p_{[1]} - p_{[2]} = M_o q_{[1]}$ for (a) and $p_{[1]} - p'_{[2]} = M_o' q_{[1]}$ for (b) from the newton's law. As we assumed mid-value of the pressure while deriving impedance in (5.8), the pressure $p'_{[2]}$ at the air boundary has to be mid-values of pressure, $(p_{[1]} + p_{[2]})/2$. From above relations, we can express modified values of M_o' to be redesigned, as below.

$$M_o' = \frac{p_{[1]} - p'_{[2]}}{q_{[1]}} = \frac{p_{[1]} - p_{[2]}}{2q_{[1]}} = \frac{1}{2} M_o \quad (5.15)$$

5.4. Application to the meta-surface example utilizing designed meta-atom

We now show the application example of the reconfigurable meta-surface using our meta-atom. Controlling discontinuous phase shift across the surface, the arbitrary wave shaping is enabled from the generalized Snell's law [83] of light. For our case, we make the 2D experiment setup with 7x1 array of the meta-atom with motorized stage to measure the field pattern (Fig. 5.7(a),(b)). For the as-wish manipulation of the sound, the phase shift is calculated for the each atom. Controlling the individual phase shift ($\phi_{\text{shift}} = n_{\text{eff}}k_0a$) across the meta-atom by reconfiguring each meta-atom wave parameters based on the design. Also the numerical analysis has been performed based on 2D meta-atom with similar ϕ_{shift} to the experiment (Fig. 2c-f, bottom row) and normalized simulation area at 1,500 Hz. In Fig. 2c-f, the examples of wave shaping is demonstrated; no distortion, wave front shift, focusing, and diverging of the sound with good agreement between simulation (top row) and experiment (middle row).; although considerable reflection for the experiment caused from the impedance mismatch.

From the decoupling and complete accessibility to the wave parameter space as clearly described analytically and numerically above, our next step is fulfilling and reproducing the top-down and reconfigurable design experimentally using the proposed meta-atom. Fig. 3b shows the experimental mapping (ρ , B^{-1}) to the (h_0 , h_l) at 1,200Hz, clearly the

decoupling ρ from V_I is observed, as well as full accessibility of the wave parameter quadrants. Also as plotted in Fig. 3c, the measured bianisotropic parameter ξ also could be controlled by Δh_0 although the not perfect decoupling of (ρ, B^{-1}) from Δh_0 achieved, completing the omni-behavior for octant wave parameter space (ρ, B^{-1}, ξ) .

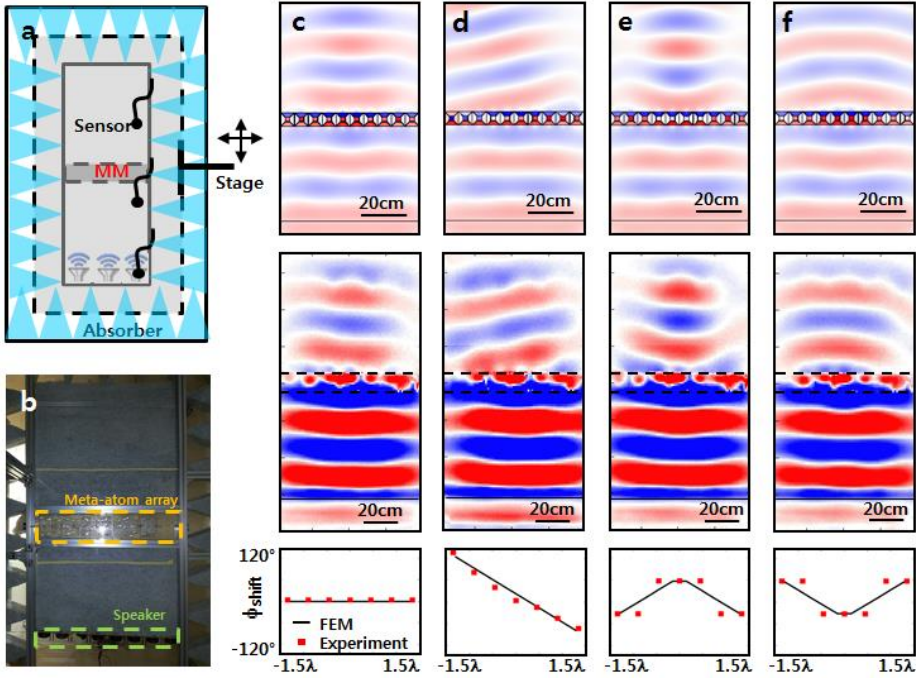


Fig. 5.7 Experimental results for reconfigurable meta-surface
a,b The schematic and picture of the meta-surface experimental set-up. c-f, The examples of wave-shaping of the reconfigurable meta-surface; Measured field pattern of no distortion, propagation wave shift, focusing, and diverging respectively.

5.5. Concept extension to the bianisotropy and energy conversion

5.5.1 Energy conversion in bianisotropic media

Extending the discussion beyond the decoupling of (ρ, B^{-1}) , it is important to note that our formalism could be generalized to the other wave parameters such as bianisotropy [28]. Meanwhile the non-zero bianisotropy has been realized using chiral and Ω -type metamaterials [28,29] in nano-photonics, this has yet to be conceptualized and demonstrated for the acoustic meta-atom to achieve the cross-conversion between velocity and stress, or displacement and momentum. Out of different bianisotropic parameters accessible in acoustics and elastics (x, y, z) , For our case, here we focus on the off-diagonal component ξ of the stress-strain coupling tensor [84], which also could be calculated from the S parameters [28].

The investigation of bianisotropic medium starts from the solving the general wave equations of the plane wave, written as,

$$\begin{aligned} v &= v_+ \exp(-ink_0 x) + v_- \exp(ink_0 x), \\ p &= v_+ z_+ \exp(-ink_0 x) - v_- z_- \exp(ink_0 x) \end{aligned} \quad (5.16)$$

where z_+ and z_- refers to the acoustic impedance depending on the sign of the directions. From the relationship of $\xi = -in(z_+ - z_-)/(z_+ + z_-)$, it is straightforward to find separated impedances $z_+ \neq z_-$ occurs for nonzero ξ . The remarkable physical feature of bianisotropic medium is manipulating wave

impedance of the sound, exchanging kinetic and potential energy during wave propagation, toward impedance manipulation of the sound. This could be understood by considering for the case of $\rho = B^{-1} = 0$ ($z_+ \rightarrow 0$, $z_- \rightarrow \infty$, $n \rightarrow i\xi$) in (5.16), the wave solution could be simplified as below.

$$v = v_0 \exp(\xi k_0 x), \quad p = p_0 \exp(-\xi k_0 x). \quad (5.17)$$

From (5.17), it is clear that sound impedance (p/v) exponentially changes, without loss of energy transmission for constant v_p . Also, the impedance change is inverse for opposite directions ($\pm x$) showing undisputable reciprocity [84].

5.5.2 Analytical derivation of bianisotropy in proposed meta-atom

Noting that ξ originates from the structural anti-symmetry / asymmetry [74], we apply asymmetry in the form of Δb_I is provided for to controlling ξ ; without any change for (ρ , B^{-1}) in 1st order as shown Fig. F1. For the top-down determination of the design parameters, the analytical expression of bianisotropy ξ (pseudo chirality, [28]) is given below.

$$\xi \sim -\frac{2\omega\Delta b\rho_0}{Z_0} \times \frac{C_o^2(M_I + C_o^2 + 2C_I^2)}{[2M_IC_o + M_o(M_I + C_o)]} \times \frac{1}{[2M_IC_o(M_I + C_o) + 4C_oC_I(2M_I + C_o) + M_o(M_I + C_o)(M_I + C_o + 4C_I)]} \quad (5.18)$$

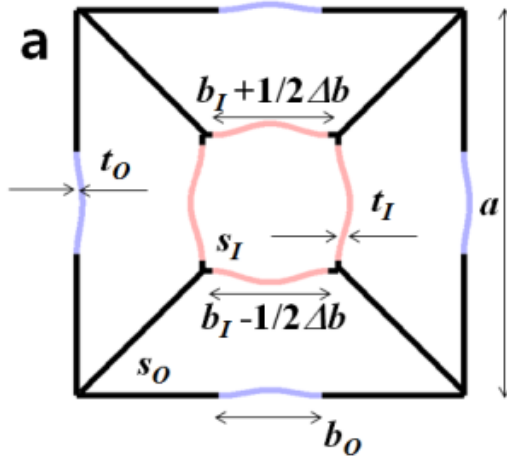


Fig. 5.8. Schematics for nonzero bianisotropy of the proposed meta-atom when $\Delta b \neq 0$.

5.5.3 Beam Steering and Focusing by impedance-matched Acoustic Meta-surface

In contrast to various devices of functionalities of meta-surface have been proposed however, the current status of the meta-surface [83,85–90] yet does not guarantee the complete transmission across the surface, as it is difficult to match the meta-surface's impedance to the background medium, with controlling of the phase shift (ϕ_{shift}) at the same time. For this, decoupled control of the wave parameters (e.g. ϵ and μ for electromagnetics, ρ and B^{-1} for acoustics) of each individual meta-atom of meta-surface is indispensable for attaining desired $\text{shift} = (\rho/B)^{1/2}k_0d$ and, $Z = (\rho B)^{1/2}$ for the acoustic wave. Here focusing on the acoustic domain, we propose the decoupling ρ and B^{-1} by introducing anisotropic mass vibrating through linear and radial directions. Furthermore, we also introduce concept the bianisotropy to provide the generalized

impedance matching for meta-surface where the input side and output side's impedance inequality sets ($Z_i \neq Z_t$) as well.

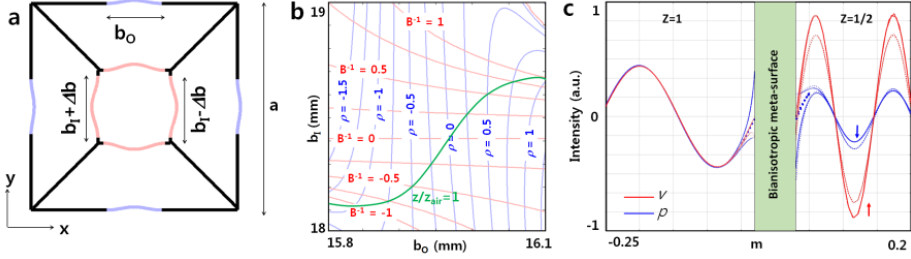


Fig. 5.9 (a) Schematic of the acoustic meta-atom. $\Delta b/2$ (b) Wave parameter mapping of meta-atom reconfiguration. (c) Wave impedance manipulation of bianisotropic medium. (d: thickness, $Z \rightarrow Z_1$ $Z \rightarrow Z_2$)

We used the PMMA for a sound insulating wall, LLDPE thin film for a membrane. The lattice constant $a = 6\text{cm}$ used at operation frequency of 1,500 Hz. The mapping of wave parameters (ρ , B^{-1}) into the width of the outer and inner membranes (b_0 , b_1) is numerically demonstrated (Fig. 5.9(b)), near matched zero index ($\rho = B^{-1} = 0$). The design parameters for impedance matching condition ($\rho = B^{-1}$) with air are expressed following a green line in Fig. 1b, for obtaining desired phase shift, with no reflection; the tuning of the refractive index (phase shift across the surface) ranged from -1.5 (-140°) to 1.5 (140°). In addition, the bianisotropy ξ could be introduced by applying asymmetry Δb to the meta-atom. From the very definition of ξ (cross-coupling parameters between p and v) [28], the exchange between potential and kinetic energy in a bianisotropic media is natural; the maximum transmittance could

be achieved by proper choice of Δb for ξ , of satisfying $\exp(2\xi k_0 d) = Z_2/Z_1$ (Fig. 5.9(c))

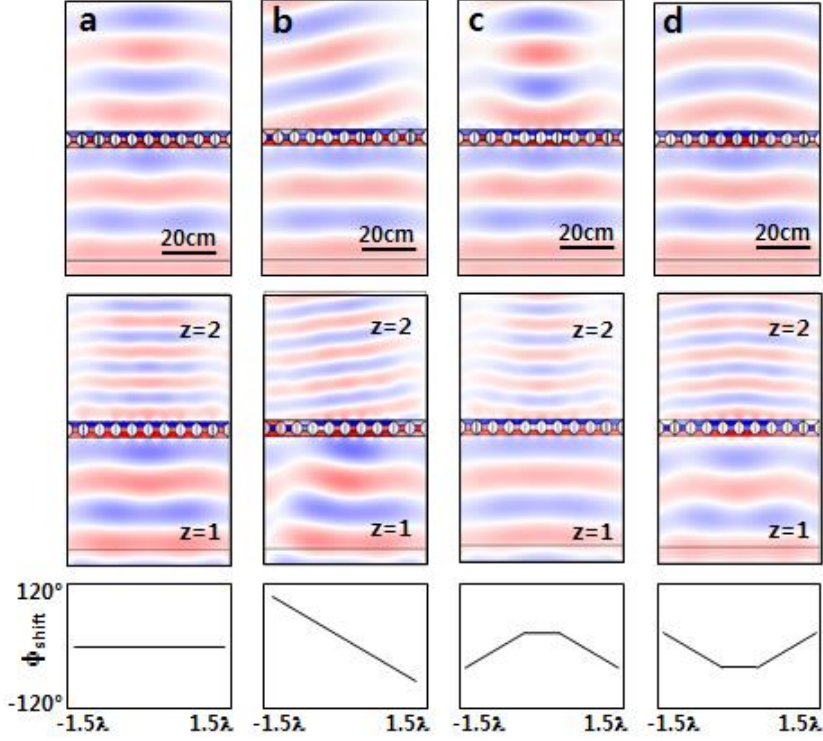


Fig. 5.10 Numerical demonstration of wave controlling by meta-surface. (a) Straight propagation, (b) 10° beam bending, (c) beam focusing, (d) beam diverging case. Wave propagation for the case of impedance of input and output sides are same (top) and output side is doubled (middle), controlled phase of meta-atoms (bottom).

We built a meta-surface by composing meta-atom arrays (10 by 1) described above and delicately tuned the membranes. Determining refractive indices (phase shift) of each atom by the wave propagating directions of their positions from the

generalized Snell' s law, the design parameters of (b_0, b_l) could be specified through the green guiding line in Fig. 1b. The two cases are under consideration for our meta-surface between same ($Z_1 = Z_2$, Fig. 2a) and different ($Z_1 = 2Z_2$, Fig. 2b) impedance media; demonstrating 4 different types of beam manipulating situations; straight propagation, beam steering, focusing and diverging for both case with controlling (b_0, b_l) for the phase shift as (Fig. 5.10(c)). We also note that although we have used same design parameters of (b_0, b_l) both case in Fig. 10(a),(b) for different Δb (0, 0.5 mm), the expected patterns of the wave is achieved for both case toward decoupled design of (ρ, B^{-1}) and ξ .

5.5.4 Numerical / Experimental derivation of bianisotropy

Using bianisotropic meta-atom, we now then demonstrate a link for the waveguide pairs of different impedance with using as described in Fig. 5.11. Six meta-atoms at the input side with ξ , and $\rho = B^{-1} = 0$, as well as meta-atoms layer of $(\rho, B^{-1}, \xi) = (0, 0, 0)$ in the output side are used. As shown in the analytically calculated field (Fig. 5.11 red and blue line), the behavior of p and v gets separated to decrease the impedance p/v at region I, and the sound flow velocity gets distributed evenly along the waveguide to suppress the higher modes at region II. Also the exponential decay of the pressure inside the meta-atom could be clearly observed from the numerical result. Obviously, the desired ξ for complete transmission could be calculated depending on the impedance ratio and the length of the bianisotropic meta-atom ($\xi = \log(1/11)/(-2k_0 \cdot 6a) \sim 0.12$

for our case). With changing ξ for different Δb in the region I, we plot the numerically calculated transmittance in Fig. 5.12 (a),(b), agreeing well with the analytical result and maximum $\sim 90\%$ transmittance achieved at $\Delta b = 0.48$ mm ($\xi \sim 0.11$).

To experimentally show the impedance conversion in nonzero ξ meta-atom as we showed in Fig. 5.11, we put the single meta-atom between waveguides of different cross-section (Fig. 5.12(d)). Although the transmittance was near 0.5 which has been dissipated, the maximum point occurs in $\Delta h_0 = -15$ mm corresponding to $\xi = -0.20$, which is close from the desired value of $\xi = \log(4)/(-2k_0 \cdot 0.12) \sim -0.26$ for impedance matching.

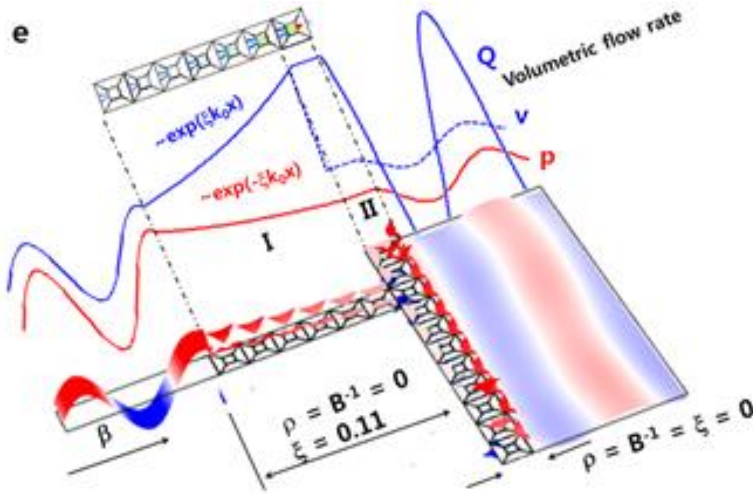


Fig. 5.11 The structure of in analysis of asymmetric tunneling with six bianisotropic meta-atoms ($\Delta b = 0.48$ mm) in the gap, and with matched zero index meta-atom array at the output side ($\Delta b = 0$). The analytically (blue and red line) and numerically calculated pressure field profile displayed

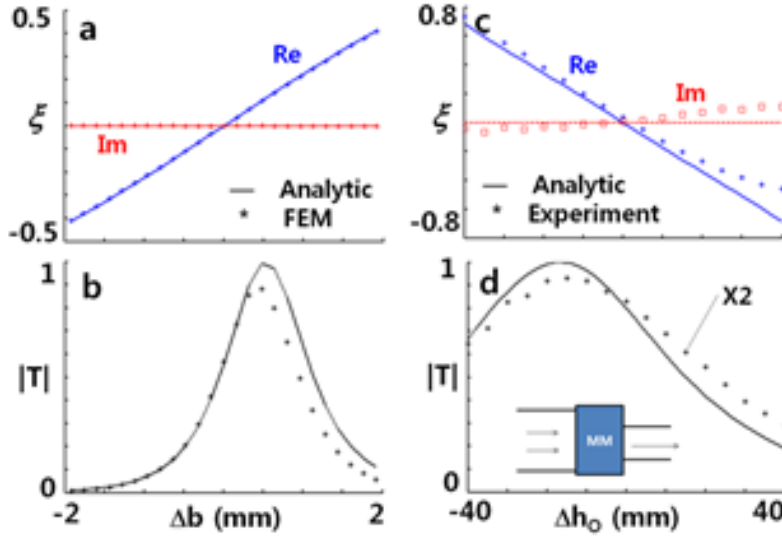


Fig. 5.12 Design and the pressure field pattern of the bianisotropic meta-atom. (a) Bianisotropy ξ for different Δb designed at 1500Hz. (b) Analytically and numerically calculated transmittance of the structure (c) depending on Δb . (c) Measured bianisotropy ξ with the control of geometric asymmetry Δh_0 (marker: experiment data, dashed: fitted). (d) Transmittance for different Δh_0 of a single meta-atom connecting waveguides of different cross-section area (5cm and 2.5cm radius).

5.6 Summary

Our proposed omni meta-atom visualized the mapping between wave parameters (ρ, B^{-1}, ξ) and $(b_o, b_l, \Delta b_l)$ or $(h_o, h_l, \Delta h_o)$ which could access to the all octant space near Dirac point, toward top-down meta-atom. In addition to the (ρ, B^{-1}, ξ) , there exist other unexplored parameters inside the constitutive tensor of the elastic wave which could be controlled understanding the fundamental mode of its parameter from first-principle homogenization techniques. Moreover, our reconfigurable meta-atom providing more freedom of wave control, we also expect reconfigurable all-in one multi-functional elastic device (cloaking, super-focusing, perfect absorption for example) in the single platform.

Chapter 6.

Conclusion

The new top-down design of the metamaterials has been proposed throughout the thesis, especially targeted for the field confinement of the electromagnetic and acoustic wave. For the numerical analysis of those problems, I have set-up the super computer CPU and GPU clusters and programmed home-made FDTD algorithm.

From the numerical set-up, I have performed the investigation into the extreme light electric and magnetic focusing at the nanogap and nanowire, revealing the role of the surface impedance on the Babinet's principle. The application examples are demonstrated for the active switch by utilizing the energy confinement, and also for magnetic polarizer by separation of the electric and magnetic field.

To increase the energy focusing efficiency at the nano structure we focus on the fundamental limitation of the λ -zone, which restricts the size of the light collection area in terms of

the wavelength. This limit can be overcome by utilizing matched zero index metamaterials; by effectively change the λ -zone to the infinite area. In addition, the new metamaterial top-down design paradigm have been proposed using the anisotropic hypothetical meta-atom; motivated by the electric and magnetic dipoles in the classical atom.

This design concept has been extended to the sound wave based on the duality relation between acoustic and electromagnetic wave. For the desired parameters of ρ , B^{-1} , ξ , the mass of the membranes are analytically determined. The applications of acoustic meta-surface and bianisotropic impedance conversion are demonstrated.

References

- [1] A. Ahmadi and H. Mosallaei, Phys. Rev. B 77, 045104 (2008).
- [2] Q. Zhao, J. Zhou, F. Zhang and D. Lippens, Mater. Today 12, 60 (2009).
- [3] C. M. Soukoulis and M. Wegener, Nat. Photonics 5, 523 (2011).
- [4] X. Huang et al., Nat. Materials 10, 582 (2011).
- [5] I. B. Vendik, O. G. Vendik, and M. S. Gashinova, Tech. Phys. Lett. 32, 429 (2006)
- [6] M. Silveirinha and N. Engheta, Phys. Rev. B 75, 075119 (2007).
- [7] B. Edwards, A. Alù, M. E. Young, M. Silveirinha and N. Engheta, Phys. Rev. Lett. 100, 033903 (2008).
- [8] Q. Cheng et al., Appl. Phys. Lett. 91, 234105 (2007).
- [9] M. Silveirinha and N. Engheta, Phys. Rev. Lett. 97, 157403 (2006).
- [10] M. G. Silveirinha, Phys. Rev. E 73, 046612 (2006).
- [11] V. M. Shalaev, Nat. Photonics 1, 41 (2007).
- [12] M. Choi et al., Nature 470, 369 (2011).
- [13] A. Alù and N. Engheta, Opt. Express 17, 5723 (2009).
- [14] A. Alù, A. Salandrino and N. Engheta Opt. Express 14, 1557 (2006).
- [15] A. Vallecchi, M. Albani and F. Capolino, Opt. Express 19, 2754 (2011).
- [16] N. A. Mirin and N. J. Halas, Nano Lett. 9, 1255 (2009).
- [17] P. Ginzburg, et al., Nano Lett. 11, 2329 (2011).
- [18] E. Plum et al., Phys. Rev. B 79, 035407 (2009).
- [19] Wu, Y., Lai, Y. & Zhang, Z-Q. Elastic metamaterials with simultaneously negative effective shear modulus and mass density. Phys. Rev. Lett. 107, 105506 (2011).
- [20] Liang, Z., Willatzen, M., Li, J. & Christensen, J. Tunable acoustic double negativity metamaterial. Sci. Rep. 2, 859

(2012).

- [21] Yang, M., Ma, G., Yang, Z. & Sheng, P. Coupled membranes with doubly negative mass density and bulk modulus. *Phys. Rev. Lett.* 110, 134301 (2013).
- [22] Hosang Yoon, Kitty Y. M. Yeung, Vladimir Umansky & Donhee Ham, *Nature* 488, 65–69 (2012)
- [23] S. Zhang, et al., Near-infrared double negative metamaterials, *Optics express*, 13, 4922 (2005)
- [24] Liu, F., Huang, X. & Chan, C. T. Dirac cones at $k = 0$ in acoustic crystals and zero refractive index acoustic materials. *Appl. Phys. Lett.* 100, 071911 (2012).
- [25] Popa, B-I. & Cummer, S. A. Design and characterization of broadband acoustic composite metamaterials. *Phys. Rev. B* 80, 174303 (2009).
- [26] Fang, N. et al. Sub-diffraction-limited optical imaging with a silver superlens. *Science* 308, 534–537 (2005).
- [27] Li, J., Fok, L., Yin, X., Bartal, G. & Zhang, X. Experimental demonstration of an acoustic magnifying hyperlens. *Nat. Materials* 8, 931 (2009).
- [28] Li., Z., Aydin, K. & Ozbay, E. Determination of the effective constitutive parameters of bianisotropic metamaterials from reflection and transmission coefficients. *Phys Rev. E* 79, 026610 (2009).
- [29] Zhang, S. et al. Negative refractive index in chiral metamaterials. *Phys. Rev. Lett.* 102, 023901 (2009).
- [30] D. Schurig et al., *Science* 314, 977 (2006).
- [31] H. Chen, C. T. Chan and P. sheng, *Nat. Materials* 9, 387 (2010).
- [32] D. A. Genov, S. Zhang and X. Zhang, *Nat. Physics* 5, 687 (2009).
- [33] J. Li and J. B. Pendry, *Phys. Rev. Lett.* 101, 203901 (2008).
- [34] J. H. Kang, D. S. Kim and Q.-H. Park, *Phys. Rev. Lett.* 102, 093906 (2009).

- [35] Z. Ruan and S. Fan, Phys. Rev. Lett. 105, 013901 (2010)
- [36] Taflove, A. & Hagness, S. C. Computational Electromagnetics: The Finite Difference Time-Domain Method (Artech House, 2000).
- [37] M. Born and E. Wolf, Principles of Optics (Pergamon, Oxford, 1964)
- [38] Cummer, S. A. & Schurig, D. One Path to acoustic cloaking. New J. of Phys. 9, 45 (2007).
- [39] T. W. Ebbesen et al., Nature 391, 667 (1998)
- [40] J. B. Pendry, L. Martín-Moreno and F. J. García-Vidal, Science 305, 847 (2004)
- [41] W. L. Barnes, A. Dereux and T. W. Ebbesen, Nature 424, 824 (2003)
- [42] T. Matsui et al., Nature 446, 517 (2007)
- [43] J. W. Lee et al., Phys. Rev. Lett. 99, 137401 (2007)
- [44] F. J. García de Abajo, R. Gómez-Medina, and J. J. Sáenz, Phys. Rev. E 72, 016608 (2005)
- [45] F. J. García-Vidal, et al., Phys. Rev. Lett. 95, 103901 (2005)
- [46] Y. Takakura, Phys. Rev. Lett. 86, 5601 (2001)
- [47] F. Yang and J. R. Sambles, Phys. Rev. Lett. 89, 063901 (2002)
- [48] H. Liu, and P. Lalanne, Nature 452, 728 (2008)
- [49] M. A. Seo et al., Nature photonics 3, 152 (2009)
- [50] I. V. Shadrivov et al., Opt. Express 16, 20266 (2008)
- [51] C. Rockstuhl, et al., Opt. Express 16, 2080 (2008)
- [52] C. Xiang et al., ACS Nano, 2, 1939 (2008)
- [53] T. Senior, IEEE Trans. 25, 417 (1977)
- [54] Ordal, M. A. Optical properties of the metals Al, Co, Cu, Au, Fe, Pb, Ni, Pd, Pt, Ag, Ti and W in the infrared and far infrared. Appl. Opt. 22, 1099 -1119 (1983).
- [55] E. Kreysziq, Advanced engineering mathematics (Wiley, Singapore, 1999)
- [56] H. K. Chaurasia, W. A. G. Voss, IEEE Trans. 21, 51

(1973)

[57] M. D. Harpen, Phys. Med. Biol, 33, 329 (1988)

[58] Bethe, H. A. Theory of diffraction by small holes. Phys. Rev. 66, 163 (1944).

[59] Jackson, J. D. Classical Electrodynamics. 3rd edn (John Wiley & Sons Inc, 1999).

[60] Nikitin, A.Yu., Zueco, D., Garcia-Vidal, F. J. & Martin-Moreno, L. Electromagnetic wave transmission through a small hole in a perfect electric conductor of finite thickness. Phys. Rev. B. 78, 165429 (2008).

[61] J. Sheen, J. of Electromagn. Waves and Appl. 19, 753 (2005).

[62] D. R. Smith, S. Schultz, P. Markoš and C. M. Soukoulis, Phys. Rev. B 65, 195104 (2002).

[63] F.-G. Hu, J. Song and T. Kamgaing, EPEPS, IEEE 19th Conference on, 225 (2010).

[64] Jonghwa Shin, Jung-Tsung Shen, and Shanhui Fan, Phys. Rev. Lett. 102, 093903 (2009)

[65] S. Koo, M. S. Kumar, J. Shin, D. Kim and N. Park, Phys. Rev. Lett. 103, 263901 (2009).

[66] M. A. Seo et al., Nano Lett. 10, 2064 (2010).

[67] Pendry, J. B., Schurig, D. & Smith, D. R. Controlling electromagnetic fields. Science 312, 1780 (2006).

[68] Zheludev, N. I. & Kivshar, Y. S. From metamaterials to metadevices. Nat. Materials 11, 917 (2012).

[69] Ou, J. Y., Plum, E., Jiang, L. & Zheludev, N. I. Reconfigurable photonic metamaterials, Nano Lett. 11, 2142 (2011).

[70] Hu, X., Ho, K.-M., Chan, C. T. & Zi, J. Homogenization of acoustic metamaterials of Helmholtz resonators. Phys. Rev. B 77, 172301 (2008).

[71] Cheng, Y., Xu, J. Y. & Liu, X. J. One-dimensional structured ultrasonic metamaterials with simultaneously negative dynamic density and modulus. Phys. Rev. B 77,

045134 (2008).

[72] Mei, J. et al. Dark acoustic metamaterials as super absorbers for low-frequency sound. *Nat. Commun.* 3, 756 (2012).

[73] Park, C. M. et al. Amplification of acoustic evanescent waves using metamaterial slabs. *Phys. Rev. Lett.* 107, 194301 (2011).

[74] Alù, A. First-principles homogenization theory for periodic metamaterials. *Phys. Rev. B* 84, 075153 (2011).

[75] Pendry, J. B., Holden, A. J., Stewart, W. J. & Youngs, I. Extremely low frequency plasmons in metallic mesostructures. *Phys. Rev. Lett.* 76, 4773 (1996).

[76] Pendry, J. B., Holden, A. J., Robbins, D. J. & Stewart, W. J. Magnetism from conductors and enhanced nonlinear phenomena. *IEEE Trans. Microwave Theory Tech.* 47, 2075 (1999).

[77] Robillard, J-F. et al. Phononic metamaterials for thermal management: an atomistic computational study. *Chinese J. of Phys.* 49, 448 (2011).

[78] Brun, M., Guenneau, S. & Movchan, A. B. Achieving control of in-plane elastic waves. *Appl. Phys. Lett.* 94, 061903 (2009).

[79] Driscoll, T. et al. Memory metamaterials. *Science* 325, 1518 (2009).

[80] Timoshenko, S. & Woinowsky-Krieger, S. *Theory of plates and shells* (McGraw-Hill, New York, 1989).

[81] Steinberg, D. S. *Vibration analysis for electronic equipment* (John Wiley & Sons, New York, 2000).

[82] Cheng, D. K. *Field and wave electromagnetics* (Addison Wesley, Singapore, 1989).

[83] Yu, N. et al. Light propagation with phase discontinuities: generalized law of reflection and refraction. *Science* 334, 333 (2011).

[84] Mackay, T. G. and Lakhtakia, A. *Electromagnetic anisotropy and bianisotropy: A field guide* (World Scientific,

Singapore, 2010)

[85] S. Sun, Q. He, S. Xiao, Q. Xu, X. Li and L. Zhou, Nat. Mater. 11, 426 (2012).

[86] J. Zhao, B. Li, Z. N. Chen, and C. W. Qiu, Appl. Phys. Lett. 103, 151604 (2013).

[87] X. Ni, N. K. Emani, A. V. Kildishev, A. Boltasseva, and M. Shalaev, Science 335, 427 (2012).

[88] L. Zigoneanu, B. I. Popa, and S. A. Cummer, Phys. Rev. B 84, 024305 (2011).

[89] S. Sun et al., Nano Lett. 12, 6223 (2012).

[90] Y. Yang et al., Nano Lett. 14, 1394 (2014).

한 글 초 록

피동의 특이 투과 및 집속 현상은 1998년 Ebbesen의 최초 발견 이래로, 광학 분야에서 다양한 가시광선, 적외선, THz, 마이크로파 등의 거의 전 영역의 빛과 bow-tie, slit, hole antenna 등 다양한 미세 구조에 대해서 연구되어 왔다. 특히 전자기파는 금속의 skin-depth 깊이 이내에서의 전자와 결합하기 때문에, skin-depth 보다 작은 크기의 나노 구조에서는 특이 집속 현상이 어려울 것으로 일반적으로 여겨져 왔다. 본 학위 논문 초기에 해당하는 연구 내용은 3mm 파장을 가지는 빛을 skin-depth 보다 작은 70nm 금속 나노 구조, 또는 파장의 수만 분의 1 이하에 해당하는 구조와 상호 작용시켜 기존 연구에 비해 100배 이상 극한적이고 도전적인 상황에서의 특이 집속 현상을 연구한 것이다. Babinet's 원리에 입각하여 상보구조인 nanogap 과 nanowire 구조를 비교한 결과, nanogap의 전기장 집속도의 특이점이 skin-depth보다 훨씬 작은 Thomas-Fermi length (sub-nm)인 반면에 nanowire의 자기장 집속도는 특이점이 skin-depth가 주어짐을 규명하였다. 따라서 Babinet 원리는 극한 나노 영역에서는 실패하게 되며, nanowire의 자기장 에너지 집속도는 nanogap에서의 전기장 에너지 집속도 향상인 1,000,000배에 비해 줄어들게 되지만, 여전히 100,000배 정도의 큰 자기장 집속도 향상을 얻을 수 있었다. 이 연구 결과는 전자기장 기반의 비선형 소자와 센서 시스템에 활용될 수 있을 것이라 기대한다.

이의 후속 연구로써, 특이 집속 현상의 극대화를 위해 메타물질의 이용을 고려하였다. 유효 유전율 (ϵ)과 투자율 (μ)이 동시에 0인 물질을 이용하면, 공간을 유효적으로 없애는 것이 가능하고 이를 nanogap 구조에 적용하게 되면, 기존 한계영역으로 여겨져 왔던 λ -zone 이상으로 빛을 끌어 모을 수 있다. 이러한 메타

물질 구조들을 설계함에 있어서, 유전율과 투자율의 dipole moment를 고전적인 원자모델에 근거하여 구조적으로 분리시키고, 원하는 파라미터를 먼저 결정되면 그에 따라 설계 파라미터가 계산되는 하향식으로 체계화하였다. 우선 2006년에 Pendry가 언급했듯이, 유전율과 투자율이 분리되어 조절되는 이상적인 구조를 원하였는데. 이를 실현을 위하여, 물질의 유전율을 r 방향과 θ 방향으로 나누고 독립적으로 조절되는 비등방성 원자를 이론적으로 가정하여 유전율과 투자율을 분리시켰다. 또한 이 구조의 원하는 파라미터가 정해지면, 디자인이 정해지는 역함수 문제를 이론적으로 계산하는 데에 성공하여, ϵ , μ 모두 0을 가지기 위한 경우 설계 parameter를 이론적으로 결정하는 데에 성공하고 이를 수치해석으로 확인하였다. 이 주제의 응용으로써, 메타물질을 nanogap과 결합하여 기존한계영역의 50배 확장된 빛이 투과함을 확인하였다.

마지막으로 상기 개념을 전자기파에서 음파로 확장시켰다. 파동 사이에는 서로 파라미터 사이에 서로 대응 되는 duality관계가 있는데, 전자기파의 ϵ 과 μ 은 음파의 밀도(ρ)와 탄성계수 역수(B^{-1})가 서로 그러한 관계에 있다. 전자기파에서 그랬듯이 방과 방 사이를 연결하는 막 (membrane)의 질량을 linear한 방향과 radial한 방향을 분리하여 조절하면, ρ 와 B^{-1} 의 독립적인 조절이 가능하다. 이론적인 결과에 나타나 있듯이, linear하게 움직이는 바깥쪽 막과 radial하게 움직이는 안쪽 막은 각각 ρ 와 B^{-1} 와 직교 관계에 있다는 것을 알 수 있고, 원하는 물질 파라미터에 대해서 막의 폭이 결정되는 하향식 설계가 가능함을 도식화한 것이다. 이 개념을 한차원 확장시켜, 물질의 비대칭성에 의해서 인가되는 파라미터인 bianisotropy를 구현하고 원하는 대로 이론적, 실험적으로 조절 하는 데에 성공하였다. 이의 응용 예로써, 비대칭적인 impedance를 가지는 넓은 도파로에서 좁은 도파로로 소리를 집속하고 또는 역으로 방사시키는 현상을 이론적,

실험적으로 보여주었다.

주요어 : 나노 광학, 메타 물질, 나노 광 집속, 음향학
학 번 : 2009-30177